Multi-centre molecules driven by intense laser fields

Ahai Chen

Department of Physics and Astronomy

University College London

October 17, 2017

I, Ahai Chen, confirm that the work presented in this thesis is my own. Where information has been derived from other sources, I confirm that this has been indicated in the work.

Abstract

In this dissertation we investigate the underlying mechanisms for double ionisation in atoms and frustrated double ionisation in multi-centre molecules. We first study the main mechanisms that underlie non-sequential double ionisation in atoms that are driven by near-single-cycle intense laser fields. Unlike long laser pulses, short ones allow for an easier comparison between theory and experiment. We compare several very recently measured experimental quantities for strongly-driven *Ar* with our computational results and find good agreement. Next, we investigate double ionisation, frustrated double ionisation, frustrated single ionisation in two-electron triatomic molecules. We compare our computational results for the sum of the kinetic energies of the final ion fragments for double ionisation and for frustrated double ionisation with experimental results. We find very good agreement, particularly for frustrated double ionisation. Moreover, we find that, as for diatomic molecules, two pathways prevail in frustrated ionisation of two-electron triatomic molecules. Only in one of these pathways electron-electron correlation plays an important role. For non-sequential double ionisation, it is well established both theoretically and experimentally that electron-electron correlation plays an important role. However, this is not the case for frustrated double ionisation. We identify a scheme of two colour, orthogonally polarised laser fields that can control the strength of the electron-electron correlation in frustrated double ionisation as a function of the time delay between the two laser pulses. Therefore, based on our proposed combination of laser pulses future experiments can demonstrate the role of electron-electron correlation in frustrated double ionisation.

Acknowledgements

Contents

List of Figures

List of Tables

List of Abbreviations

1D	One-dimensional
3D	Three-dimensional
ADK	Ammosov-Delone-Krainov
CEP	Carrier-envelope phase
DI	Double ionisation
EI	Electron-impact ionisation
FDI	Frustrated double ionisation
FSI	Frustrated single ionisation
FVE	Focal volume effect
HHG	High harmonic generation
KER	Kinetic energy release
MO-ADK	Molecular Ammosov-Delone-Krainov
NSDI	Non-sequential double ionisation
OTC	Orthogonally polarised two-colour
RESI	Recollision-induced excitation with subsequent field ionisation
SAE	Single active electron
SI	Single ionisation
WKB	Wentzel-Kramers-Brillouin

Chapter 1

Introduction

Significant advances have been achieved in strong field physics since the invention of the laser in the middle of the last century [1]. One of the most important ones is the generation of attosecond pulses [2–4]. Multi-electron dynamics takes place on the attosecond time scale. Therefore, attosecond pulses can probe electron motions[5, 6]. The ultimate goal is to use ultrafast laser pulses to control electronic motion and chemical reactions, thus, impacting physics, chemistry and biology [7–11].

1.1 Attosecond pulse generation and the three-step model

In 2001, a train of pulses of attosecond duration [12] as well as the first single attosecond pulse of 650 as [2] were realised. These pulses were generated based on high harmonic generation (HHG). HHG was first observed by McPherson et al. [13] and M. Ferray et al. [14] at the end of the 1980s. A surprising finding was that the intensity of the high harmonics has a plateau over many orders of magnitude and then falls abruptly to zero at an energy equal to $E_{cut-off} = 3.17U_p + I_p$ [13–15]. U_p is the average energy an electron can gain in the laser field, while I_p is the ionisation energy. This cut-off energy can be understood in terms of the three-step model proposed by Paul Corkum in 1993 [16]. This model has played a central role in

generating attosecond laser pulses and in understanding multi-electron dynamics in atoms and molecules in intense laser fields [16, 17]. It involves the following stages, see Fig.1.1: (a) tunnelling ionisation, (b) propagation, and (c) recollision. In step (a) a valence electron ionises to the continuum either by tunnelling ionisation or by over-the-barrier ionisation when the Coulomb potential is lowered by the external laser field. Then, in step (b) the initially ionising electron is accelerated by the oscillating laser field and propagates in the continuum. When the field reverses its direction, the electron has a certain probability to return to the parent ion. Finally, in step (c) the electron can either recombine with the parent ion or recollide with the bound electrons [16, 18]. In the former case, high harmonics are emitted [15, 19]. In the latter case, the returning electron transfers energy to the bound electrons, leading to the excitation or direct ionisation of the electrons involved. In step (c) the highest kinetic energy an electron has upon returning to the parent ion is 3.17 U_p.
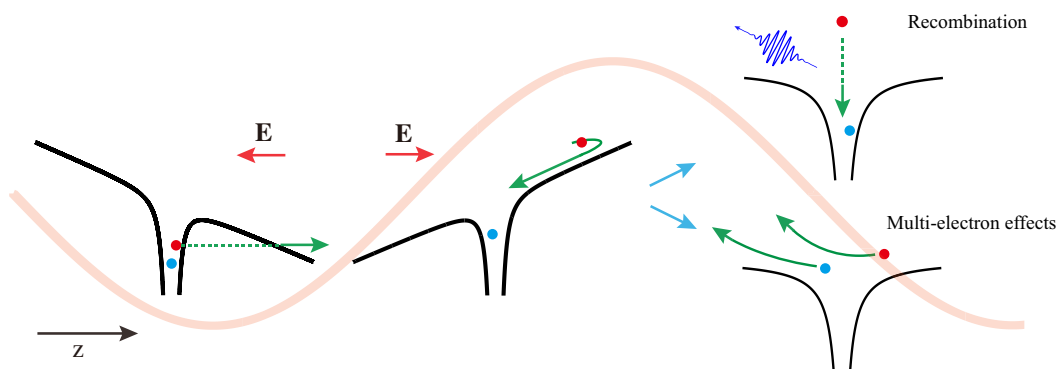
Figure 1.1: Schematic illustration of the three-step model.

1.2 Background on atoms and molecules in strong laser fields

We discuss the progress that has been achieved in the field of intense laser-matter interactions in non-sequential double ionisation (NSDI) in atoms and in frustrated ionisation in molecules. These phenomena will provide the background

information to the results relevant to this dissertation.

1.2.1 Non-sequential double ionisation in atoms

For high intensities of the laser field, in double ionisation, the two electrons are pulled away sequentially by the laser field. However, for intermediate intensities electron-electron correlation plays an important role in double ionisation (DI). First evidence for NSDI was provided by experiments in the 1980s [20–23]. A milestone for NSDI was the experiment in 1994 by Walker et al. [24] who performed a measurement for single ionisation (SI) and DI of *He* in a 160 fs linearly polarised laser pulse. The measurement was carried out over a range of 12 orders of magnitude of the intensity. It was found that the DI yields for high intensities in the region of 5×10^{15} W/cm^2 to 10^{16} W/cm^2 are consistent with sequential double ionisation and agree with the results obtained using a single active electron (SAE) approximation [25, 26]. The striking feature in this experiment is that for intermediate intensities (10^{14} W/cm^2 to 10^{15} W/cm^2) the DI yields are many orders of magnitudes higher than what is predicted by single active electron methods [25, 26]. The failure of these latter techniques to account for the measured DI yields for intermediate intensities suggests that electron-electron correlation is important in this regime, thus, the term non-sequential double ionisation. NSDI has been observed in many different atoms, for example, in *He* [22, 24, 27], *Xe* [28] and *Ar* [29], to mention but a few.

Non-sequential double ionisation can be understood in terms of the recollision picture [16]. During the recollision step, the returning electron transfers energy to the bound electron, leading to DI. According to the three-step model, the recollision step takes place at a zero of the electric field, i.e. when the electron momentum is maximum. If both electrons are ionised soon after recollision takes place then the two electrons escape with similar large momenta along or opposite the direction of the laser field. This interpretation was first verified by Weber et al. and Moshammer et al. in 2000 [30, 31], who measured and found that the ion momentum distribution along the polarisation direction of the laser field in *Ar* has two peaks. Further

evidence for the underlying mechanisms of NSDI was provided by another experiment by Weber et al. [32]. The latter measured the correlated electron momenta distribution of the two emitted electrons along the polarisation direction of the laser field in *Ar*. In Fig.1.2, the correlated electron momenta are shown for two intensities. For the high intensity at 1.5×10^{15} W/cm^2, the correlated electron momenta have small values and are distributed in all four quadrants. For the intermediate intensity at 3.8×10^{14} W/cm^2, the correlated momenta are mainly distributed at the first and third quadrant and have large values. This latter feature is consistent with the recollision picture. However, even for the intermediate intensity, in Fig.1.2 it is shown that there is a significant probability for the electrons to be emitted in opposite directions occupying the second and fourth quadrants. It was thus concluded that more than one mechanism underlying NSDI.

It is by now established that there are two major mechanisms contributing to NSDI, i.e. the electron-impact ionisation (EI) [16, 31, 32] and the recollision-induced excitation with subsequent field ionisation (RESI) [33, 34], alternatively referred to as the direct and delayed ionisation [35], respectively. In EI, the bound electron obtains sufficient amount of energy from the returning electron to ionise to the continuum soon after recollision takes place. However, in RESI, the energy transferred from the returning electron is only enough to promote the bound electron to an excited state. Then, with further assistance from the laser field, the excited electron is subsequently ionised at a maximum of the laser field. These two different mechanisms result in different ion momentum distribution, or equivalently sum of the electron momenta, along the laser polarisation direction, see the right panel of Fig.1.2. In EI, the ion momentum distribution has two peaks away from the centre, while in RESI it is centred around zero [32–34].

Most of the experiments employ multi-cycle laser pulses allowing for multiple recollisions to occur before both electrons ionise. Multiple recollisions complicate the electron dynamics and render the comparison with theory difficult. Recently, however, kinematically complete experiments succeeded in confining NSDI to a single laser cycle by using carrier-envelope phase (CEP)-controlled few- and near-
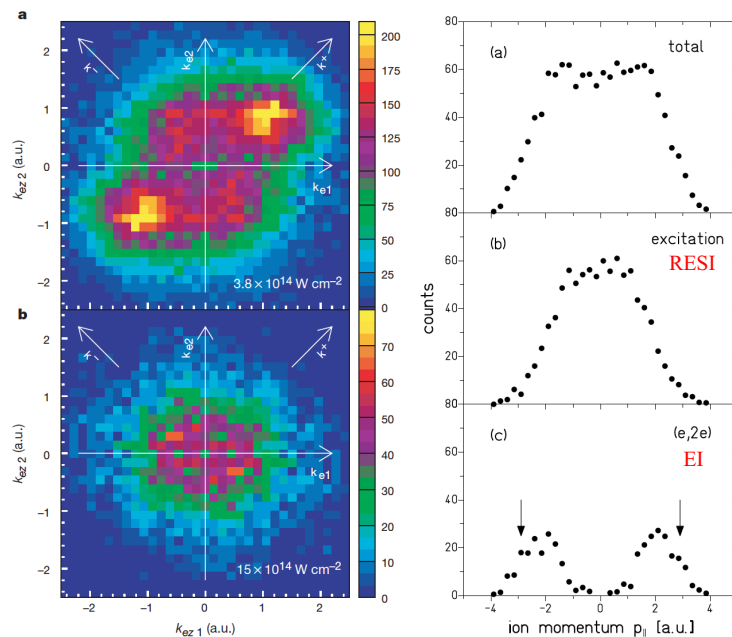
Figure 1.2: Left panel: the correlated electron momenta distributions along the polarisation direction of the laser field for double ionisation in *Ar* at different intensities, taken from [32], Copyright (2000) by Nature Publishing Group; Right panel: the ion momentum distribution along the polarisation direction of the laser field corresponding to double ionisation events at different quadrants of the left panel, taken from [34], Copyright (2001) by the American Physical Society.

single-cycle pulses [36, 37]. These experiments with near-single-cycle pulses allow for an easier comparison between theory and experiment. A numerical difficulty concerning the comparison of theory and experiment is accounting for the focal volume effect (FVE) in theory, which will be discussed in Chapter .3 and in Appendix C. It is an open question whether current classical models can accurately describe the observables measured in near-single cycle experiments. This is a question we address in this dissertation.

Describing NSDI in atoms driven by intense laser fields using fully ab-initio quantum mechanical techniques is still a challenging task [38]. Classical models are much faster than ab-initio calculations and have been very successful in describing NSDI. They also provide significant insights into the mechanisms underlying correlated electron dynamics in strongly-driven atoms [35, 39–42].

1.2.2 Frustrated double ionisation in molecules

Frustrated double ionisation (FDI) is one of the main processes that takes place during the fragmentation of molecules when driven by intense laser fields. Meanwhile, FDI is a possible mechanism for creating Rydberg states in atoms [43]. In frustrated ionisation, an electron first tunnel-ionises in the driving laser field. Then, this electron, at the end of the laser field, does not have enough energy to escape and it occupies an excited state of the parent ion [44]. This process was first observed by T. Nubbemeyer et al. [44] in 2008 in the context of strongly-driven He. In FDI an electron escapes and another occupies a Rydberg state at the end of the laser pulse. FDI was observed for strongly-driven H_2 [45] in 2009. The final fragments in FDI for H_2 are a neutral H atom with an electron in a Rydberg state (H^*), a H^+ ion as well as an electron in the continuum. In the experiment in Ref. [45], the correlated kinetic energy distribution of the H^* and H^+ fragments was measured, see Fig.1.3.
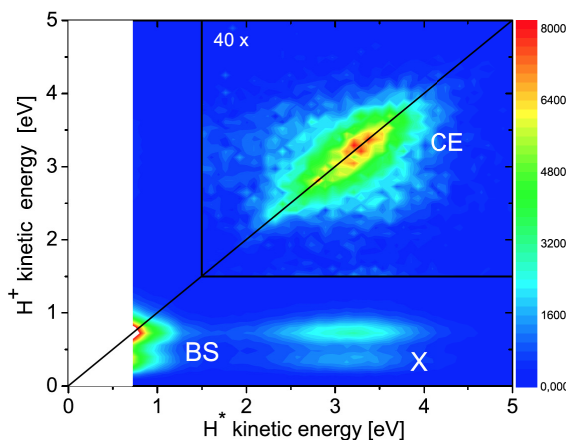
Figure 1.3: Correlated kinetic energy distribution of the excited neutral (H^*) and ion (H^+) fragment in the FDI of H_2, taken from [45], Copyright (2009) by the American Physical Society.

In Ref. [45], it was conjectured that the mechanism underlying frustrated double ionisation is as follows. An electron tunnel-ionises in the field-lowered Coulomb potential and then it escapes fast to the continuum. Then, the remaining bound electron gains energy from the field in an enhanced-like ionisation process. However, at the end of the laser field, this energy is not enough to ionise this second elec-

tron and the initially bound electron remains captured in a Rydberg state. Enhanced ionisation [11, 46–51] is a molecular effect taking place in intense laser fields. In enhanced ionisation, at a critical distance of the nuclei, a double potential well is formed such that it is easier for an electron bound to the higher potential well to tunnel to the lower potential well and subsequently ionise, see Fig.1.4. FDI has also

Enhanced ionisation
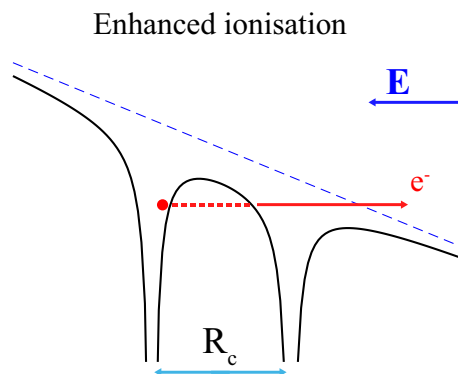
Figure 1.4: Schematic illustration of enhanced ionisation, in the context of a diatomic molecule. R_c indicates the critical internuclear distance for enhanced ionisation.

been observed in other diatomic molecules, for instance, in *Ar* dimers [52, 53] and N_2 [54] as well as in triatomic molecules H_3^+ and D_3^+ [55–59].

    Currently, quantum mechanical techniques can only address one electron in triatomic molecules in two-dimensions [60]. One reason is that the strongly-driven dynamics of two electrons and three nuclei poses an immense challenge for fully ab-initio quantum mechanical calculations. Therefore, classical and semi-classical models are very important in understanding the underlying mechanisms of FDI in molecules driven by intense laser fields [61, 62]. Employing a three-dimensional (3D) semi-classical calculation it has been shown in Ref. [61] that two major pathways contribute to FDI.

    The two pathways contributing to FDI are labelled as A and B and are illustrated in Fig.1.5 in the context of H_2. In the following, we refer to the electron that tunnel-ionises through the Coulomb barrier in the initial state as electron 1 and to the initially bound electron as electron 2. In pathway A, electron 1 tunnel-ionises,

subsequently escaping very quickly. Electron 2 tunnel-ionises later and quivers in the laser field. However, when the field is turned off, electron 2 does not have enough drift energy to escape and occupies a Rydberg state instead. Therefore, in pathway A the later ionisation step is "frustrated". This pathway is the mechanism that was conjectured to be the one responsible for FDI in the experimental work in Ref. [45]. However, the semi-classical model predicts an additional mechanism for FDI, namely, pathway B. In this latter pathway, electron 1 tunnel-ionises very quickly, quivering in the field, while electron 2 tunnel-ionises and escapes after a few periods of the laser field. When the laser field is turned off, electron 1 does not have enough energy to escape and remains in a Rydberg state of the H atom instead, i.e., the earlier ionisation step is "frustrated". In pathway B, electron-electron correlation is more important than in pathway A, since electron 1 returns to the parent molecular ion and can transfer energy to electron 2 [61]. It is still an open question
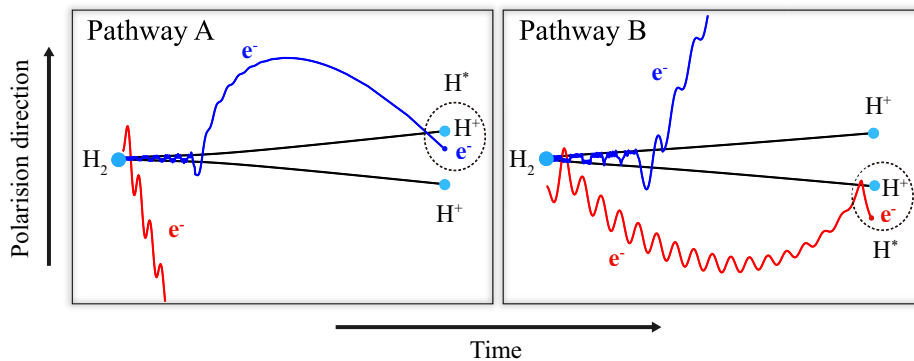
Figure 1.5: Schematic illustration of the pathways A (left panel) and B (right panel) that lead to the formation of H^* in the FDI of H_2. In the panels, we show the positions of electrons (blue and red lines) and nuclei (black lines) along the polarisation direction of the laser field as a function of time. The final fragments include a neutral H atom (H^*), a H^+ ion and an ionised electron.

what are the main mechanisms underlying FDI in strongly-driven two-electron triatomic molecules. Another open question is whether the two pathways of FDI in two-electron molecules driven by intense laser fields can be separated experimentally. These questions are addressed in this dissertation.

In this dissertation, we investigate multi-electron dynamics in atoms and multi-centre molecules driven by intense and infrared laser fields. In the first chapter, we have discussed the achievements in the field of attosecond and strong-field science focusing on non-sequential double ionisation in atoms and frustrated double ionisation in molecules. In Chapter 2, we discuss the state-of-the-art, three-dimensional, semi-classical model we employ for our studies concerning two-electron multi-centre molecules that are driven by intense laser fields. Specifically, we discuss the initial phase space conditions for the two electrons and mention the techniques we use for time propagation. In Chapter 3, we unravel the mechanisms that underlie non-sequential double ionisation in atoms when driven by near-single-cycle, intense laser fields. In addition, we compare our results for several observables with recently obtained experimental results. In Chapter 4, we investigate the pathways that contribute to frustrated double and single ionisation in strongly-driven two-electron triatomic molecules, such as D_3^+ and H_3^+. In addition, we compare our results for double and frustrated double ionisation for strongly-driven D_3^+ with experimental results. In Chapter 5, we identify a combination of perpendicularly polarised laser pulses in order to control electron-electron correlation in frustrated double ionisation in strongly-driven two-electron triatomic molecules. We conclude in Chapter 6.

Chapter 2

Semi-classical model for molecules driven by intense laser fields

As we have already discussed, semi-classical and classical models are essential for understanding the interplay of electron and nuclear motion during the fragmentation of molecules in intense laser fields. In this chapter, we describe the three-dimensional semiclassical model we employ to study ultrafast phenomena in strongly-driven two-electron triatomic molecules.

The major steps involved in the semi-classical model we employ are: i) setting up the initial conditions for the particles involved and propagating in time all the particles by solving the relevant classical equations of motion. We first address the initial conditions for the two electrons and the nuclei in a two-electron triatomic molecule. We assume that one electron tunnels through the field lowered Coulomb potential. It does so with a certain ionisation rate. In what follows we present the rates we employ as well as the initial momentum and position we assign to this electron (electron 1) once it emerges from the potential barrier. Regarding the other initially bound electron (electron 2) we assign the initial position and momentum of this electron using a micro-canonical distribution. We find this choice of initial distribution results in very good agreement of our results and experiments [45, 59, 61, 63]. In addition, using important sampling in the time interval that the laser field is switched on, we specify the time that electron 1 tunnel-ionises. This latter time is also the time that we start the propagation in time. The ionisation rate is used

as the importance sampling distribution; ii) time propagation for the two electrons and the three nuclei solving the classical equations of motion for the Hamiltonian of the strongly-driven five-body system. We solve the classical equations of motion while we fully account for the Coulomb singularities; iii) accounting for tunnelling of each electron during the time propagation. This aspect is important in order to accurately account for the enhanced ionisation process [11, 46–51].

2.1 Initial conditions in the 3D semi-classical model

2.1.1 Selecting the initial tunnel-time with importance sampling

We start the time propagation at the time t_0 that electron 1 tunnel-ionises. This time can take any value in the time interval where the laser field is switched on. We select this initial condition in a classical Monte-Carlo scheme [64–68] by generating a uniform random number in the time interval that the laser field is switched on. However, by doing so we generate initial times that are equally spread around time intervals corresponding to small and large ionisation rates. Therefore, to improve the efficiency of our computations, we select the initial time t_0 using importance sampling [69] with the ionisation rate as the distribution function. Generally, the idea of using importance sampling to compute the integral

$$I = \int g(t)dt \tag{2.1}$$

is instead of sampling the variable t is to sample W, where $f(t)dt = dW$, re-expressing the integral as follows

$$I = \int \frac{g(t)}{f(t)}f(t)dt = \int \frac{g(t)}{f(t)}dW. \tag{2.2}$$

f(t) is labeled as the "importance sampling distribution". In our semi-classical model, the importance sampling distribution is the ionisation rate Γ.

The steps involved in selecting t_0 are as follows:

1. computing W_{max} by integrating the ionisation rate $\Gamma(t)$ over the duration of the laser field $[t_a, t_b]$:

$$W_{max} = \int_{t_a}^{t_b} \Gamma(t)dt; \tag{2.3}$$

2. Selecting a uniform random number W in the interval $[0, W_{max}]$. The corresponding initial time t_0 is obtained by solving

$$W = \int_{t_a}^{t_0} \Gamma(t)dt. \tag{2.4}$$

This process is repeated for a large number of times in order to accurately sample the time interval where the laser field is switched on.

2.1.2 Initial conditions for the tunnel-ionising electron

2.1.2.1 Ionisation rate

We assume that, initially, electron 1 tunnel-ionises through the field lowered Coulomb barrier. This is a quantum mechanical process. The ionisation rate has been extensively addressed in the literature and has been formulated using semi-classical models for atoms [25, 70] and molecules [71–73].

2.1.2.1.1 Ionisation rate for atoms: ADK theory

The Ammosov-Delone-Krainov (ADK) theory was formulated first for the ionisation rate of the hydrogen atom. It was then extended to describe other atoms by using the effective principal and orbital quantum numbers [25]. In the ADK theory, the ionisation rate for a field strength E is given by [25, 70, 74]:

$$\Gamma(E) \;\; = \;\; C_{n^*l^*}^2 N(l,m)\frac{\kappa^2}{2}\left(\frac{2\kappa^3}{E}\right)^{2n^*-|m|-1}\exp\left(-\frac{2\kappa^3}{3E}\right) \tag{2.5}$$

with

$$N(l,m) = \frac{(2l+1)(l+|m|!)}{2^{|m|}(|m|)!(l-|m|)!}, \tag{2.6}$$

$$C^2_{n^*l^*} = \left[\frac{1}{2\pi n^*} \left(\frac{4e^2}{n^{*2} - l^{*2}} \right)^{n^*} \left(\frac{n^* - l^*}{n^* + l^*} \right)^{l^*+1/2} \right]^{\frac{1}{2}} \tag{2.7}$$

$$\approx \left(\frac{2e}{n^*} \right)^{n^*} \frac{1}{(2\pi n^*)^{1/2}} \quad \text{for} \quad n^* \gg l^*, \tag{2.8}$$

where e is Euler's number, E is the field strength, $\kappa = \sqrt{2I_p}$ and I_p is the ionisation potential of the atom under consideration. $n^* = \frac{Z^*}{\sqrt{2I_p}}$ is the effective principal quantum number while l^* and m are the effective orbital quantum number and magnetic quantum number, respectively. The ADK ionisation rates compare well with experimental results for atoms such as *Kr*, *He*, *Ne*, *Xe* and *Ar*, see Ref. [70, 75].

For high intensities where the Coulomb barrier is sufficiently suppressed so that electron 1 escapes classically over-the-barrier, i.e. for the over-the-barrier intensity regime, the ADK formula no longer agrees well with experimental results [76]. To correct the ADK ionisation rate for field strengths above a critical value

$$E_b = \frac{\kappa^4}{16Q_c}. \tag{2.9}$$

a simple empirical method was proposed by Tong et al. in 2005 [77]:

$$\Gamma_{BSI}(E) = \Gamma(E) \exp \left(-\alpha \frac{Q_c^2}{I_p} \frac{E}{\kappa^3} \right), \tag{2.10}$$

where $\Gamma(E)$ is the ionisation rate given by the ADK theory. α is an empirical parameter that has been computed by fitting Eq.2.10 to quantum mechanical rates that are obtained using the single-active-electron approximation [77].

2.1.2.1.2   Ionisation rate for molecules: MO-ADK theory

An analytical expression for the ionisation rate of molecules was proposed by C.D. Lin in 2002, termed as molecular ADK (MO-ADK) theory [71]. In this derivation the molecular frame is denoted by (X, Y, Z). The electric field is consid-

ered along the Z direction. Next, the wave-function of the ionising electron in the molecular frame is expressed using the single-centre-expansion [78]

$$\Psi(\mathbf{r}) = \sum_{lm} F_{lm}(r) Y_{lm}(\hat{r}) \tag{2.11}$$

with m the magnetic quantum number and $Y_{lm}(\hat{r})$ the spherical harmonics. The radial wave function in the asymptotic region satisfies

$$F_{lm}(r \to \infty) \approx C_{lm} r^{Q_c/\kappa - 1} e^{-\kappa r} \tag{2.12}$$

with Q_c being the asymptotic Coulomb charge and with C_{lm} parameters that are obtained by fitting the wave function in the asymptotic region. The relevant ionisation rate of the tunnelling electron is given by [79, 80]

$$\Gamma(E) = \sum_m \frac{B^2(m)}{2^{|m|}|m|!} \frac{1}{\kappa^{2Q_c/\kappa - 1}} \left(\frac{2\kappa^3}{E} \right)^{2Q_c/\kappa - |m| - 1} e^{-2\kappa^3/3E}, \tag{2.13}$$

where E is the field strength and

$$B(m) = \sum_l (-1)^l C_{lm} Q(l,m) \tag{2.14}$$

with

$$Q(l,m) = (-1)^m \sqrt{\frac{(2l+1)(l+|m|)!}{2(l-|m|)!}}. \tag{2.15}$$

A general direction of the laser field defined in the lab fixed-frame (X_L, Y_L, Z_L), is accounted for in the ionisation rate by defining the Euler angles between the lab frame and the molecular frame. The Euler angles are $\mathbf{R} \equiv (\phi, \theta, \chi)$, where θ is the angle between the axes Z_L and Z; ϕ and χ denote the rotations around the Z axis and the Z_L axis, respectively. The general expression for the ionisation rate is given

by

$$\Gamma(E,\mathbf{R}) = \sum_{m'} \frac{|B(m')|^2}{2^{|m'|}|m'|!} \frac{1}{\kappa^{2Z_c/\kappa - 1}} \left(\frac{2\kappa^3}{E}\right)^{2Q_c/\kappa - |m'| - 1} e^{-2\kappa^3/3E}, \qquad (2.16)$$

with $B(m')$ expressed as

$$B(m') = \sum_{lm} (-1)^l C_{lm} D_{m',m}^l(\mathbf{R}) Q(l,m') \qquad (2.17)$$

and the Wigner rotation matrix given by [79]

$$D_{m',m}^l(\mathbf{R}) = e^{im'\phi} d_{m',m}^l(\theta) e^{im\chi}. \qquad (2.18)$$

Note that in deriving Eq.2.16 the electron is assumed to ionise opposite to the direction of the laser field [80].

2.1.2.1.3 A semi-classical ionisation rate for molecules

Another method to compute the ionisation rate for molecules was proposed by Murray et al. in 2011 [73]. This method better accounts for the molecular structure. In this method, the ionisation rate is expressed as [62, 73]

$$\Gamma(E,\theta) = \Gamma_{as}(E)R(\theta) \qquad (2.19)$$

with

$$\Gamma_{as}(E) = 2\pi\kappa^2 C_\kappa^2 \left(\frac{2\kappa^3}{E}\right)^{2Q_c/\kappa - 1} exp\left(-\frac{2\kappa^3}{3E}\right) \qquad (2.20)$$

$$R(\theta) = \left[F_0(\theta) - \frac{4E}{3\kappa^3}F_2(\theta) + \frac{2E}{3\kappa^3}F_3(\theta)\right]^2 + \frac{2E}{9\kappa^3}F_1^2(\theta), \qquad (2.21)$$

where E is the instantaneous field strength, θ is the angle between the laser field and the z axis in the molecular frame and Q_c is the asymptotic charge. The coefficient C_k is obtained by fitting the Dyson orbital [81] describing the tunnel-ionising electron

to its asymptotic wave function

$$\psi(r,\theta,\phi) \approx C_\kappa \kappa^{3/2} (r\kappa)^{Q/\kappa-1} e^{-\kappa r} F(\cos\theta, \sin\theta\cos\phi) \qquad (2.22)$$

where r, θ and ϕ are the spherical coordinates in the molecular frame. The Dyson orbital is the overlap integral of the two-electron wave function of the molecule with the one-electron wave function of the molecular ion. The function $F(\cos\theta, \sin\theta\cos\phi)$ is chosen to best fit the angular dependence of the wave function at large distance r. The functions $F_i(\theta)$ $(i = 0, 1, 2, 3)$ are given by

$$
\begin{aligned}
F_0(\theta) &= F(\cos\theta, \sin\theta) \\
F_1(\theta) &= F_v \cos\theta - F_u \sin\theta \\
F_2(\theta) &= F_u \cos\theta + F_v \sin\theta \\
F_3(\theta) &= F_{vv} \cos^2\theta + F_{uu} \sin^2\theta - F_{uv} \sin 2\theta_L
\end{aligned}
\qquad (2.23)
$$

where F_v, F_u, F_{vv} and F_{uu} is the first and second order partial derivatives of $F(u, v)$ with respect to u and v, calculated at $u = \cos\theta$ and $v = \sin\theta$. The function $F(\cos\theta, \sin\theta\cos\phi)$ depends on the molecular orbital the electron occupies before tunnelling.

To obtain $F(\cos\theta, \sin\theta\cos\phi)$, for instance, for the molecule H_3^+, the ground state of H_3^+ is approximated by a linear combination of $1s$ atomic orbitals [62]

$$\Phi(\mathbf{r}) \propto e^{-\kappa|\mathbf{r}-\mathbf{R}_a|} + e^{-\kappa|\mathbf{r}-\mathbf{R}_b|} + e^{-\kappa|\mathbf{r}-\mathbf{R}_c|}, \qquad (2.24)$$

where $\mathbf{R}_a$, $\mathbf{R}_b$ and $\mathbf{R}_c$ indicate the positions of the nuclei of H_3^+. Taking the asymptotic expansion for $r \gg R$, with R the internuclear distances, it is found

$$
\begin{aligned}
F(cos\theta, sin\theta cos\phi) &\approx 2\cosh(\kappa R cos\theta/2)\exp\left(-\kappa R sin\theta cos\phi/(2\sqrt{3})\right) \\
&\quad + \exp\left(\kappa R sin\theta cos\phi/\sqrt{3}\right).
\end{aligned}
\qquad (2.25)
$$

By fitting the Dyson orbital in the interval $3 \le r \le 6$, $0 \le \theta \le \pi$ and $0 \le \phi \le 2\pi$ [62]

C_κ is found equal to 0.139761.

A comparison of the ionisation rates of H_3^+ obtained by the MO-ADK theory [71] and by the method developed by Murray et al. [73] is shown in Fig.2.1 in atomic units. Atomic units are used throughout this dissertation unless stated otherwise. These rates are computed as a function of intensity for $\theta = 0$ (left panel) and as a function of the angle θ at an intensity of $3.5 \times 10^{14} W/cm^2$ (right panel). A good agreement is found between the two methods for H_3^+.
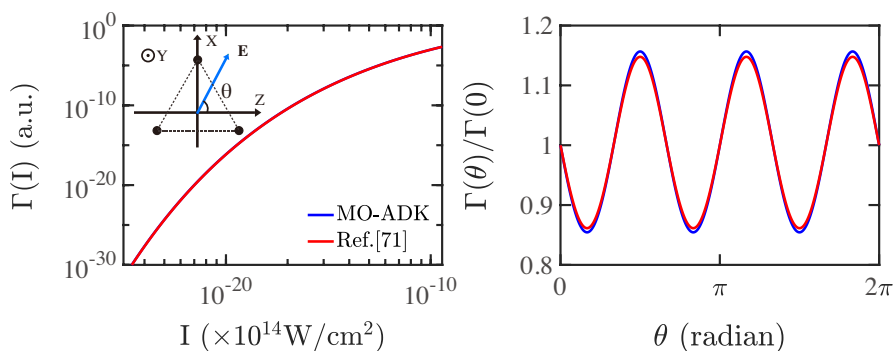
Figure 2.1: The ionisation rate of H_3^+ calculated with the MO-ADK method [71] and Ref. [73] as a function of intensity for $\theta = 0$ (left panel) and as a function of the angle θ at an intensity of 3.5×10^{14} W/cm^2 (right panel).

2.1.3   Exit point in the field-lowered Coulomb barrier

Depending on the strength of the laser field, electron 1 either tunnel-ionises through the field-lowered Coulomb potential, i.e. tunnelling intensity regime, or escapes classically over the Coulomb barrier, i.e. over-the-barrier intensity regime. For the tunnelling intensity regime, following the formulation in Ref. [62], we specify first the point where electron 1 exits through the potential barrier. We assume that the electron always exits the potential barrier along the axis of the electric field. Electron 1 can exit the potential barrier along the axis of the laser field but at different distances perpendicular to the electric field. We assume that electron 1 exits along the axis that corresponds to the lowest maximum value of the potential barrier. Once this perpendicular shift r_s has been identified, then, we find the distance

r_e in the direction opposite to the direction of the laser field that is determined by solving

$$-\sum_{i=1}^{N_n} \frac{eQ_i}{r_{1,i}} + K_{ee}(\mathbf{r}_1) - r_e|\mathbf{E}| + I_p = 0, \tag{2.26}$$

where $\mathbf{r}_1 = -r_e\frac{\mathbf{E}}{|\mathbf{E}|} + r_s\frac{\mathbf{E}_\perp}{|\mathbf{E}|}$, see Fig.2.2 and the subscripts i denotes the different nuclei. N_n is the number of nuclei in the molecule, which is taken equal to two or three. Q_i is the charge of the nucleus i and r_{1i} denotes the distance between the nucleus i and electron 1. The integral K_{ee} is given by

$$K_{ee}(\mathbf{r}_1) = \int d\mathbf{r}_2 \frac{|\Phi(\mathbf{r}_2)|^2}{|\mathbf{r}_1 - \mathbf{r}_2|} \tag{2.27}$$

and accounts for the Coulomb repulsion between the initially tunnel-ionising electron (electron 1) and the initially bound electron (electron 2). $\mathbf{r}_2$ is the position vector of the initially bound electron. Once r_e is obtained the coordinates of the exit point are given by

$$
\begin{aligned}
r_{tx} &= -r_e sin(\theta) + r_s cos(\theta) \\
r_{ty} &= 0 \\
r_{tz} &= -r_e cos(\theta) - r_s sin(\theta),
\end{aligned}
\tag{2.28}
$$

where θ is the angle of the electric field with the z axis.
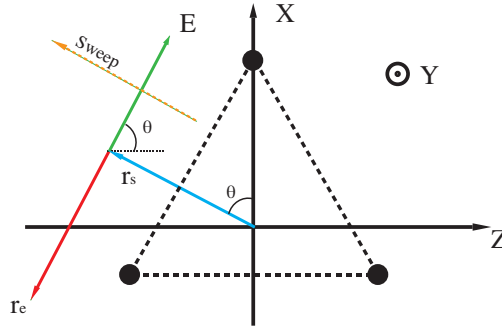
Figure 2.2: Illustration of the parallel (r_e)and perpendicular (r_s) to the laser field components of the exit point for electron 1.

Regarding the initial momentum, we assume that electron 1 exits the potential barrier with zero momentum along the direction of the electric field. For the direction perpendicular to the laser field, we assume that the momentum of electron 1 follows a Gaussian distribution [70, 82]:

$$w_\perp(v_\perp) = \frac{\kappa}{\pi} \frac{v_\perp}{E} \exp\left(-\frac{v_\perp^2 \kappa}{E}\right).$$ (2.29)

To fully define the components of the vertical component of the momentum, the polar angle ϕ needs to be specified. The latter is generated as a uniform random number in the interval $[0, 2\pi]$. Moreover, for $v_\perp$ we also generate a uniform random number in the velocity interval where the distribution $w_\perp(v_\perp)$ is non zero. The above described distribution for the initial momentum of electron 1 has been recently verified experimentally for strongly-driven *Ar* [83]. For the general case that the electric field forms an angle θ with respect to the z axis the coordinates of the initial momentum of electron 1 are given by

$$\begin{aligned} v_{tx} &= v_\perp cos(\phi)cos(\theta) \\ v_{ty} &= v_\perp sin(\phi) \\ v_{tz} &= -v_\perp cos(\phi)sin(\theta). \end{aligned}$$ (2.30)

For the above-the-barrier intensity regime, electron 1 has enough energy to escape over the field-lowered Coulomb barrier. Following the formulation in Ref. [62], we assume that electron 1 initially starts at the position where the maximum of the potential barrier is located, r_{1max}. Moreover, we assume that it ionises with energy equal to the difference between the first ionisation energy I_p of the molecule and the maximum value of the potential barrier:

$$\Delta E = I_p - \sum_{i=1}^{N_n} \frac{eQ_i}{r_{1max,i}} + K_{ee}(\mathbf{r}_{1max}) - r_{e_{max}}|\mathbf{E}|,$$ (2.31)

where $\mathbf{r}_{1max}$ is the position of the barrier maximum. Thus, the amplitude of the

initial momentum of electron 1 is given by

$$v_{ovb} = \sqrt{2\Delta E}. \tag{2.32}$$

We also assume that electron 1 escapes with momentum in the direction opposite to the laser field which, assuming the electric field is along the z axis, is given by

$$
\begin{aligned}
v'_{ovbx} &= v'_{ovb}cos(\phi)\sqrt{1-\vartheta^2} \\
v'_{ovby} &= v'_{ovb}sin(\phi)\sqrt{1-\vartheta^2} \\
v'_{ovbx} &= v'_{ovb}\vartheta,
\end{aligned}
\tag{2.33}
$$

where $\phi \in [0,2\pi]$ is the azimuthal angle in spherical coordinates and $\vartheta \in [-1,0]$ is the polar angle restricted in the direction opposite to the electric field. Uniform random numbers in these intervals are assigned to these angles for the initial state of electron1. For a general direction of the laser field the initial momentum of electron 1 is given by:

$$
\begin{aligned}
v_{ovbx} &= v'_{ovbx}cos(\theta)+v'_{ovbz}sin(\theta) \\
v_{ovby} &= v'_{ovby} \\
v_{ovbz} &= v'_{ovbz}cos(\theta)-v'_{ovbx}sin(\theta).
\end{aligned}
\tag{2.34}
$$

2.1.4 Initial conditions for the bound electron

We assume that the initially bound electron is described by a one-electron micro-canonical distribution

$$f(\mathbf{r},\mathbf{p}) \propto \delta\left[-I_p - \frac{p^2}{2} - V\right] \tag{2.35}$$

where V is the Coulomb potential of the bound electron with respect to the nuclei. One electron micro-canonical distributions have been previously developed for atoms [84], for diatomic molecules [85]. These distributions have been used to

describe the initial state for studies of particle impact induced fragmentation [84, 85] and for ionisation processes in two-electron atoms and diatomic molecules driven by intense laser fields [35, 39, 42, 61, 86–88]. A one-electron micro-canonical distribution for triatomic molecules has been recently developed by Lazarou and Emmanouilidou [89]. In what follows we first present the one-electron micro-canonical distribution for diatomic molecules, since it is used as the basis to develop the one-electron micro-canonical distribution for triatomic molecules, which we present afterwards.

2.1.4.1   Micro-canonical distribution for diatomic molecules

A micro-canonical distribution for diatomic molecules was developed by R. E. Olson et al. in 1989 [85]. In what follows we describe the one-electron micro-canonical distribution for diatomic molecules since it is used as a stepping stone to derive in the next section the one-electron micro-canonical distribution for triatomic molecules. We denote the position vectors of the two nuclei A and B by $\mathbf{R}_A = \left(0,0,-\frac{R_{AB}}{2}\right)$ and $\mathbf{R}_B = \left(0,0,\frac{R_{AB}}{2}\right)$ and the inter-nuclear distance by R_{AB}. We denote the position vector of the electron by r and the distances of the electron from the nuclei A, B by $r_A = |\mathbf{r} - \mathbf{R}_A|$, $r_B = |\mathbf{r} - \mathbf{R}_B|$. We then define the confocal elliptical coordinates ξ and η using the nuclei A and B as the foci of the ellipse, that is,

$$\xi = \frac{1}{R_{AB}}(r_A + r_B) \tag{2.36}$$

$$\eta = \frac{1}{R_{AB}}(r_A - r_B), \tag{2.37}$$

where $\xi \in [1, \xi_{max}]$, $\eta \in [-1,1]$. The third coordinate $\phi_r = arctan(\frac{y}{x}) \in [0,2\pi]$ is the angle between the projection of the position vector r on the x-y plane and the positive x axis; it thus defines the rotation angle around the axis that goes through the nuclei A and B. The potential of the electron in the presence of the nuclei A and B which have charges Q_A and Q_B, respectively, is given by

$$V(r_A, r_B) = -\frac{Q_A}{r_A} - \frac{Q_B}{r_B}. \tag{2.38}$$

This potential is expressed in terms of the confocal elliptical coordinates as follows

$$V(\xi,\eta) = -\frac{2}{R_{AB}}\frac{(Q_A+Q_B)\xi-(Q_A-Q_B)\eta}{\xi^2-\eta^2}. \tag{2.39}$$

Note that the energy is given by $E = p^2/2 + V$. The electron momentum in terms of the confocal elliptical coordinates is expressed as follows

$$
\begin{aligned}
p_x &= \sqrt{2(E-V(\xi,\eta))}\cos(\phi_p)\sqrt{1-v_p^2}, \\
p_y &= \sqrt{2(E-V(\xi,\eta))}\sin(\phi_p)\sqrt{1-v_p^2}, \\
p_z &= \sqrt{2(E-V(\xi,\eta))}v_p,
\end{aligned}
\tag{2.40}
$$

where $\phi_p \in [0,2\pi]$ and $v_p \in [-1,1]$ define the momentum $\mathbf{p}$ in spherical coordinates.

Transforming from $(\mathbf{r},\mathbf{p}) \to (\xi,\eta,\phi_r;E,v_p,\phi_p)$, the Jacobian determinant is given by

$$J = \left(\frac{R_{AB}}{2}\right)^3\sqrt{2(-I_p-V(\xi,\eta))(\xi^2-\eta^2)}, \tag{2.41}$$

resulting in the following micro-canonical distribution:

$$
\begin{aligned}
f(\xi,\eta,\phi_r;E,v_p,\phi_p) &\propto J\delta(-I_p-E) & (2.42) \\
&= \left(\frac{R_{AB}}{2}\right)^3\sqrt{2(-I_p-V(\xi,\eta))(\xi^2-\eta^2)}\delta(-I_p-E). & (2.43)
\end{aligned}
$$

Integrating $f(\xi,\eta,\phi_r;E,v_p,\phi_p)$ over $E \in (-\infty,0)$, ϕ_p and v_p we find

$$\rho(\xi,\eta) \propto \begin{cases} (\xi^2-\eta^2)\sqrt{-I_p-V(\xi,\eta)} & -I_p \geq V \\ 0 & -I_p < V. \end{cases} \tag{2.44}$$

To set up the initial conditions, we find ξ_{max} so that $\frac{p^2}{2} = -I_p - V(\xi,\eta) \geq 0$. We then find the maximum value ρ_{max} of the distribution $\rho(\xi,\eta)$. To create initial conditions using the one-electron micro-canonical distribution we implement the

following steps:

1. Generate the uniform random numbers $\xi \in [1, \xi_{max}]$, $\eta \in [-1, 1]$ and $\chi \in [0, \rho_{max}]$.

2. Accept the generated values as initial conditions if $\rho(\xi, \eta) > \chi$, otherwise reject these values.

3. Repeat the above process.

2.1.4.2 Micro-canonical distribution for triatomic molecules

In this section, we describe the one-electron micro-canonical distribution formulated by C. Lazarou and A. Emmanouilidou for a general one-electron triatomic molecule [89].
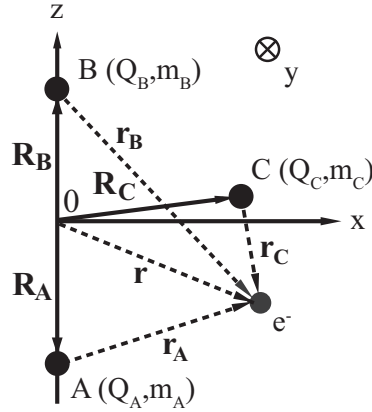
Figure 2.3: The configuration of the triatomic molecule we use to set-up the micro-canonical distribution.

We denote the positions of the nuclei by $\mathbf{R}_A = (0, 0, -R_{AB}/2)$, $\mathbf{R}_B = (0, 0, R_{AB}/2)$ and $\mathbf{R}_C = (x_C, 0, z_C)$, and the inter-nuclear distances by R_{AB}, R_{BC} and R_{AC}. The coordinates of the nucleus C are expressed in terms of the inter-nuclear distances as follows

$$z_C = \frac{R_{AC}^2 - R_{BC}^2}{2R_{AB}} \tag{2.45}$$

$$x_C = \pm\sqrt{R_{AC}^2 - \left(\frac{R_{AC}^2 - R_{BC}^2 + R_{AB}^2}{2R_{AB}}\right)^2}. \tag{2.46}$$

We denote the position vector of the electron by **r** and the distances of the electron from the nuclei A, B and C by $r_A = |\mathbf{r} - \mathbf{R}_A|$, $r_B = |\mathbf{r} - \mathbf{R}_B|$ and $r_C = |\mathbf{r} - \mathbf{R}_C|$, respectively. The configuration of the one-electron molecule used to derive the micro-canonical distribution is shown in Fig.2.3. We then define the confocal elliptical coordinates ξ and η as

$$\xi = \frac{1}{R_{AB}}(r_A + r_B) \tag{2.47}$$

$$\eta = \frac{1}{R_{AB}}(r_A - r_B), \tag{2.48}$$

where $\xi \in [1, \xi_{max}]$, $\eta \in [-1, 1]$. The third coordinate $\phi_r = arctan(\frac{y}{x}) \in [0, 2\pi]$ is the angle between the projection of the position vector *r* on the *x-y* plane. The potential of the electron in the presence of the nuclei A, B and C with charges Q_A, Q_B and Q_C, is given by

$$V(r_A, r_B, r_C) = -\frac{Q_A}{r_A} - \frac{Q_B}{r_B} - \frac{Q_C}{r_C}. \tag{2.49}$$

This potential is then expressed in terms of the confocal elliptical coordinates as follows

$$V(\xi, \eta, \phi) = -\frac{2}{R_{AB}}\left[\frac{Q_A}{\xi + \eta} + \frac{Q_B}{\xi - \eta} + Q_C \left((\xi^2 + \eta^2 - 1) - \frac{4z_C}{R_{AB}}\xi\eta - \right.\right.$$
$$\left.\left. \frac{4x_C}{R_{AB}}\cos(\phi)\sqrt{(\xi^2 - 1)(1 - \eta^2)} + \frac{4(x_C^2 + z_C^2)}{R_{AB}^2} \right)^{-\frac{1}{2}} \right]. \tag{2.50}$$

As for the diatomic case, the electron momentum in terms of the confocal elliptical coordinates is expressed as follows

$$p_x = \sqrt{2(E - V(\xi, \eta, \phi))}\cos(\phi_p)\sqrt{1 - v_p^2},$$
$$p_y = \sqrt{2(E - V(\xi, \eta, \phi))}\sin(\phi_p)\sqrt{1 - v_p^2}, \tag{2.51}$$
$$p_z = \sqrt{2(E - V(\xi, \eta, \phi))}v_p,$$

Transforming from $(\mathbf{r}, \mathbf{p}) \rightarrow (\xi, \eta, \phi_r; E, v_p, \phi_p)$, the Jacobian determinant

takes the form

$$J = \left(\frac{R_{AB}}{2}\right)^3 \sqrt{2(-I_p - V(\xi, \eta, \phi))}(\xi^2 - \eta^2). \tag{2.52}$$

Thus, the one-electron micro canonical distribution is given by

$$f(\xi, \eta, \phi_r; E, \nu_p, \phi_p) \quad \propto \quad J\delta(-I_p - E) \tag{2.53}$$

$$= \quad \left(\frac{R_{AB}}{2}\right)^3 \sqrt{2(-I_p - V(\xi, \eta, \phi))}(\xi^2 - \eta^2)\delta(-I_p - E) \tag{2.54}$$

Integrating $f(\xi, \eta, \phi_r; E, \nu_p, \phi_p)$ over $E \in (-\infty, 0)$, ϕ_p and ν_p we find

$$\rho(\xi, \eta, \phi) \propto \begin{cases} (\xi^2 - \eta^2)\sqrt{-I_p - V(\xi, \eta, \phi)} & -I_p \geq V \\ 0 & -I_p < V. \end{cases} \tag{2.55}$$

The distribution ρ goes to zero when the electron is placed on top of either nucleus A or B and it is thus well-behaved in these cases. However, when the electron is placed on top of nucleus C, i.e. when $\mathbf{r} \to \mathbf{R}_C$, $\rho(\xi, \eta, \phi) \to \infty$. We eliminate this singularity by introducing an additional transformation. Setting $\xi = \xi_C = (R_{AC} + R_{BC})/R_{AB}$, $\phi = 0$ and expanding $\rho(\xi_c, \eta, 0)$ around $\eta_C = (R_{AC} - R_{BC})/R_{AB}$, we find

$$\rho(\xi_C, \eta, 0) \propto \frac{1}{|\eta - \eta_C|^{1/2}}, \tag{2.56}$$

where ξ_C and η_C are the values of ξ and η, respectively, when the electron is placed on top of nucleus C. To eliminate the singularity in Eq.2.56, we introduce a new variable t with $t^\gamma = \eta - \eta_C$. So the limit of t is $t_{min} = -(1 + \eta_c)^{1/\gamma}$ and $t_{max} = (1 - \eta_c)^{1/\gamma}$. Then the total Jacobian determinant for both transformations is

$$J \quad = \quad 2^{\frac{1}{\gamma} - 4}\gamma(R_{AB})^3|t^{\gamma-1}|\sqrt{2(-I_p - V(\xi, \eta, \phi))}\left(\xi^2 - (t^\gamma + \xi_C)^2\right). \tag{2.57}$$

The new distribution takes the form

$$
\rho\left(\xi,t,\phi\right) \propto
\begin{cases}
|t^{\gamma-1}|\left(\xi^2 - (t^\gamma + \xi_C)^2\right)\sqrt{P(\xi,t,\phi)} & P \geq 0 \\[2mm]
0 & P < 0,
\end{cases}
\tag{2.58}
$$

with

$$
\begin{aligned}
P(\xi,t,\phi) &= -I_p - V(\xi,t,\phi) && (2.59)\\
&= -I_p + \frac{2}{R_{AB}}\left[\frac{Q_A}{\xi + t^\gamma + \eta_C} + \frac{Q_B}{\xi - t^\gamma - \eta_C} + \right.\\
&\quad Q_C\left((\xi^2 + (t^\gamma + \eta_C)^2 - 1) - \frac{4z_C}{R_{AB}}\xi(t^\gamma + \eta_C) - \right.\\
&\quad \left.\left.\frac{4x_C}{R_{AB}}\cos(\phi)\sqrt{(\xi^2-1)(1-(t^\gamma+\eta_C)^2)} + \frac{4(x_C^2 + z_C^2)}{R_{AB}^2}\right)^{-\frac{1}{2}}\right]. && (2.60)
\end{aligned}
$$

Since $\eta \in [-1,1]$, t^γ and t take both negative and positive values and there-fore, if we choose one γ for all values of η, γ must be odd. Moreover, to avoid the singularity when the electron is placed on top of nucleus C, γ must be such that $t^{\gamma-1}/t^{\gamma/2} \to 0$, i.e., $\gamma \geq 2$. Combining the above two conditions, yields $\gamma = 3,5,7,....$. The new distribution $\rho(\xi,t,\phi)$ goes to zero when the electron is placed on top of nucleus C, i.e. when $\xi = \xi_C$, $t = 0$ and $\phi = 0, 2\pi$.

To set up the initial conditions, we find ξ_{max} so that $\frac{p^2}{2} = -I_p - V(\xi,t,\phi) \geq 0$ and equivalently $P(\xi,t,\phi) \geq 0$. We then find the maximum value ρ_{max} of the distribution $\rho(\xi,t,\phi)$. To create initial conditions using the one-electron micro-canonical distribution we implement the following steps:

1. Generate the uniform random numbers $\xi \in [1, \xi_{max}]$, $t \in [-t_{min}, t_{max}]$, $\phi \in [0, 2\pi]$ and $\chi \in [0, \rho_{max}]$.

2. Accept the generated values as initial conditions if $\rho(\xi,t,\phi) > \chi$, otherwise reject these values.

3. Repeat the above process.

Following the above described formulation, we obtain the initial conditions of the electron with respect to the origin of the coordinate system as shown in

Fig.2.3. To obtain the initial conditions for the position of the electron with respect to the centre of mass of the triatomic molecule, $\mathbf{r}'$, in terms of the ones with respect to the origin, $\mathbf{r}$, we shift the coordinates by $\mathbf{r}' = \mathbf{r} - \mathbf{R_{cm}}$, where $\mathbf{R_{cm}}$ is given by $(X_{cm}, 0, Z_{cm})$ with

$$X_{cm} = \frac{m_C x_c}{m_A + m_B + m_C} \tag{2.61}$$

$$Z_{cm} = \frac{R_{ab}(m_B - m_A)/2 + m_C z_c}{m_A + m_B + m_C}, \tag{2.62}$$

with m_A, m_B and m_C the masses of the nuclei.

2.1.4.3   Comparison of quantum mechanical calculation and micro-canonical distribution

Finally, using the one-electron micro-canonical distribution that we have formulated above, we compute the position and momentum probability densities of the initially bound electron for H_2^+ and H_3^{2+}. We do so for the ground state of H_2 and H_3^+ with the internuclear distances 1.4 a.u. and 1.65 a.u. [90], respectively. The ionisation potentials for H_2^+ and H_3^{2+} are 1.28 a.u. and 1.93 a.u., respectively, obtained using the quantum chemistry package MOLPRO [91].

First, in the top panels of Fig.2.4, we plot the probability density of the position of the electron on the x-z plane for $y = 0$. We compare this micro-canonical distribution with the quantum probability density in the bottom panels for H_2^+ and H_3^{2+}. That is, to obtain the quantum probability density, we plot $|\Psi(x, 0, z)|^2$, where $\Psi(\mathbf{r})$ is the quantum mechanical wave function for the molecules, which is obtained using MOLPRO. It shows that the two probability densities of the electron position compare well. However, the micro-canonical probability density underestimates the electron density between the nuclei while it overestimates the one around the nuclei.

In addition, using the micro-canonical distribution, for all values of the electron momentum component along the y-axis, p_y, we plot the probability density of the electron momentum on the p_x-p_z plane in the top panels of Fig.2.5. We compare
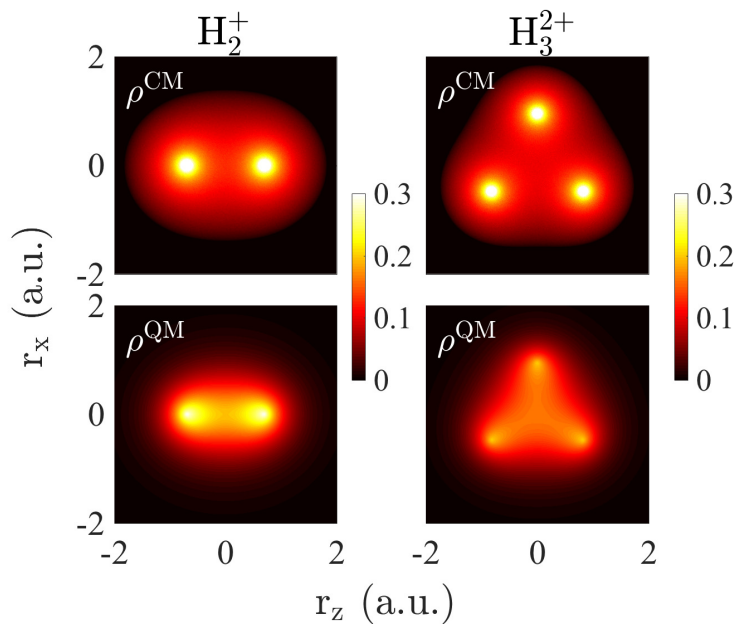
Figure 2.4: Top panels: the micro-canonical probability density (ρ^{CM}) of the electron position on the x-z plane for $y = 0$ for H_2^+ and H_3^{2+}; Bottom panels: the quantum mechanical probability density (ρ^{QM}) of the electron position on the x-z plane for $y = 0$ for H_2^+ and H_3^{2+}.
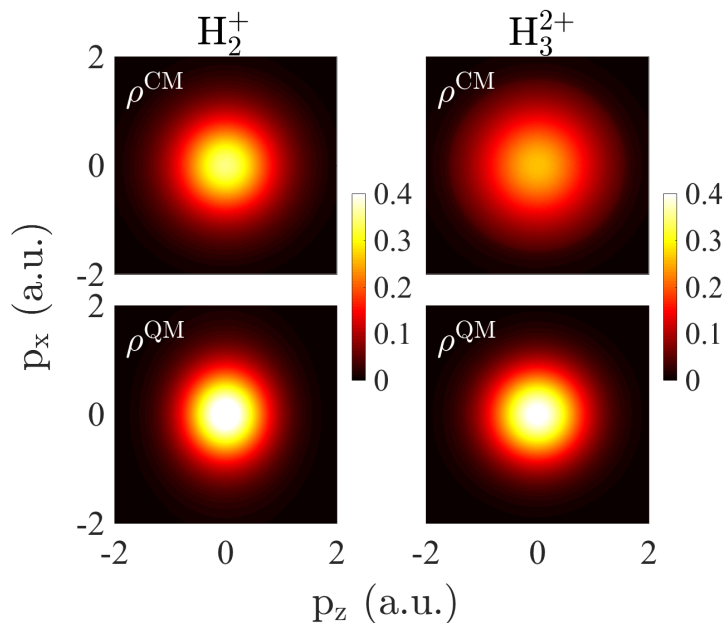
Figure 2.5: Top panels: the micro-canonical probability density (ρ^{CM}) of the electron momentum plotted on the $p_x - p_z$ plane for all values of p_y; Bottom panels: the quantum mechanical probability density (ρ^{QM}) of the electron momentum on the p_x-p_z plane for all values of p_y.

this distribution with its quantum mechanical analog $\rho^{QM}(p_x, p_z)$. The latter is plotted in the bottom panels of Fig.2.5. To obtain $\rho^{QM}(p_x, p_z)$, we, first, compute the quantum mechanical wave function in momentum space

$$\Phi(\mathbf{p}) = \frac{1}{(2\pi)^{3/2}} \int \Psi(\mathbf{r}) e^{-i\mathbf{p}\mathbf{r}} d\mathbf{r}, \tag{2.63}$$

and we, next, integrate over p_y

$$\rho^{QM}(p_x, p_z) = \int_{-\infty}^{\infty} |\Phi(\mathbf{p})|^2 dp_y. \tag{2.64}$$

The plots in Fig.2.5 show that the two probability densities for the electron momentum compare well. However, the micro-canonical probability density overestimates the higher values of the electron momentum. It is consistent with the result in Fig.2.4, where the micro-canonical probability density overestimates the electron position around the nuclei.

2.2 Propagation method

The technique we use to propagate in time was described in detail in Ref. [62] and references therein. Briefly, this 3D propagation technique accounts for the accurate treatment of the Coulomb singularity. This is an essential component of an accurate classical treatment, since classically an electron can come infinitely close to the nucleus. The main steps in the 3D propagation technique that we employed for our calculation are i) formulating the equations of motion for the five-body Hamiltonian in a strong laser field using the global regularisation scheme described in Ref. [92]; ii) using a time transformed leapfrog propagation technique in conjunction with the Bulirsch-Stoer method.

2.2.1 Global regularisation of N-body problem

The global regularisation scheme is described as follows [92]. The Hamiltonian of an N-body system interacting with the laser field is expressed as

$$H = \sum_{i=1}^{N} \frac{\mathbf{p}_i^2}{2m_i} + \sum_{i=1}^{N-1} \sum_{j=i+1}^{N} \frac{Q_i Q_j}{|\mathbf{r}_i - \mathbf{r}_j|} - \sum_{i=1}^{N} Q_i \mathbf{E}(t) \cdot \mathbf{r}_i. \tag{2.65}$$

The new coordinates involve the relative coordinates $\mathbf{q}_{ij}$ and the corresponding conjugate momenta $\boldsymbol{\rho}_{ij}$:

$$\mathbf{q}_{ij} = \mathbf{r}_i - \mathbf{r}_j \tag{2.66}$$

$$\boldsymbol{\rho}_{ij} = \frac{1}{N} \left(\mathbf{p}_i - \mathbf{p}_j - \frac{m_i - m_j}{M} \langle \boldsymbol{\rho} \rangle \right), \tag{2.67}$$

where $\langle \boldsymbol{\rho} \rangle = \sum_{i=1}^{N} \mathbf{p}_i$, $M = \sum_{i=1}^{N} m_i$. Inversely, we obtain

$$\mathbf{r}_i = \frac{1}{M} \sum_{j=i+1}^{N} m_j \mathbf{q}_{ij} - \frac{1}{M} \sum_{j=1}^{i-1} m_j \mathbf{q}_{ji} + \langle \mathbf{q} \rangle \tag{2.68}$$

$$\mathbf{p}_i = \sum_{j=i+1}^{N} \boldsymbol{\rho}_{ij} - \sum_{j=1}^{i-1} \boldsymbol{\rho}_{ji} + \frac{m_i}{M} \langle \boldsymbol{\rho} \rangle, \tag{2.69}$$

where $\langle \mathbf{q} \rangle = \frac{1}{M} \sum_{i=1}^{N} m_i \mathbf{r}_i$. The fictitious particle corresponding to each ij pair of particles is defined with the new index k

$$k(i,j) = (i-1)N - \frac{i(i+1)}{2} + j \qquad (i < j). \tag{2.70}$$

So the total number of fictitious particles are $K = \frac{N(N-1)}{2}$. With this notation, equations (2.68) and (2.69) take the form

$$\mathbf{r}_i = \sum_{k=1}^{K} a_{ik} \frac{m_j}{M} \mathbf{q}_k + \langle \mathbf{q} \rangle \tag{2.71}$$

and

$$\mathbf{p}_i = \sum_{k=1}^{K} a_{ik} \boldsymbol{\rho}_k + \frac{m_i}{M} \langle \boldsymbol{\rho} \rangle \tag{2.72}$$

with $a_{im} = 1$ and $a_{jm} = -1$ when $m = k(i,j)$, otherwise, $a_{ij} = 0$. So the Hamiltonian in new coordinates is expressed as

$$H = \sum_{k,k'=1}^{K} T_{kk'} \boldsymbol{\rho}_k \boldsymbol{\rho}_{k'} + \frac{1}{2M} \langle \boldsymbol{\rho} \rangle^2 + \sum_{k=1}^{K} \frac{U_k}{\mathbf{q}_k} - \left(\sum_{k=1}^{K} L_k \mathbf{q}_k + \sum_{i=1}^{N} Q_i \langle \mathbf{q} \rangle \right) \cdot \mathbf{E}(t) \tag{2.73}$$

with

$$T_{kk'} = \sum_{i=1}^{N} \frac{a_{ik} a_{ik'}}{2m_i}, \quad U_k = Q_i Q_j \tag{2.74}$$

and

$$L_k = \frac{Q_i m_j - Q_j m_i}{M}. \tag{2.75}$$

So the equations of motion in regularised coordinates are given by

$$\frac{d\mathbf{q}_k}{dt} = 2 \sum_{k'=1}^{K} T_{kk'} \boldsymbol{\rho}_{k'}, \quad \frac{d\langle \mathbf{q} \rangle}{dt} = \frac{1}{M} \langle \boldsymbol{\rho} \rangle, \tag{2.76}$$

and

$$\frac{d\boldsymbol{\rho}_k}{dt} = \frac{U_k \mathbf{q}_k}{q_k^3} + L_k \mathbf{E}(t), \quad \frac{d\langle\boldsymbol{\rho}\rangle}{dt} = \sum_{i=1}^{N} Q_i \mathbf{E}(t). \tag{2.77}$$

2.2.2 Electron tunnelling during time propagation

In our propagation method, we also allow for each electron to tunnel. This is essential for our 3D semi-classical model to accurately describe the enhanced ionisation process [46–50], see section 1.2.2. To allow for tunnelling, we use the Wentzel-Kramers-Brillouin (WKB) approximation [93] with the transmission probability given by

$$T_{tun} \approx \exp\left(-2\int_{r_a}^{r_b} \sqrt{2(V_{tun}(r,t_{tun}) - E_{tun})}dr\right). \tag{2.78}$$

$V_{tun}(r,t_{tun})$ is the potential along the field direction of each electron. E_{tun} is the energy of the electron at the time of tunnelling t_{tun}. r_a and r_b are the tunnelling points and exit point, respectively.

Chapter 3

Non-sequential double ionisation of atoms in near-single cycle pulses

Non-sequential double ionisation in intense near-infrared laser fields is a fundamental process with electron-electron correlation playing a key role [16, 94, 95]. Considerable information regarding NSDI has been obtained from kinematically complete experiments, i.e., the momenta of the escaping electrons and ions are measured in coincidence [96]. Most of these experiments employ multi-cycle laser pulses allowing for multiple recollisions to occur before both electrons ionise. Multiple recollisions complicate the electron dynamics and render the comparison with theory difficult. Recently, however, kinematically complete experiments succeeded in confining NSDI to a single laser cycle by using carrier-envelope phase-controlled few- and near-single-cycle pulses [36, 37]. These experiments with near-single-cycle pulses allow for an easier comparison between theory and experiment. In this Chapter, we compare our 3D semi-classical model [42] for strongly-driven atoms with experimental results for near-single-cycle pulses [97].

3.1 Background on NSDI in atoms driven by near-single cycle pulses

To interpret the double ionisation spectra of driven *Ar* measured using near-single-cycle laser pulses, a simple one-dimensional (1D) classical model was put forth [37, 97, 98]. This model relies on the assumption that the dominant pathways of double ionisation are, for small and intermediate intensities, delayed non-sequential ionisation and, for higher intensities, sequential ionisation. For strongly-driven *Ar*, intermediate intensities refer to the intensity range from 2×10^{14} W/cm^2 to 4×10^{14} W/cm^2. This model neglects the contribution of another major pathway of double ionisation, namely, direct ionisation as well as the Coulomb potential. This 1D model did not achieve a quantitative agreement with the complete set of available experimental data over the whole intensity range. Delayed ionisation—also referred to as recollision-induced excitation with subsequent field ionisation, RESI [33, 34], and direct ionisation are two main pathways of NSDI. An interesting finding of these near-single cycle experiments was that the correlated momenta components of the two escaping electrons along the direction of the laser field have a cross-shaped pattern for an intensity around 10^{14} W/cm^2 [37, 97, 98]. A cross-shaped correlated electron momenta pattern due to the delayed double ionisation mechanism was previously identified in the context of strongly-driven *He* at an intensity of 9×10^{14} W/cm^2 and for a wavelength of 400 nm [99]. In a cross-shaped correlated electron momenta pattern the double ionisation probability is the highest when the component of the momentum along the direction of the laser field is very small for one electron while it takes a wide range of values for the other electron, see the experimental correlated electron momenta at 10^{14} W/cm^2 in Fig.3.5. In the context of strongly-driven *Ar*, the above described 1D model attributed the cross-shaped pattern of the correlated electron momenta to the delayed pathway of double ionisation [97, 98]. A quantum mechanical calculation, which neglects the Coulomb potential, was used to refine the contribution of the delayed pathway of

double ionisation to the cross-shaped correlated electron momenta pattern [100]. This calculation identified the key role that the symmetry of the excited state plays in the final shape of the correlated momenta.

3.2 Advantage of our 3D semi-classical model over previous models

Using our 3D semi-classical model [42], NSDI of *Ar* is studied when *Ar* is driven by 750 nm near-single-cycle laser pulses at intensities ranging from 0.85×10^{14} W/cm^2 to 5×10^{14} W/cm^2. All Coulomb forces and the interaction of each electron with the laser field are fully accounted for. Moreover, when analysing the numerically obtained doubly-ionised events, no assumptions are made regarding the prevailing mechanism of double ionisation and we use no free parameter. This is not the case for the 1D model [97]. In addition, the Coulomb singularity is fully accounted for using regularised coordinates [101]. This is an advantage over models which soften the Coulomb potential [102]. Previous successes of this 3D model include identifying the mechanism responsible for the fingerlike structure in the correlated electron momenta [42], which was predicted theoretically [38] and was observed experimentally for *He* driven by 800 nm laser fields [103, 104]. Moreover, this model was used to investigate direct versus delayed pathways of NSDI for *He* driven by a 400 nm laser field while achieving excellent agreement with fully ab-initio quantum mechanical calculations [35]. Using this model, in what follows, several observables are computed for different intensities of strongly-driven *Ar*. These observables are the sum of the two electron momentum components along the direction of the polarisation of the laser field and the double differential probability of the two electron momentum components along the polarisation direction of the laser field, i.e. the correlated electron momenta. Furthermore, the amplitude and the phase of the asymmetry parameter that determines the difference of the ions escaping with positive versus negative momentum along the polarisation direction of the laser field are computed as a function of the carrier-envelope phase and the

intensity.

Previously obtained experimental results over the whole intensity range [37, 97, 98] are in better agreement with the computed results obtained using the 3D semi-classical model rather than with the computed results obtained with the 1D model in Ref. [97]. Throughout this chapter the computed results are compared with the experimental results that were recently published in and adopted from Ref. [97] where the data acquisition and analysis is described in detail. Briefly, CEP stable laser pulses with a full-width-half-maximum pulse duration of 4 fs and a centre wavelength of 750 nm are focused onto a cold-gas jet of argon atoms inside a reaction microscope. There, the momenta of ions and electrons generated in the laser focus via strong field ionisation are recorded in coincidence as a function of the intensity and of the CEP of the laser pulse. The CEP is measured with a precision of roughly 200 mrad. Motivated by the good agreement we find between theory and experiment, the strength of the 3D semi-classical model in fully accounting for the electron dynamics is utilised to identify the prevailing pathway of double ionisation as a function of intensity. In addition, for a small intensity around 10^{14} W/cm^2, the dependence of the double ionisation pathways on CEP is computed using the 3D semi-classical model. Finally, the transition from strong to soft recollisions is identified as the main reason for the experimentally observed escape of the two electrons with opposite momenta at higher intensities [88].

3.3   3D semi-classical model for atoms and measurable quantities

The 3D semi-classical model employed is formulated in the framework of the dipole approximation (see Appendix A) [42]. The initial state in the 3D model entails one electron tunnelling through the field-lowered Coulomb potential with the ADK formula [70]. To obtain the tunnel ionisation rate for *Ar*, in the ADK formula the first ionisation energy of *Ar*, i.e. $I_{p_1} = 0.579$ a.u. and the effective

charge $Z = 1$ are used. The exit point of the tunnel-ionised electron is along the direction of the laser field and is computed using parabolic coordinates [105]. The remaining electron is initially described by a micro-canonical distribution [64]. In what follows, the initially tunnelling and bound electrons are denoted as electrons 1 and 2, respectively. The weight of each classical trajectory i that we propagate in time is given by

$$W_i = W_i^1 \cdot W_i^2, \tag{3.1}$$

where

$$W_i^1 \propto \left(\frac{1}{|\mathbf{E}(t_0)|} \right)^{2n^*-1} \exp\left(-\frac{2\kappa^3}{3|\mathbf{E}(t_0)|} \right) \tag{3.2}$$

is the ADK ionisation rate [70] at the time t_0 of tunnel-ionisation, see section 2.1.2.1.1. n^* is the effective principal quantum number given by $I_{p_1} = Z^2/2n^{*2}$. W_i^2 is the weight for electron 1 to have a transverse velocity equal to $v_\perp$ at the time t_0, see section 2.1.3:

$$W_i^2 \propto \frac{v_\perp}{|\mathbf{E}(t_0)|} \exp\left(-\frac{v_\perp^2 \kappa}{|\mathbf{E}(t_0)|} \right). \tag{3.3}$$

t_0 is the time electron 1 tunnel-ionises through the field-lowered Coulomb potential. The laser field is linearly polarised and is given by

$$\mathbf{E}(t) = E_0 e^{\left(-2ln2 \left(\frac{t}{t_{FWHM}} \right)^2 \right)} cos(\omega t + \phi)\hat{z}, \tag{3.4}$$

where $\tau = 4$ fs is the full-width-half-maximum pulse duration, ω=0.061 a.u (750 nm) is the frequency, E_0 is the strength and ϕ is the CEP of the laser field. The tunnel-ionisation time is selected as a uniform random number in the interval (-$2\tau,2\tau$) where the laser field in Eq.3.4 is switched on. The time propagation is determined by the three-body Hamiltonian of the two electrons with the nucleus kept fixed. During the time propagation we fully account for the Coulomb singu-

larity [42]. In addition, we assume that each electron is interacting with the nucleus with charge $Z = 2$. The double and single ionisation probabilities are given by

$$P_{DI} = \frac{\sum_i^{N_{DI}} W_i}{\sum_i^N W_i} \tag{3.5}$$

$$P_{SI} = \frac{\sum_i^{N_{SI}} W_i}{\sum_i^N W_i} \tag{3.6}$$

where N_{DI}, N_{SI} and N are the numbers of doubly-ionised, singly-ionised and all events, respectively.

3.4 NSDI and ionisation pathways

For the results presented in what follows, the intensities considered range from 0.85×10^{14} W/cm^2 to 5×10^{14} W/cm^2. At 0.85×10^{14} W/cm^2, 12 CEPs are considered ranging from $\phi = 15°$ to $\phi = 345°$ in steps of 30°. For all other intensities, 24 CEPs are considered ranging from $\phi = 0°$ to $\phi = 360°$ in steps of 15°. For each ϕ, at 10^{14} W/cm^2, 1.4×10^{14} W/cm^2, 2×10^{14} W/cm^2, 3×10^{14} W/cm^2, 4×10^{14} W/cm^2 and 5×10^{14} W/cm^2 the doubly-ionised events obtained are 1.5×10^4, 5×10^4, 10^5, 1.8×10^5, 3×10^5 and 6×10^5, respectively. For the results presented regarding total double ionisation the average has been taken over all CEPs for each intensity. From the above, it is clear that the computations required, particularly for the lower intensities, are challenging, since, it is time-consuming to obtain enough doubly-ionised events that render the statistical error very small for each intensity and for each of the 12 or 24 CEPs. The intense computations required is the reason results are obtained for seven intensities in the range from 0.85×10^{14} W/cm^2 to 5×10^{14} W/cm^2. Using the results obtained at these seven intensities an average over the focal volume is performed [106] to directly compare with experiment. It is, however, noted that computations at a larger number of intensities are needed to account more accurately for the focal volume effect, see Appendix C for details. For the results presented, it is stated explicitly when focal volume averaging is included and when it is not.

In Fig.3.1, the ratio of double to single ionisation probability is computed as a function of the laser intensity and compared to the experimental results [97]. It is found that the computed ratio of double to single ionisation probability reproduces well the overall pattern of the observed ratio. The computed ratio is found to be at most a factor of two smaller than the observed ratio and by a factor of 3.5 when the focal volume effect is accounted for. This difference possibly suggests that the effective charge of $Z = 2$ used to model the attractive Coulomb potential in the 3D semi-classical model during time propagation overestimates the Coulomb attraction.
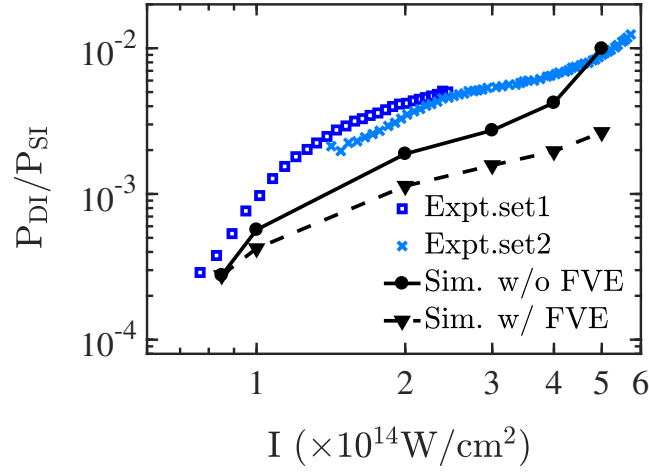
Figure 3.1: Ratio of double to single ionisation probability as a function of intensity. Experimental results [97] are denoted by dark blue squares and light blue crosses and computed results are presented by a solid line with black circles when the focal volume effect is not accounted for and by a dashed-line with triangles when the focal volume effect is accounted for. The difference in the two experimental sets results from slightly different averaging over the focal volume [97].

Once the doubly-ionised events are obtained using the 3D semi-classical model, an analysis of the classical trajectories is performed in time in order to identify the contribution of the direct and the delayed pathway of NSDI as a function of the laser intensity. The main two double ionisation energy transfer pathways are identified by using the time difference between the recollision time t_{rec} and the ionisation time (see Appendix D) of each electron t_{ion}^i, with $i = 1, 2$, for each doubly-ionised classical trajectory. The recollision time is defined as the time of minimum approach of the two electrons and is identified by the max-

imum in the electron pair potential energy. The ionisation time (see Appendix D) for each electron is defined as the time when the sum of the electron's kinetic energy (using the canonical momentum) and the potential energy due to the electron's interaction with the nucleus becomes positive and remains positive thereafter. The canonical momentum of an electron is given by $\mathbf{p} - \mathbf{A}$, with $\mathbf{A}$ the vector potential. The ionisation time of electron 1 is, thus, not necessarily the time t_0 this electron tunnel-ionises at the start of the time propagation. This energy is referred to as compensated energy and was introduced in Ref. [107], see Appendix D for details. A doubly-ionised trajectory is labeled as delayed or direct depending on the time differences $t_{ion}^1 - t_{rec}$ and $t_{ion}^2 - t_{rec}$. Specifically,

$$|t_{ion}^1 - t_{rec}| < t_{diff} \,\&\, t_{ion}^2 < t_{ion}^1 \qquad (3.7a)$$
$$|t_{ion}^2 - t_{rec}| < t_{diff} \,\&\, t_{ion}^1 < t_{ion}^2 \qquad (3.7b)$$
$$\text{Direct}$$

$$t_{ion}^1 - t_{rec} > t_{diff} \,\&\, t_{ion}^2 - t_{rec} < t_{diff} \qquad (3.8a)$$
$$t_{ion}^2 - t_{rec} > t_{diff} \,\&\, t_{ion}^1 - t_{rec} < t_{diff} \qquad (3.8b)$$
$$\text{Delayed}$$

$$t_{ion}^1 - t_{rec} > t_{diff} \,\&\, t_{ion}^2 - t_{rec} > t_{diff} \qquad (3.9) \quad \text{Double Delayed}$$

where t_{diff} is a positive arbitrary parameter. The percentage of doubly-ionised events labeled as delayed or direct, out of all doubly-ionised events, depends on our choice of the time difference t_{diff}. These percentages are given by

$$R_{DI}^{\alpha} = \frac{\sum_i^{N_{DI}^{\alpha}} W_i}{\sum_i^{N_{DI}} W_i}, \qquad (3.10)$$

where N_{DI}^{α} is the number of α labelled doubly-ionised events, with α denoting the direct or delayed events. Thus, the probability of doubly-ionised events labeled as delayed or direct, out of all events, is given by

$$P_{DI}^{\alpha} = R_{DI}^{\alpha} P_{DI}. \qquad (3.11)$$

t_{diff} should not be chosen neither very large, such as 1/4 T, or very small such as 1/40 T. Choices in between are reasonable and lead to similar trends of the two prevailing pathways of double ionisation. This is shown in Fig.3.2 where the percentages of direct and delayed doubly-ionised events are plotted for t_{diff} equal to 1/10 T, 1/20 T and 1/40 T as a function of the intensity of the laser field. It is found that the contribution of the direct and the delayed pathways to double ionisation as a function of intensity displays general trends that do not significantly depend on the choice of t_{diff}. Both the direct and the delayed pathways of double ionisation significantly contribute at all intensities. Thus, the direct pathway can not be neglected as was done in previous models. The direct pathway contributes the most for intermediate intensities. In Fig.3.2, at a high intensity above 4×10^{14} W/cm^2, it is shown that the contribution of the direct pathway of double ionisation starts decreasing. At this high intensity a transition from strong to soft recollisions takes place, as discussed in the following. It is found that double delayed events contribute no more than 15% for the smallest intensity even when the time difference is chosen small and equal to 1/40 T. $t_{diff} = 1/10$ T is chosen for the results presented in this work. We find that with this choice of t_{diff} the distributions of the sum of the two electron momentum components along the polarisation direction of the laser field for the direct and the delayed pathways of double ionisation are the closest to what is expected from Ref.[34]. That is, the former distribution dips while the latter one peaks around zero.

We find that different results are obtained if instead of the compensated energy the energy of each electron is used to identify the ionisation time. Namely, one finds that at an intensity of 0.85×10^{14} W/cm^2 almost all classical trajectories are identified as double delayed. This was the conclusion in Ref. [36]. Using the actual energy to identify the ionisation time at an intensity of 3×10^{14} W/cm^2 results in the direct pathway of double ionisation still only contributing 20%. However, this is not a reasonable result. At 3×10^{14} W/cm^2 3.17 U$_p$ is equal to 50 eV which is much higher than the second ionisation energy of *Ar*. Moreover, the recollision at this intensity is strong, which is discussed in the section for the correlated electron
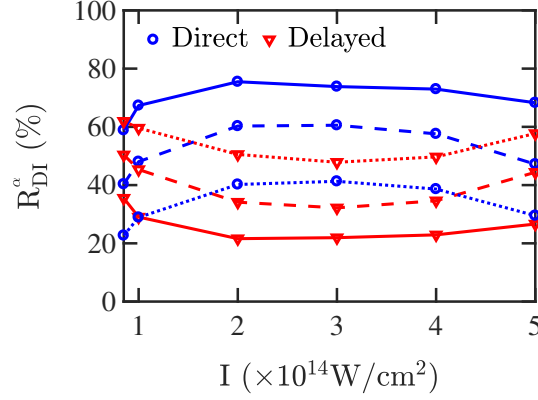
Figure 3.2: Percentages of the direct (blue circles) and the delayed (red triangles) pathways of DI as a function of laser field intensity for $t_{diff} = 1/10$ T (solid lines), $t_{diff} = 1/20$ T (dashed lines) and $t_{diff} = 1/40$ T (dotted lines). The FVE is not accounted for.

momenta as a function of intensity, and so the direct pathway of double ionisation should contribute significantly. Thus, the compensated energy is employed to identify the ionisation time in this work which leads to both the direct and delayed pathway being the main pathways of double ionisation in agreement with Ref. [102] for the smallest intensity.

3.5 Distribution of the sum of the two electron momenta

In Fig.3.3, the probability distributions of the sum of the two electron momentum components along the polarisation direction of the laser field are presented for intensities from 0.85×10^{14} W/cm^2 to 5×10^{14}W/cm^2. In Fig.3.3, the contribution of the direct and the delayed pathways of double ionisation to the probability distribution of the sum of the momenta is also shown; the focal volume effect is not accounted for. It is found that the distribution of the delayed pathway is concentrated around zero while of the direct pathway is a doubly-peaked distribution, as expected from Ref.[34]. The direct pathway's probability distribution of the sum of the momenta is the broadest one. Therefore, including only the delayed pathway of double ionisation would result in a narrower distribution of the sum of the momenta
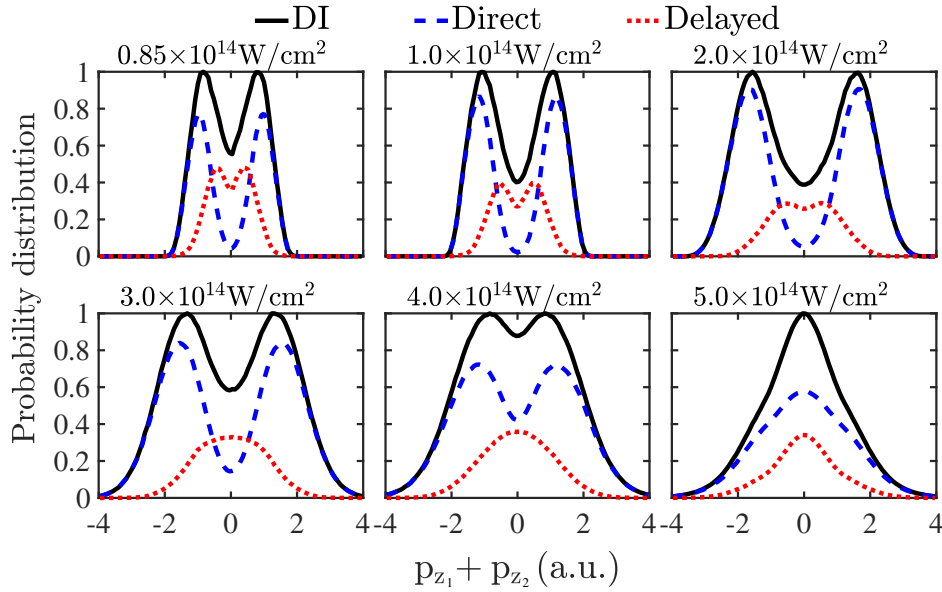
Figure 3.3: Probability distribution of the sum of the two electron momentum components parallel to the polarisation of the laser field (black solid lines) for laser field intensities from 0.85×10^{14} W/cm^2 to 5×10^{14} W/cm^2. For each intensity, the probability distribution of the sum of the momenta of the delayed pathway (red dotted lines) and of the direct pathway (blue dashed lines) are also plotted. The FVE is not accounted for. Each probability distribution is divided by its maximum value.

than the observed one. Indeed, the 1D model described in Ref.[97] which accounts only for the delayed pathway of double ionisation results in a narrower probability distribution of the sum of the momenta than the observed one.

In Fig.3.4, the experimental results for the probability distribution of the sum of the momenta in Ref.[97] are compared with one set of computed results that account for the focal volume effect (black dashed lines) and one that does not (black solid lines). It is found that the computed results are in good agreement with the observed ones. Specifically, it is found that, for each intensity, the computed sum of the electron momenta extends over a range that is very similar to the experimental one. For instance, for an intensity of 0.85×10^{14} W/cm^2, the computed sum of the momenta extends over a range from roughly -2 a.u. to 2 a.u., while, for an intensity of 5×10^{14} W/cm^2, it extends from -4 a.u. to 4 a.u.; for both intensities these ranges are in agreement with the experimental results [97]. It is noted that a difference of the computed probability distributions of the sum of the electron momenta with the
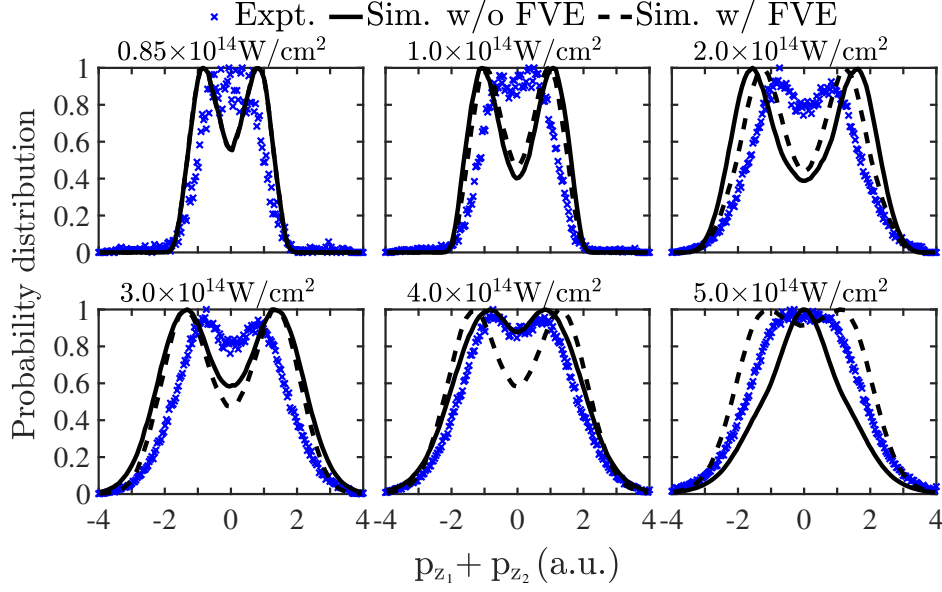
Figure 3.4: Probability distribution of the sum of the two electron momentum components parallel to the polarisation of the laser field for laser field intensities from 0.85×10^{14} W/cm^2 to 5×10^{14}W/cm^2. The computed results with the FVE not accounted for are denoted by black solid lines and when it is accounted for by black dashed lines; the blue crosses denote the experimental results [97]. Each probability distribution is divided by its maximum value.

experimental ones is that the computed ones have smaller values around zero. This is more so the case for the computed results that account for the focal volume effect. This difference suggests that the current 3D model underestimates the contribution of the delayed pathway of double ionisation.

3.6 Transition from strong to soft recollisions in correlated electron momenta

For intensities ranging from 0.85×10^{14} W/cm^2 to 5×10^{14}W/cm^2, the computed correlated electron momenta, i.e. the double differential probability of the two electron momentum components along the polarisation direction of the laser field, with the focal volume effect accounted for are plotted and compared to the measured ones in Fig.3.5. We find that at all intensities, but particularly at smaller ones, there are fewer doubly-ionised events with both momenta being close to zero than in the
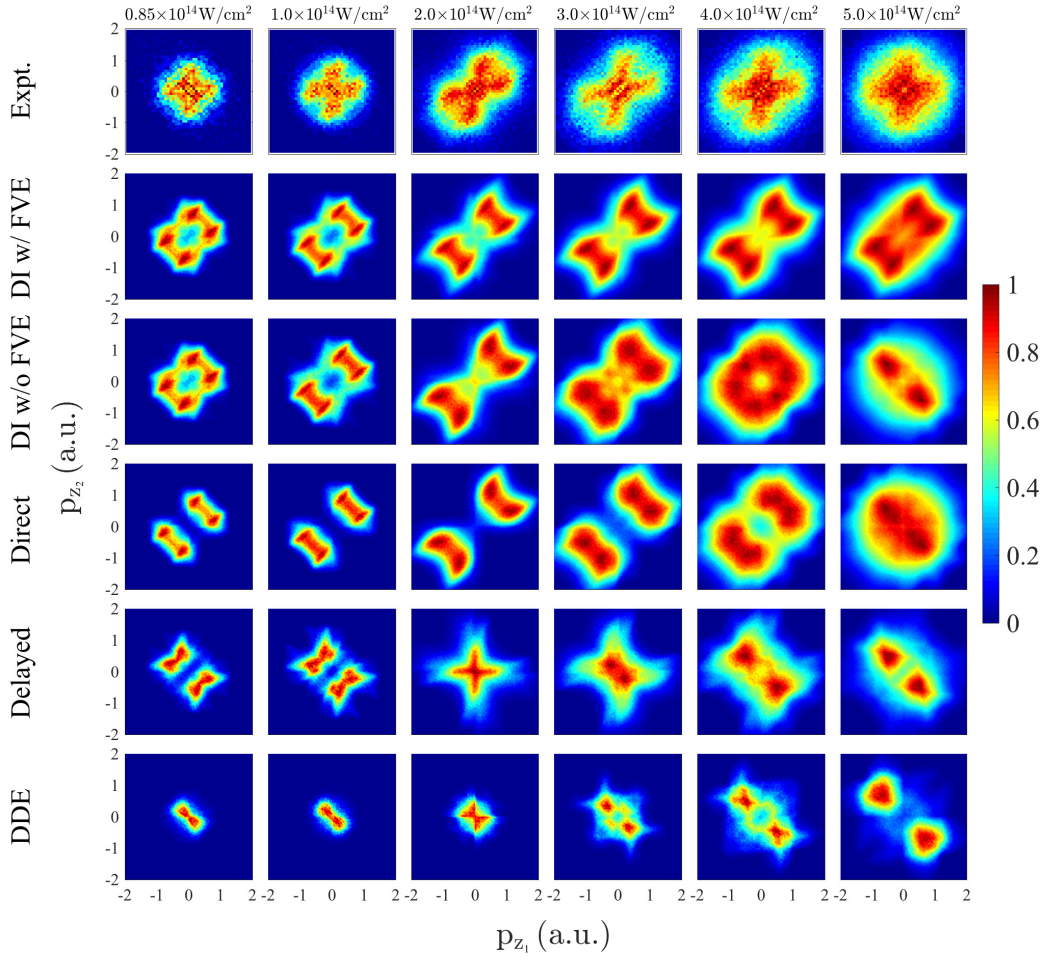
Figure 3.5: First row: measured correlated electron momenta [97]. Second row: computed correlated electron momenta for all double ionisation events with the FVE accounted for. Third row: computed correlated electron momenta for all double ionisation events with the FVE not accounted for. Fourth row: correlated electron momenta for the direct pathway of double ionisation with the FVE not accounted for. Fifth row: correlated electron momenta for the delayed pathway of double ionisation with the FVE not accounted for. Sixth row: correlated electron momenta for the double delayed pathway of double ionisation with the FVE not accounted for. The sum of the fourth row plus the fifth row plus the sixth row is equal to the third row. Each double differential distribution is divided by its maximum value.

experimentally obtained correlated electron momenta [37, 97]. In Fig.3.5, we also plot the computed correlated electron momenta for all doubly-ionised events and for the direct and the delayed double ionisation pathways without accounting for the focal volume effect. Each double differential distribution is divided by its maximum value. At intermediate intensities of $2\text{-}4 \times 10^{14}$ W/cm^2, as in the observed correlated
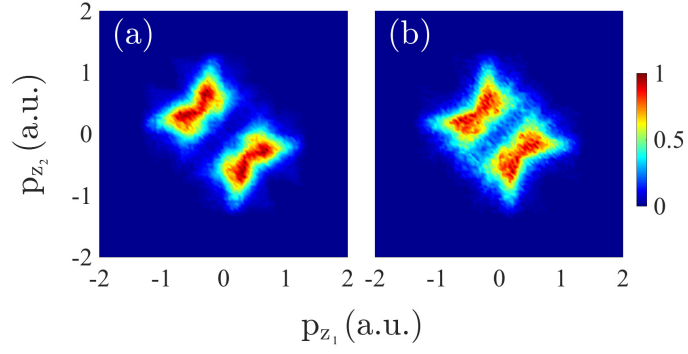
Figure 3.6: Correlated electron momenta at an intensity 0.85×10^{14} W/cm^2 for the delayed pathway of double ionisation for the case when the electron that ionises second is electron 2 (a) and electron 1 (b). Each double differential distribution is divided by its maximum value.

electron momenta in Ref.[97], the computed correlated electron momenta transition to a well-known pattern [32, 34]. This pattern involves both electrons escaping in the same direction either parallel or antiparallel to the laser field, thus, giving rise to a much higher probability density in the first and third quadrants of the correlated electron momenta, rather than the second and fourth ones. We find that this pattern is due to the direct pathway of double ionisation which is the prevailing one at intermediate intensities of 2-4$\times 10^{14}$ W/cm^2. This pattern is due to strong recollisions where the two electron momentum components along the direction of the laser field are both determined from the vector potential at times just larger than the recollision time. Thus, both electrons escape with similar momenta in the direction along the polarisation of the laser field. We also find that at these intermediate intensities the pattern of the correlated electron momenta for the delayed pathway of double ionisation is more spread out over all four quadrants and has a significant number of doubly-ionised events with both electron momenta close to zero, as expected from Ref.[34].

At smaller intensities of 0.85×10^{14} W/cm^2 and 10^{14} W/cm^2, the computed correlated electron momenta resemble but do not quite have the cross-shaped pattern of the measured results [37, 97], see Fig.3.5. The main difference is that the computed correlated electron momenta have fewer doubly-ionised events with both electron momenta being close to zero. At these small intensities, we find that the direct path-

way of double ionisation involves mainly events with both electrons escaping in the same direction either parallel or antiparallel to the laser field, however, the electron momenta are not as equal as at intermediate intensities. At small intensities, we also find that the delayed pathway involves mainly doubly-ionised events with both electrons escaping in the opposite direction, with magnitudes of the electron momenta that are more asymmetric than for the direct pathway of double ionisation. The cross-shaped pattern is better reproduced by the delayed double ionisation pathway, see Fig.3.5. Indeed, this pathway does not have as many doubly-ionised events with equal magnitude of the components of the electron momenta along the direction of the laser field as the direct pathway does. In addition, we find that 63% of the events labelled as delayed doubly-ionised satisfy the conditions in Eq.3.8 (b) while 37% satisfy the conditions in Eq.3.8 (a). That is, for the majority of delayed doubly-ionised events the initially bound electron is the one that ionises last following recollision. We find that the correlated electron momenta when the tunnelling electron ionises second in the delayed doubly-ionised events (37%) resemble more a cross-shaped pattern than the correlated electron momenta when the initially bound electron ionises second (63%), see Fig.3.6.

A less known pattern is that observed experimentally and retrieved computationally with the 3D semi-classical model for intensities above 4×10^{14} W/cm^2, see Fig.3.5. For these higher intensities, it is found that the two electrons escape mostly with opposite momenta for a significant number of doubly-ionised events. To identify the reason for this shift in the correlated electron momenta, in Fig.3.7 , the time electron 1 tunnel-ionises, t_0, and the recollision time, t_{rec}, are plotted for three different intensities, namely, 10^{14} W/cm^2, 3×10^{14} W/cm^2 and 5×10^{14} W/cm^2 and for two different CEP's, namely, $\phi = 15°$ and $\phi = 105°$ for each intensity. The tunnelling time of electron 1 is found to be close to the times corresponding to the extrema of the laser field for all three intensities. However, the distribution of the recollision time is found to shift from times corresponding roughly to zeros of the laser field for an intensity of 10^{14} W/cm^2 to times corresponding to the extrema of the laser field for an intensity of 5×10^{14} W/cm^2. The transfer of energy
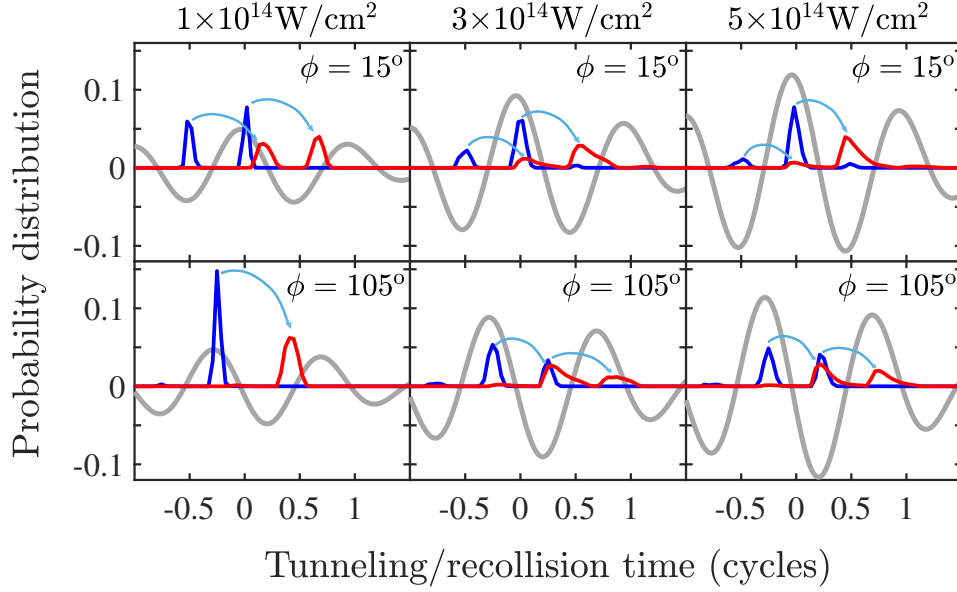
Figure 3.7: Probability distribution of the tunnelling time t_0 of electron 1 (blue line) and of the recollision time t_{rec} (red line) for intensities 10^{14} W/cm^2, 3×10^{14} W/cm^2 and 5×10^{14} W/cm^2 and for two different CEPs, $\phi = 15°$ and $\phi = 105°$, for each intensity. Similar results hold for all other CEPs. Grey line denotes the laser field. The light blue arrows indicate the mapping of a tunnelling-time peak to a recollision-time peak.

from electron 1 to electron 2 is much smaller for the soft recollisions. For these higher intensities, where soft recollisions prevail, the momentum of electron 1 is mostly determined from the vector potential at the tunnelling time. The momentum of electron 2 is determined by the vector potential shortly after recollision takes place which is roughly half a laser cycle after electron 1 tunnel-ionises. As a result, the two electrons escape mostly with opposite momenta. This mechanism of soft recollisions for higher intensities was first identified in a theoretical study of strongly-driven N$_2$ with fixed nuclei [88]. For the delayed pathway of double ionisation, this opposite momenta pattern, demonstrated with much higher probability density in the second and fourth quadrants of the correlated electron momenta, sets in at lower intensities of 3×10^{14} W/cm^2, see Fig.3.5. For the direct pathway this opposite momenta pattern sets in at higher intensities of 5×10^{14} W/cm^2. This is consistent with a smaller transfer of energy taking place from electron 1 to electron 2 at the recollision time in the delayed pathway compared to the energy transfer in the direct pathway.

3.7 Asymmetry parameter

The asymmetry parameter [97]

$$A(I,\phi) = \frac{R_{DI}^+(I,\phi) - R_{DI}^-(I,\phi)}{R_{DI}^+(I,\phi) + R_{DI}^-(I,\phi)} \tag{3.12}$$

is computed as a function of the intensity I and the CEP (ϕ). $R_{DI}^+(I,\phi)$ and $R_{DI}^-(I,\phi)$ denote the percentage of doubly-ionised events with ions escaping with positive and negative momentum, respectively, along the direction of the polarisation of the laser field. Since in the 3D semi-classical model the nucleus is fixed, $R_{DI}^+(I,\phi)$ and $R_{DI}^-(I,\phi)$ correspond to the percentage of double ionisation events where the sum of the two electrons' momentum components along the direction of the laser field polarisation are negative and positive, respectively. For each intensity, $A(I,\phi)$ is fitted with the sinusoidal function

$$A(I,\phi) = A_0(I)\sin(\phi + \phi_0(I)), \tag{3.13}$$

In Fig.3.8, we illustrate at 3×10^{14}W/cm^2 how the sinusoidal function in Eq.3.13 fits our computed results for $A(I,\phi)$ with $A_0 = 0.42$ and $\phi_0 = 46°$. The computed results show that for a given intensity the percentage of doubly-ionised events with ions escaping with positive versus negative momentum changes as a function of the CEP.

In a manner similar to the one illustrated in Fig.3.8, we obtain the computed asymmetry amplitude $A_0(I)$ and offset phase $\phi_0(I)$ at other intensities. The computed $A_0(I)$ and offset phase $\phi_0(I)$ are plotted in Fig.3.9 (a) and (b), respectively, and compared with two sets of experimentally obtained asymmetry parameters [97]. The comparison shows that the 3D semi-classical model reproduces well the decreasing pattern of A_0 and the increasing pattern of ϕ_0 with increasing intensity. However, the computed values for these asymmetry parameters are higher than the ones obtained from the experimental results. Smaller values of A_0 correspond to a
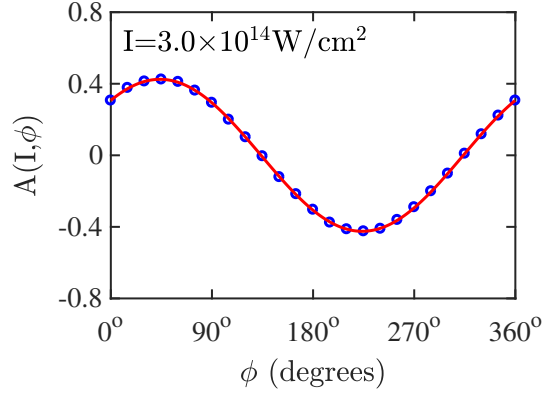
Figure 3.8: The simulation results (blue circles) of the asymmetry parameter $A(I,\phi)$ at I=3.0×10^{14} W/cm^2 as a function of ϕ. The sinusoidal function used to fit the computed results is denoted with a red solid line.
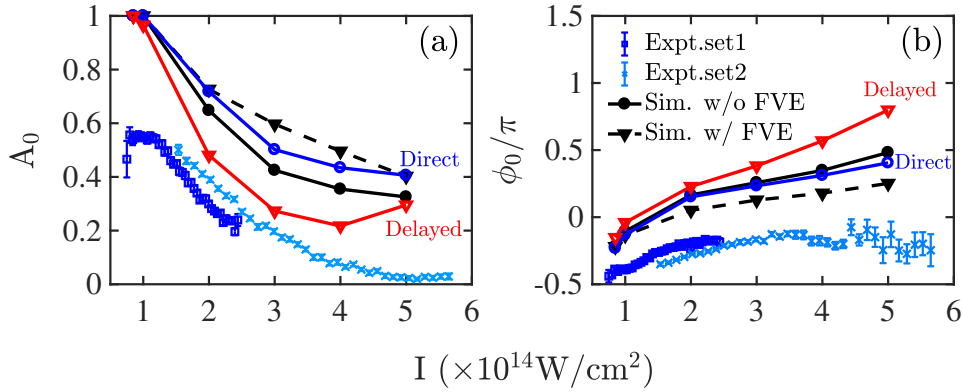
Figure 3.9: Asymmetry parameters A_0 (a) and offset phase ϕ_0 (b) as a function of intensity. The computed results for all doubly-ionised events when the focal volume effect is not accounted for are denoted by black solid lines with circles and when it is accounted for by black dashed lines with triangles. The delayed and direct pathways are denoted by red solid lines with triangles and blue solid lines with circles, respectively. For the direct and delayed pathways, the FVE is not accounted for. Experimental results[97] are denoted by light blue crosses and dark blue squares.

more spread out pattern of the correlated electron momenta. Thus, the larger values of A_0 of the computed results are consistent with the computed correlated electron momenta having less doubly-ionised events with sum electron momenta close to zero compared to the measured ones. Moreover, in Fig.3.9 (a) and (b) the asymmetry parameters are plotted for each of the main two pathways of NSDI. It is shown that for both pathways the asymmetry parameter $\phi_0(I)$ has a similar pattern. The asymmetry parameter $A_0(I)$ for the delayed pathway is generally smaller. This is consistent with the correlated electron momenta of the delayed pathway having a

more spread out pattern in all four quadrants than the correlated electron momenta of the direct double ionisation pathway, as we have seen in the previous section. Since $A_0(I)$ is smaller for the delayed pathway of double ionisation, the fact that the computed values of $A_0(I)$ are larger than the measured ones could be due to the fact that the 3D semi-classical model underestimates the contribution of the delayed pathway. We have reached a similar conclusion when discussing the distribution of the sum of the electron momenta.

3.8 Correlated momenta and double ionisation pathways as a function of CEP
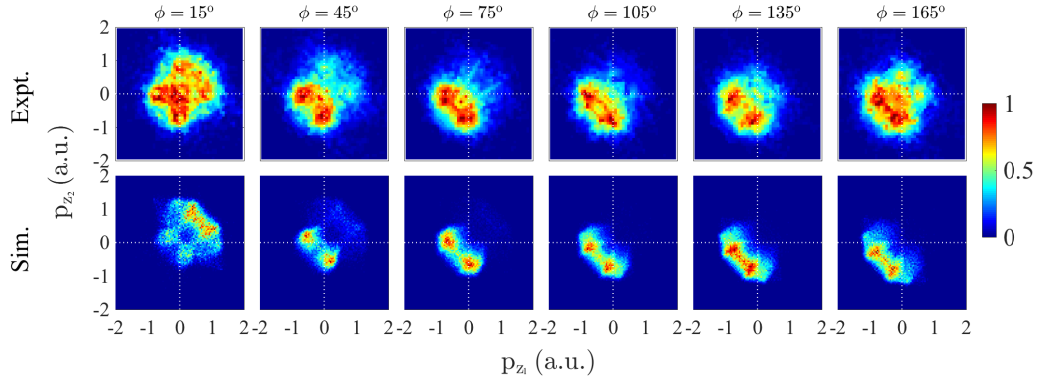
Figure 3.10: Correlated momenta at intensity 0.85×10^{14} W/cm^2 for ϕ ranging from 15° to 165° with a step of 30°. The relevant experimental results from Ref. [108] are shown for comparison. Each distribution is divided by its maximum value.

In what follows, the dependence of the correlated momenta on the CEP is investigated at an intensity of 0.85×10^{14} W/cm^2. In Fig.3.10, the correlated momenta are plotted for ϕ ranging from 15° to 165° with a step of 30°. The bin size of the CEP is chosen to be larger than 200 mrad, which is the experimental precision of the CEP, and large enough in order to get good statistics. For data analysis, all events are selected for which one electron has been detected in coincidence with an Ar^{2+} ion. The momentum of the second electron, which is not detected for most events, is calculated from conservation of momentum. Both the data and the computed results are symmetrised with respect to the bottom-left-to-top-right diagonal in order to ac-

Figure 3.11: Percentage contribution of the direct and the delayed pathways of DI as a function of the CEP at an intensity of 0.85×10^{14} W/cm^2.

count for the two electrons being indistinguishable. Moreover, due to the symmetry of the Hamiltonian, when $\phi \to \phi + 180°$ then $\mathbf{p} \to -\mathbf{p}$. This symmetry is respected by the computed results. In the experimental results, there is a small deviation from this symmetry. This deviation arises from artifacts of the electron spectrometer and false coincidences. For each CEP, in the top right half of the correlated electron momenta plot the impact of false coincidences is stronger than in the bottom left half. For CEP ranging from 195° to 345° the correlated electron momenta plots have more doubly-ionised events in the top right half. Thus, in Fig.3.10, we compare the computed results with the measured correlated electron momenta which are more accurate, i.e. for CEP ranging from 15° to 165° where the correlated electron momenta have more doubly-ionised events in the bottom left half.

A good agreement is found between the computed and the experimental results for CEP ranging from 15° to 165° given the experimental uncertainty of 200 mrad in the CEP. Specifically, the computed correlated momenta correctly reproduce the overall observed pattern for each individual CEP. A difference between the computed and the experimental results is that the former results have less doubly-ionised events with both electron momenta close to zero suggesting that the computations overestimate the contribution of the direct pathway. To better illustrate the change of the correlated momenta pattern as a function of the CEP plotted in Fig.3.10, in Fig.3.11 the percentage of the direct and delayed pathways of double ionisation are plotted as a function of the CEP. At an intensity of 0.85×10^{14} W/cm^2 the delayed

pathway has the largest contribution for CEPs $\phi = 45°$ and $\phi = 225°$, while it has the smallest for CEPs $\phi = 165°$ and $\phi = 345°$. In Fig.3.10, a comparison of the correlated momenta between $\phi = 45°$ and $\phi = 165°$ shows that there is a higher probability density for both electrons to ionise with the same large momentum, with both electrons escaping in the direction that is opposite to the electric field, for $\phi = 165°$ than for $\phi = 45°$. This is indeed consistent with the direct ionisation pathway having a larger contribution for $\phi = 165°$ than for $\phi = 45°$ as shown in Fig.3.11. From Fig.3.11, it is found that the contribution of each of the two main pathways of double ionisation varies roughly by 20% as a function of the CEP for the smallest intensity of 0.85×10^{14} W/cm^2.

3.9 Conclusions

Using a 3D semi-classical model we have investigated the dependence of double ionisation observables on the intensity and on the carrier-envelope phase of a near-single-cycle near-infrared laser field employed to drive *Ar*. The good agreement of the computed results with recent experiments employing near-single-cycle laser pulses [37, 97, 108], adds to previous successes of this 3D model in identifying features of non-sequential double ionisation of two-electron atoms when driven by many-cycle laser pulses [35, 42, 99]. We have found that a difference between the computed and the experimental results is a lower value of the distribution of the sum of the two electron momentum components along the direction of the polarisation of the laser field and of the correlated electron momenta around zero. This seems to suggest that the current 3D model overestimates the Coulomb attraction of each electron from the nucleus. Future studies can improve on the 3D model for many electron atoms such as *Ar* by using more accurate effective potentials for the time propagation. Moreover, we have demonstrated that the main pathways of double ionisation, that is, the direct and the delayed pathways, both significantly contribute at all intensities currently under consideration. Furthermore, we have investigated the prevalence of the direct versus the delayed pathway as a function of the CEP for an intensity of 0.85×10^{14} W/cm^2 and it was shown that the results obtained are consistent with features of the observed correlated electron momenta [108]. Finally, a previously-predicted in the context of a strongly-driven fixed-nuclei N$_2$ unexpected anti-correlation momentum pattern at higher intensities [88], is observed experimentally in the context of strongly-driven *Ar* [97] and also reproduced in the current work for strongly-driven *Ar* by a near-single-cycle laser field. We have shown that this anti-correlation pattern is due to soft recollisions with recollision times close to the extrema of the laser field.

Chapter 4

Two-electron triatomic molecules in intense laser fields

In this chapter, we explore frustrated double ionisation and double ionisation of strongly-driven D_3^+ and H_3^+ using the 3D semi-classical model presented in Chapter 2. So far, D_3^+ and H_3^+ are the only multi-centre molecules, where frustrated ionisation has been studied in benchmark experiments [55, 57, 59] and discussed using classical models [109, 110]. These latter classical models, however, do not allow for tunnelling during the propagation. Thus, the 3D semi-classical model we use offers a significant advantage over previous computations in describing frustrated ionisation in molecules. First, in section 4.1, we present results for frustrated double ionisation and double ionisation during the break-up of D_3^+ driven by intense laser fields. Comparing our results for FDI and DI with experimental results [59], we find a good agreement for the distribution of the kinetic energy release (KER). Then, in section 4.2, we present a detailed study of the properties of frustrated double ionisation and frustrated single ionisation (FSI) for the ground state of H_3^+ when driven by intense laser fields. These results for driven H_3^+ are compared with results for driven H_2.

4.1 Frustrated double ionisation of strongly-driven D_3^+

In this section, we investigate frustrated double ionisation of D_3^+ when driven by an intense, linearly polarised, near-infrared (800 nm) laser field. We show that our result for the distribution of the kinetic energy release for FDI is in good agreement with the experimental result in Ref. [59]. Moreover, even though FDI is generally associated with tunnel-ionisation, we show that for increasing field strengths the mechanism underlying FDI is over-the-barrier ionisation instead. We also show that for strongly-driven D_3^+ one of the two pathways contributing to FDI [111] has a trace in the angular distribution of the ion fragments and, very importantly, this trace can potentially be observed experimentally.

4.1.1 Method and initial molecular and field configuration

In our model we employ a linearly polarised laser field of the form

$$\mathbf{E}(t) = E_0(t)\cos(\omega t)\hat{z}$$

$$E_0(t) = \begin{cases} E_0 & 0 \leq t < 10T \\ E_0 \cos^2\frac{\omega(t-10T)}{8} & 10T \leq t \leq 12T, \end{cases} \tag{4.1}$$

with $E_0(t)$, T and ω the envelope, the period and the frequency, respectively, of the laser field. We take ω=0.05675 a.u. (800 nm). In the following, we consider only two cases of planar alignment, i.e. one side of the equilateral, molecular triangle is either parallel or perpendicular to the $\hat{z}$-axis. We create the initial condition in the region for $\phi_0 = \omega t_0$ in the interval $\in [-\pi/2, \pi/2]$, see Ref. [62]. An illustration of the field is shown in Fig.4.1.

To compare with the experimental results [55, 59] we take the initial state of
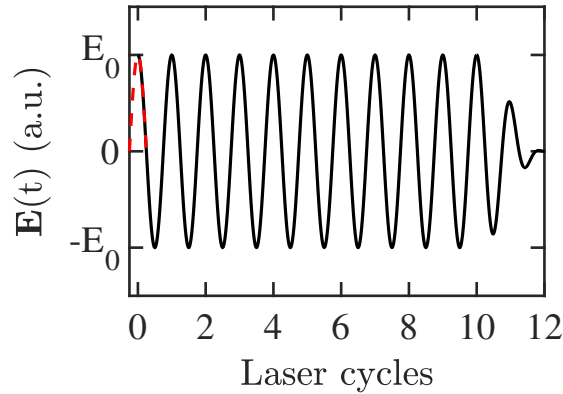
Figure 4.1: The laser field used in the simulation. It consists of 10 full laser cycles with 2 turn-off cycles. The red dashed lines indicates the initial sampling region.
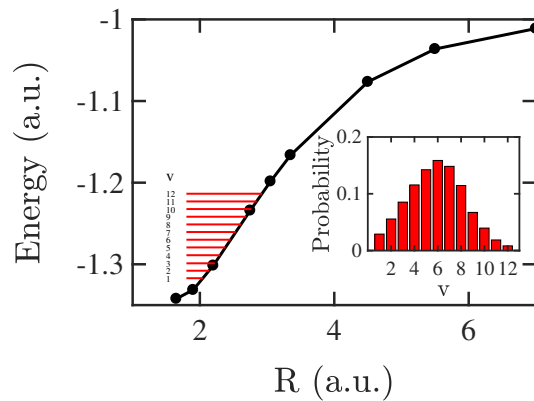
Figure 4.2: The symmetric stretch vibrational levels of D_3^+ and the relevant probabilities (inset panel), from Ref. [112]. The internuclear distances R are obtained by interpolating the potential energy curves from Ref. [113].

the D_3^+ molecule to be the one created via the reaction [55, 59]

$$D_2 + D_2^+ \rightarrow D_3^+ + D. \tag{4.2}$$

This initial state consists of a superposition of symmetric stretch vibrational states $v = 1 - 12$ [112, 113], each with a triangular configuration. Tunnel ionisation is very sensitive to variations of the ionisation potential and known to preferentially ionise larger internuclear separations [114, 115]. Thus, we assume that most of the D_3^+ ionisation occurs at the outer classical turning point of the vibrational levels. The turning point varies from 2.04 a.u. ($v = 1$) to 2.92 a.u.($v = 12$) [112, 113]. The probabilities of these vibrational levels are shown in Fig.4.2, taken from Ref. [112]. The internuclear distances are obtained by interpolating the potential energy curves

from Ref. [113]. We find the first and second ionisation potentials of the relevant 12 vibrational states using the quantum chemistry software Molpro [91]. For the initial state of D_3^+ in the laser field, we assume that one electron (electron 1) escapes either by tunnelling or over-the-barrier ionisation in the field-lowered Coulomb potential [62], depending on the field strength and the vibrational state. As mentioned in Chapter 2, we use a tunnelling rate given by the semi-classical formula in Ref.[73]. If electron 1 escapes by tunnelling then its transverse to the laser field velocity distribution is a Gaussian [25, 70], while its velocity parallel to the laser field is assumed to be zero, see section 2.1.3. We assume that the other electron is initially bound (electron 2). Its initial state is described by the micro-canonical distribution as described in section 2.1.4.2. Since an initial pre-dissociation does not significantly modify the ionisation dynamics [62], we simplify our model by initialising the nuclei at rest for all vibrational levels.

The propagation of our model system is performed as described in section 2.2. We allow for tunnelling of each electron during the propagation in time. This is essential in order for our model to accurately describe the enhanced ionisation process [47–51].

4.1.2 FDI and DI of strongly-driven D_3^+

We now consider DI and FDI of strongly-driven D_3^+. DI refers to the formation of three D^+ ions and two escaping electrons. FDI refers to the formation of a neutral excited fragment D^*, two D^+ ions and one escaping electron. Previous experiments on strong-field ionisation of D_3^+ measured, among other observables, the kinetic energy release, i.e., the sum of the kinetic energies of the ion fragments [59]. To be able to compare the experimental KER with the KER from our simulation we need to account for the intensity averaging in the focal volume [11, 116], see Appendix C for details.

We first compute the KER distribution for a process $\alpha =$FDI,DI as a function

of the intensity of the laser field as follows

$$P^\alpha(I, KER) = \frac{\sum\limits_{v, \phi_0} P_v P^\alpha(\phi_0, v, I, KER) \Gamma(\phi_0, v, I)}{\sum\limits_{v, \phi_0} P_v \Gamma(\phi_0, v, I)}, \tag{4.3}$$

where $P^\alpha(\phi_0, v, I, KER)$ is the probability to obtain a KER from a vibrational state v, for an initial phase of the laser field $\phi_0 = \omega t_0$, and for a laser field intensity I. $I = 1/2c\varepsilon_0 E_0^2$, where c is the speed of light and ε_0 is the vacuum permittivity, see Appendix B. The initial phase ϕ_0 corresponds to the starting point of the propagation. $\Gamma(\phi_0, v, I)$ is the tunnel-ionisation rate computed using the semi-classical formula in Ref. [73] and P_v is the percentage of the vibrational state v in the initial state produced following the reaction generating D_3^+ [112].

Following the formulation in [11, 116] we compute the KER distribution for a laser peak intensity I_{max} as follows

$$P^\alpha(I_{max}, KER) = \int_0^{I_{max}} \frac{P^\alpha(I, KER)}{I} dI. \tag{4.4}$$

In practice, in Eq.4.4 we integrate only over the intensities which significantly contribute to the process α. To find the lower limit of these intensities we compute the ionisation probability for an intensity I and a vibrational state v, which for small values of the ionisation probability is given by

$$\Gamma(v, I) = 1 - \exp\left(-\int_{t_i}^{t_f} \Gamma(\omega t, v, I) dt\right) \approx \int_{t_i}^{t_f} \Gamma(\omega t, v, I) dt \tag{4.5}$$

with the integration over the duration of the laser pulse. For the laser pulse and all the vibrational states of the triatomic molecule we currently consider, we find that the ionisation probability of D_3^+ is very small for field strengths less than 0.06 a.u. Therefore, only field strengths above 0.06 a.u. contribute to the observed KER distributions.

We now compare the computed intensity-averaged KER distributions with the measured ones [59] for a peak field strength of 0.56 a.u., which corresponds to the

experiment's intensity of 1.1×10^{16} W/cm^2 [59]. We find that the KER distributions for FDI for both currently considered alignments of the molecule relative to the laser field direction of polarisation are very similar; the same holds for the KER distributions of DI. We therefore expect that any other planar alignment of molecule and laser field polarisation will not significantly change the KER distributions. We plot the KER in Fig. 4.3 only for the parallel alignment. Since ionisation processes can be influenced by the shape of the laser field [117, 118], we have computed the KER for parallel alignment also for a Gaussian envelope laser field. We find that the shape of the KER plotted in Fig. 4.3 using the laser field in Eq. 4.6 is in complete agreement with the shape of the KER using a Gaussian envelope laser field. We find that for FDI the computed KER distribution is in good agreement with the experimental one, see Fig. 4.3 (a). Both distributions peak at 21 eV, while the computed KER distribution has a wider tail towards higher field strengths. In the experimental data of the single ionisation channel (Fig.4.3 (a)) an additional peak at $\approx$8 eV is present. This peak is likely due to the bond softening [119] of an intermediate D_2^+ in the experiment. Our model does not include this mechanism and hence, does not show this peak.

The agreement is not as good for the KER distribution for DI shown in Fig. 4.3 (b): the computed distribution peaks at 31 eV while the experimental one peaks at 24 eV. It is possible that our model overestimates the DI probability for high field strengths, see discussion for Fig.4.4. Indeed, when we consider a smaller peak field strength of 0.2 a.u. we find that the intensity averaged KER distributions for FDI and DI, shown in Fig. 4.3 (c) and (d), respectively, are both in better agreement with the experimental ones at the higher intensity. We note, that our results compare better with experiment than previously obtained classical results [109, 110]. In those previous simulations the KER distributions for DI peak at considerably higher energies.

To find the upper limit of intensities that contribute to the KER distributions in Fig. 4.3, we analyse in Fig.4.4 the FDI and DI probabilities as a function of the laser field strength. In this context, probability is the number of FDI or DI events relative
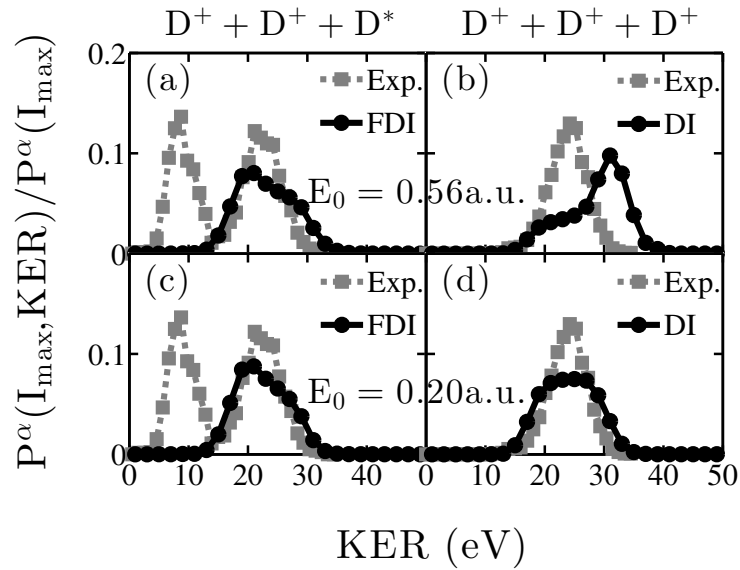
Figure 4.3: Intensity averaged KER distributions for FDI and DI for I_{max} corresponding to a field strength of E_0 =0.56 a.u., (a) and (b), and of E_0 =0.2 a.u., (c) and (d). The grey dashed lines show the relevant experimental results from [59]. Our results and the experimental ones for DI and FDI have been normalised to 1. Note that the experimental results in (a) and (c) have two peaks; it is the area under the higher energy peak that has been normalised to 1.
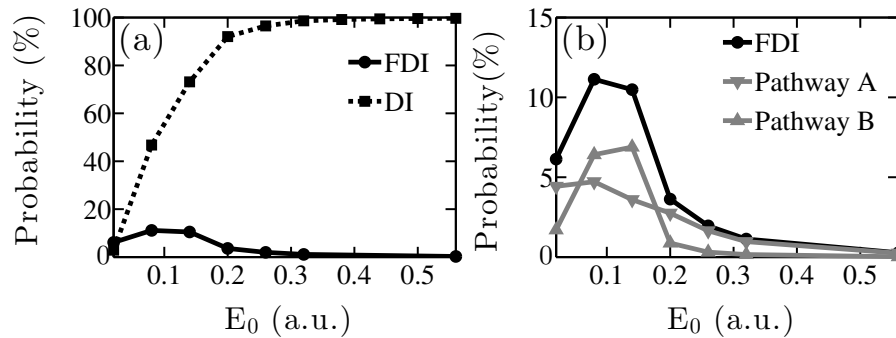
Figure 4.4: The probability (a) for FDI and DI and (b) for pathways A and B of FDI as a function of the field strength E_0. The smallest strength of the laser field we consider in this figure is $E_0 = 0.02$ a.u.

to the number of initialised trajectories. At each intensity we ran enough trajectories to obtain at least 16,000 FDI events and at least 50,000 DI events. Therefore, the statistical error of these results is very small.

Fig.4.4 (a) shows that the DI probability increases quickly as a function of the field strength reaching already a probability of 99.2% at a field strength of 0.38 a.u. Thus, all field strengths up to the peak intensity of 0.56 a.u. contribute significantly

to the intensity averaged KER distribution for DI in Fig.4.3 (b). On the other hand, Fig.4.4 shows that the FDI probability reaches a maximum of 11.1% at an intermediate field strength of 0.08 a.u. and then decreases to 0.3% at a field strength of 0.56 a.u. Combined with the 1/I factor in Eq.4.4, we find that only field strengths up to roughly 0.32 a.u. contribute significantly to the intensity-averaged KER distribution for FDI in Fig.4.3 (a).

We now focus on describing in detail the FDI process for D_3^+. Similar to the case of H_2 in [61] we identify two pathways that can lead to FDI, see section 1.2.2. In the following we refer to the initially tunnel-ionised electron as electron 1 and to the initially bound electron as electron 2. In pathway A, electron 1 escapes, while electron 2 tunnel-ionises later while the laser field is on and is eventually recaptured to a highly-excited state of a D atom. In pathway B, electron 1 is eventually recaptured to a highly excited state of D, while electron 2 tunnel-ionises later but eventually escapes. We find that the distribution of the inter-nuclear distances at the time electron 2 tunnel-ionises peaks around 3 a.u. for D_3^+. It is mainly after electron 2 tunnel-ionises that the nuclei rapidly dissociate, since tunnel-ionisation of electron 2 reduces the screening of the nuclei. We find that the distribution of sum of the kinetic energy of the nuclei at the time electron 2 tunnels is peaked at 0 eV. It, then, follows that the KER distribution for FDI should peak at 3 (number of nuclei)/3 (most probable nuclear distance for Coulomb explosion) a.u. which is 27.2 eV. Indeed, we find the peak of the computed KER distribution for FDI to be around 21 eV. This value is smaller than 27 eV as expected since one electron in FDI events remains bound screening the Coulomb repulsion of the nuclei.

In Fig.4.4 (b) we show that the probability of pathway B of FDI reaches a maximum of 6.9% at a field strength of 0.14 a.u. and then decreases fast, reaching less than 1% at a field strength of 0.2 a.u. The dominance of pathway B at intermediate intensities is due to electron-electron correlation being much more prominent for these intensities [88]. Electron-electron correlation was shown to be more important for pathway B compared to pathway A also for strongly-driven H_2 [111]. This is to be expected since in pathway B electron 1, following tunnel-ionisation,

later returns to the ion and interacts with electron 2. In addition, we find that, for D_3^+, at high intensities, the probability for pathway A of FDI decreases at a much slower rate than the probability of pathway B, see Fig.4.4 (b). The reason is that in pathway A electron 2 tunnels after gaining energy in a frustrated enhanced ionisation process, i.e., electron 2 gains energy from the field in the same way as in an enhanced ionisation process [46–50] but electron 2 eventually does not escape. For higher intensities electron correlation plays a less important role compared to enhanced ionisation. Hence, the probability for pathway A reduces at a smaller rate than the probability for B.

Next, we identify the prevalent ionisation mechanism leading to FDI in D_3^+. Specifically, we determine the probability of over-the-barrier ionisation, P_{OBI}. In our notation P_{OBI} not only refers to the permanent ionisation of electron 2 in pathway B but also includes the temporary ionisation of electron 2 in pathway A before it is being recaptured into an excited D^* state. We find that P_{OBI} is around 9% for a field strength of 0.08 a.u. increasing to 87% at 0.56 a.u. However, for field strengths above 0.32 a.u., the probability of FDI events reduces significantly, see Fig.4.4 (a). Therefore, after integrating over field strengths up to 0.56 a.u., using Eq.4.4, we find that over-the-barrier ionisation accounts for 21% of FDI events. Thus, tunnel-ionisation dominates FDI.
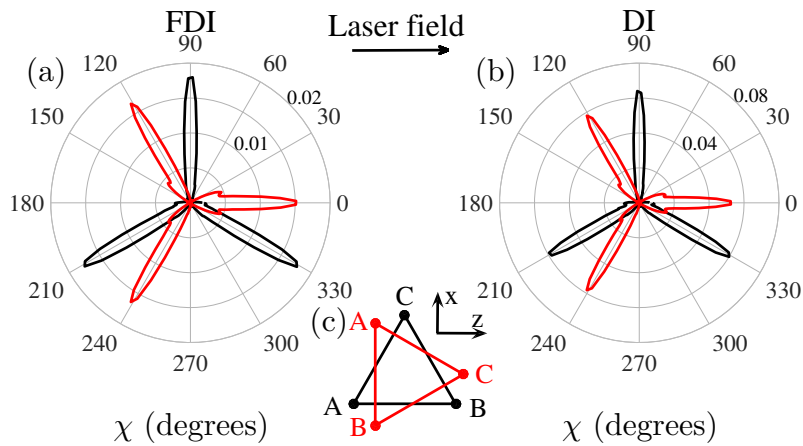
Figure 4.5: The angle of the velocity vector of D^* in FDI (a) and of D^+ in DI (b) with respect to the laser field for parallel (black) and perpendicular (red) molecular alignments. The field strength is 0.08 a.u. (c) The initial state geometric configuration of D_3^+ with respect to the laser field.
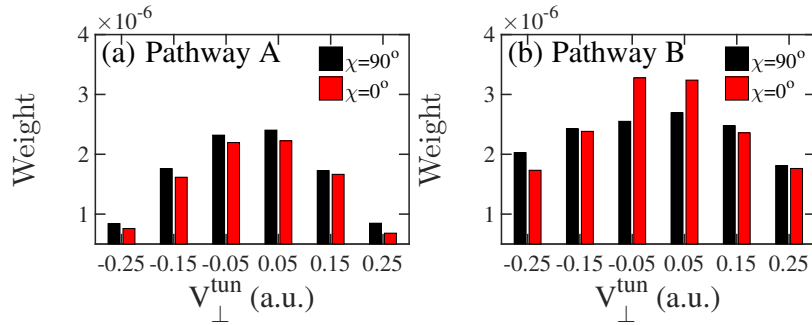
Figure 4.6: The weight of the lobes around 0° and 90° for pathway A (a) and B (b) for different initial velocity of electron 1.

Finally, we identify a feature of the break-up dynamics of the strongly-driven triatomic that is a signature of pathway B and can potentially be observed experimentally. In Fig.4.5 (a)/(b) we plot for FDI/DI the angle χ of the velocity of D^*/D^+ with respect to the laser field for a field strength of 0.08 a.u. for the two alignments of the molecule with respect to the laser field considered. We find that, as for DI, for FDI the angular distribution has a three-lobe structure. The three-lobe structure we obtain for DI is in agreement with previous experiments [59]. For FDI we cannot provide a direct comparison with experiment since the analysed data in [59] includes the angular distribution of all single ionisation events D^++D^++D, i.e., FDI events as well as bond softening events that yield the low KER peak in Fig. 4.3 (a) and (c). For FDI, we find that the three lobes in Fig.4.5 (a) do not have equal weight as is the case for DI in Fig.4.5 (b). Specifically, the lobe around 0° has a 2% higher weight than the other two lobes for perpendicular alignment and the lobe around 90° has a 2% less weight than the other two lobes for parallel alignment in Fig.4.5 (a). With respect to the initial state geometry of the nuclei of D_3^+ in Fig.4.5 (c), this means that the electron that finally stays bound in FDI gets attached for parallel alignment more to either nucleus A or B rather than C while for perpendicular alignment to nucleus C. This difference is reasonable since frustrated enhanced ionisation takes place mainly between the nuclei that are more parallel to the field, A and B for parallel alignment and A and C or B and C for perpendicular alignment. We find that this small difference in the weight of the lobes is present in both pathways A and B.

We find that the probability of the electron that finally remains bound in FDI to get attached to different nuclei varies significantly as a function of the initial velocity of the tunnelling electron. For pathway A as a function of the initial velocity of electron 1, we find that the probability for electron 2 to get attached to nucleus C is between 1.5 % and 2 % smaller/larger than the probability to get attached to nuclei A and B for parallel/perpendicular alignment. Thus, the probability of electron 2 to get attached to nuclei A, B and C is not sensitive to the initial velocity of electron 1. However, we find that for pathway B the probability for electron 1 to get attached to nuclei A, B and C varies with the initial velocity of electron 1 in the direction perpendicular to the field. Namely, for parallel alignment, we find that it is for small initial velocities of electron 1 that the probability of electron 1 to get attached to nucleus C differs the most from the probability of getting attached to nuclei A or B; the probability to get attached to nucleus C is roughly 7 % smaller. For perpendicular alignment, we find again that it is for small initial velocities of electron 1 that the probability of electron 1 to get attached to nucleus C differs the most from the probability of getting attached to nuclei A or B; the probability to get attached to nucleus C is roughly 7 % larger. Expressing the above differences in terms of the lobes of the angular distribution of FDI it means that, for pathway B, for very small initial velocities of electron 1 the lobe around 90° has 7 % less weight than each of the other two lobes of parallel polarisation while the lobe around 0° has 7 % more weight than each of the other two lobes of perpendicular polarisation. Thus, if the initial velocity of electron 1 can be probed experimentally then one would observe a significant difference in the weight of the lobes around 0° and 90° that is due to pathway B. We illustrate the latter in Fig.4.5. In Fig.4.5 (a), we show that in pathway A the difference in weight between the lobes around 0° and 90° is small and insensitive to the initial velocity of electron 1. In contrast, in Fig.4.5 (b), we show that for pathway B the difference in weight between the lobes around 0° and 90° is very sensitive to the initial velocity of electron 1 and is large for small initial velocities.

4.2 Frustrated double and single ionisation of strongly-driven H_3^+

In this section, we study frustrated ionisation of strongly-driven H_3^+ from its ground state. The inter-nuclear distance of the equilateral configuration of H_3^+ in its ground state is 1.65 a.u. [90]. This distance is smaller from the inter-nuclear distance of the initial state we consider for our study of strongly-driven D_3^+. In what follows, we investigate three different processes that take place through Coulomb explosion during the fragmentation of H_3^+, when the molecule is driven by a near-IR intense laser field. Specifically, we study: i) double ionisation where the final fragments are three H^+ ions and two escaping electrons; ii) frustrated double ionisation where the final fragments are a highly excited neutral fragment H^*, two H^+ ions and one escaping electron; iii) frustrated single ionisation where the final fragments are two highly excited neutral fragments H^* and one H^+ ion. We mainly focus on FDI and FSI and investigate their dependence on the intensity of the laser field. For FDI we also study its dependence on the geometry of the initial molecular state. We do the latter by comparing our results for the driven diatomic H_2 with our results for the driven triatomic H_3^+.

4.2.1 Method and initial molecular and field configuration

The linearly polarised laser field we employ in our studies for driven H_3^+ is the same as the one described in Eq.4.1 and illustrated in Fig.4.1:

$$\mathbf{E}(t) = E_0(t)\cos(\omega t)\hat{z}$$

$$E_0(t) = \begin{cases} E_0 & 0 \leq t < 10T \\ E_0 \cos^2 \frac{\omega(t-10T)}{8} & 10T \leq t \leq 12T, \end{cases} \tag{4.6}$$

We take the initial state to be the ground state of H_3^+ with the nuclei forming an equilateral triangle with an inter-nuclear distance R=1.65 a.u. [90]. In our simulations,

we take the three nuclei A, B and C to be on the x-z plane. In addition, we simplify our model by considering the nuclei initially at rest. We note that for $I_{p_1} = 1.208$ a.u. we find that the threshold field strength E_0 for over-the-barrier ionisation is 0.178 a.u. If the instantaneous field strength at the time we start the propagation is smaller than the threshold field strength for over-the-barrier ionisation, we assume that one electron (electron 1) tunnels in the field-lowered Coulomb potential with a tunnelling rate given by the semi-classical formula in [73]. The tunnel electron emerges from the potential barrier with zero velocity along the direction of the laser field and with a velocity that follows a Gaussian distribution in the direction perpendicular to the laser field [70]. If the instantaneous field strength at the time we start the propagation corresponds to the over-the-barrier intensity regime, then we assume that electron 1 tunnel ionises at the maximum of the field lowered Coulomb potential. We take the kinetic energy of electron 1 to be equal to the difference between the first ionisation energy and the maximum of the field-lowered Coulomb potential, for details see [62]. For both below- and over-the-barrier ionisation of electron 1 in the initial state, we describe the initial state of the initially bound electron (electron 2) using the one-electron micro-canonical distribution [89], see section 2.1.4.2.

4.2.2   FDI and FSI in strongly-driven H_3^+

We consider a laser field polarised along one side of the equilateral triangle, see Fig.4.7 (a). In Fig.4.7 (b), we plot the DI and FDI probabilities as a function of the laser field strength. We vary the laser field strength from 0.04 a.u. up to 0.18 a.u., that is up to a field strength just above the threshold value for over-the-barrier ionisation. In this context, probability is the number of DI, FDI and FSI events relative to the number of initialised trajectories. We find that DI is the dominant process at E_0=0.18 a.u. with a probability of 69.4%. The FDI probability reaches a maximum of 9.5% at $E_0 = 0.12$ a.u. and reduces to 5.2% at $E_0 = 0.18$ a.u.

Focusing on FDI during the fragmentation of strongly-driven H_3^+ from its ground state, we find that two main pathways, A and B, contribute to FDI. We
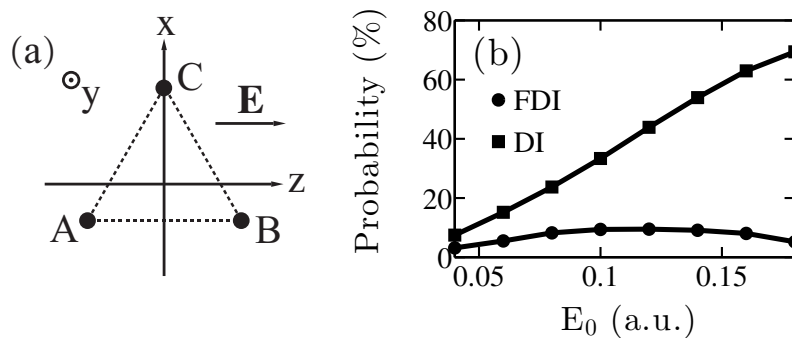
Figure 4.7: Left panel: The initial configuration of H_3^+ relative to the polarisation direction of the laser field. The laser pulse is linearly polarised and aligned along one of the sides of the triatomic molecule. Right panel: The DI and FDI probabilities as a function of the laser field strength E_0. The lowest laser field strength in (b) is $E_0 = 0.04$ a.u.

have previously identified these two pathways in our studies of FDI during the fragmentation of strongly-driven H_2 from its ground state [61] and of strongly-driven D_3^+ from a state other than its ground state in section 4.1.

Fig.4.8 shows that for intermediate strengths of the laser field below the over-the-barrier ionisation threshold, pathway B is the dominant pathway of FDI. Fig.4.8 also shows that pathway A's contribution to FDI increases with increasing field strength. At $E_0 = 0.18$ a.u. both pathways have the same probability. These results are not surprising since, in strongly-driven molecules, electron-electron correlation is more important for intermediate strengths of the laser field, while enhanced ionisation becomes more prominent with increasing strength of the laser field.
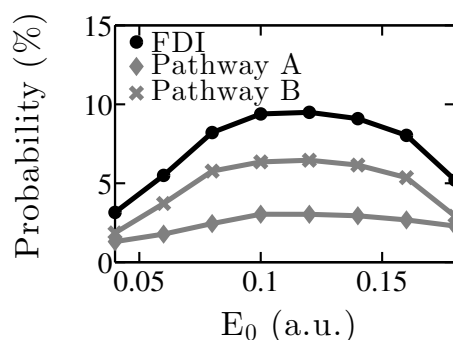
Figure 4.8: The probability of FDI, pathway A and B as a function of the laser field strength. The lowest laser field strength is $E_0 = 0.04$ a.u.

Next, we investigate whether tunnel-ionisation is the underlying mechanism of
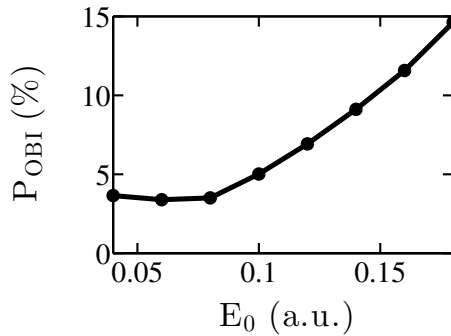
Figure 4.9: P_{OBI} as a function of the laser field strength. The lowest laser field strength is $E_0 = 0.04$ a.u.

FDI, as it was first suggested in [120]. Specifically, we check whether the tunnel or over-the-barrier ionisation is the underlying mechanism of FDI. By over-the-barrier ionisation in FDI, we refer to electron 2 reaching an excited state without tunnelling in pathway A or to electron 2 escaping by over-the-barrier ionisation in pathway B. We denote by P_{OBI} the fraction of FDI over-the-barrier ionisation events out of all FDI events. As shown in Fig.4.9, P_{OBI} increases from 3.7% at E_0=0.04 a.u. to 14.6% for E_0=0.18 a.u. This increase of P_{OBI} is due to over-the-barrier ionisation becoming more prominent with increasing strength of the laser field. We have obtained similar results for the contribution of the over-the-barrier ionisation mechanism in FDI for D_3^+.

In Fig.4.10 (a), we plot the KER distribution for FDI for three different laser field strengths for the laser pulse defined in Eq.4.6. In Fig.4.10 (b), we plot the KER distribution for FDI for three different laser field strengths for a Gaussian envelope laser pulse with full width at half maximum of 40 fs. Comparing Fig.4.10 (a) and (b) shows that the KER distributions have the same shape for both pulses. We find that with increasing strength of the laser field the peak of the KER distribution shifts to higher values, namely, from 23 eV at E_0 =0.06 a.u. to 31 eV at E_0 =0.18 a.u. This increase is consistent with the nuclei Coulomb exploding earlier in time and at smaller inter-nuclear distances for higher strengths of the laser field.

Previously, both for the fragmentation of strongly-driven H_2 from its ground state [62] and of strongly-driven D_3^+ from a superposition of states with inter-nuclear distances larger than the inter-nuclear distance of the ground state, we have
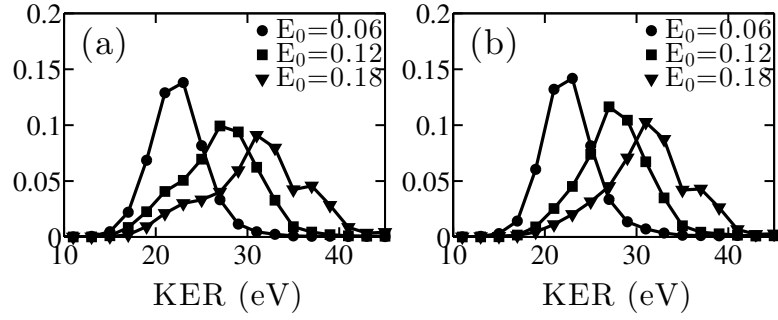
Figure 4.10: Panel (a): the KER distributions for FDI at laser field strengths of 0.06 a.u., 0.12 a.u. and 0.18 a.u. (a) is plotted using the laser pulse defined in Eq. 4.1 and (b) is plotted using a Gaussian envelope laser pulse with t_{FWHM}=40 fs.

found that the peak of the KER distributions can be roughly estimated as follows. We first compute the most probable distance of the nuclei at the time electron 2 tunnels, R_{tun}. For the above-mentioned previous studies, this is also the time when Coulomb explosion of the nuclei mostly sets in. As a result, we found that the KER distributions peak roughly at $1/R_{tun}$ for H_2 and at $3/R_{tun}$ for D_3^+. We find that this is not quite the case for strongly-driven H_3^+ when driven from its ground state. Specifically, in Fig.4.11 , we plot the sum of the kinetic energies of the ions at the time electron 2 tunnels for strongly-driven H_3^+ (a) and H_2 (b) at $E_0 = 0.06$ a.u. We show that the distribution of the sum of the kinetic energies of the nuclei for H_3^+ peaks around 10.5 eV, see Fig.4.11 (a), while for H_2 the distribution peaks around 1.5 eV, see Fig.4.11 (b). Thus, for H_3^+ the nuclei have already acquired a significant amount of kinetic energy by the time electron 2 tunnels unlike H_2^+. This is reasonable since one electron screens more effectively two rather than three nuclei. For H_3^+ fragmenting from its ground state, to roughly estimate where the KER distribution for FDI peaks we have to add $3/R_{tun}$+10.5= 25.3 eV; we have substituted $R_{tun} = 5.5$ a.u. which we obtain from our simulations. Indeed, we find that the KER distribution for FDI peaks at 23 eV, see Fig.4.11, which is slightly less than 25.3 eV, since for FDI the electron that is recaptured screens the Coulomb explosion of the nuclei.

Next, we address FSI where two highly excited neutrals are formed:

$$H_3^+ \rightarrow H^\star + H^\star + H^+.$$
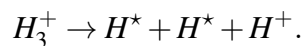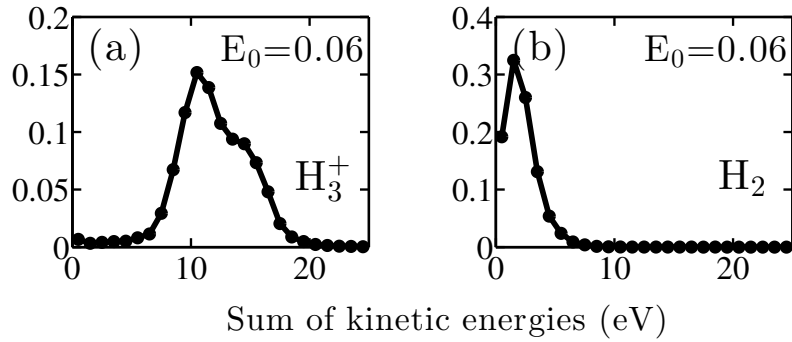
Figure 4.11: The distribution of the sum of the kinetic energies of the nuclei for FDI at the time electron 2 tunnels for (a) H_3^+ and for (b) H_2 at $E_0 = 0.06$ a.u.
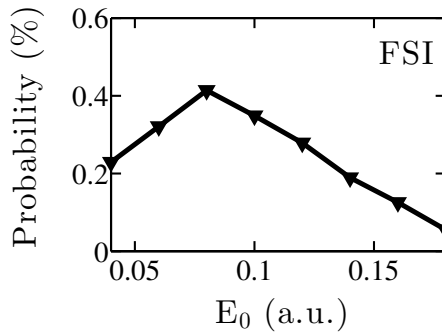
Figure 4.12: FSI probability as a function of the laser field strength. The lowest laser field strength is $E_0 = 0.04$ a.u.
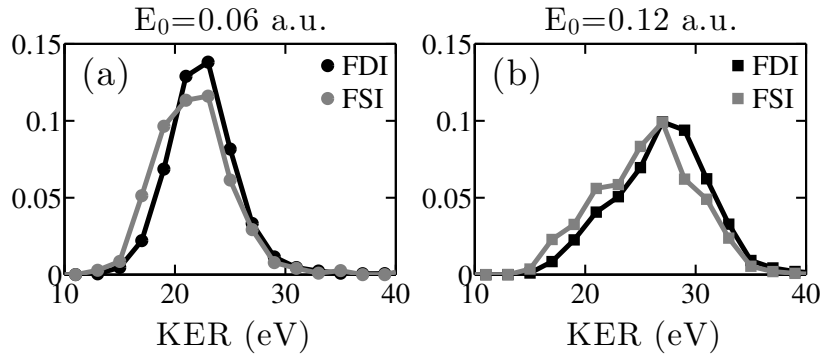
Figure 4.13: KER distributions for FSI at laser field strengths of 0.06 a.u. and 0.12 a.u. The KER distributions for FDI are also presented for comparison.

In Fig.4.12, we show that the FSI probability reaches a maximum probability of 0.4% at $E_0 = 0.08$ a.u. and then reduces fast with increasing field strength reaching 0.06% at $E_0 = 0.18$ a.u. This is consistent with a higher strength of the laser field resulting in a higher probability for an electron to ionise. Thus, FSI is a process roughly 20 times less likely than FDI. A similar conclusion was reached in previous

studies of FSI in the context of strongly-driven H_2 [111]. As for FDI, we plot the KER distributions for FSI for different laser field strengths, see Fig.4.13. We find that the KER distributions for FSI peak at similar energy values as the KER distributions for FDI.

4.2.3 Influence of molecular geometry on FDI

Molecule	$E_0(a.u.)$	$\Gamma(I)$	FDI (%)	Pathway A (%)	Pathway B (%)	DI (%)
H_2	0.04	4.0×10^{-5}	9.6	2.9	6.7	24.4
H_3^+	0.04	2.0×10^{-21}	3.2	1.3	1.9	7.5
H_2	0.06	0.03	9.4	3.2	6.1	39.5
H_3^+	0.06	1.5×10^{-12}	5.5	1.8	3.7	15.2

Table 4.1: The probabilities for FDI and DI as well as the pathways A and B of FDI for H_2 and H_3^+ in a linearly polarised laser field at field strengths 0.04 a.u. or 0.06 a.u.

Molecule	$E_0(a.u.)$	$\Gamma(I)$	FDI (%)	Pathway A (%)	Pathway B (%)	DI (%)
H_2	0.04	4.0×10^{-5}	9.6	2.9	6.7	24.4
H_3^+	0.10	1.5×10^{-5}	9.4	3.0	6.3	33.3
H_2	0.06	0.03	9.4	3.2	6.1	39.5
H_3^+	0.15	0.04	8.7	2.8	5.8	58.3

Table 4.2: The probabilities for FDI and DI as well as the pathways A and B of FDI for H_2 and H_3^+ in a linearly polarised laser field. The laser field strengths are chosen so that the two molecules have similar ionisation probability $\Gamma(I)$.

In what follows, we investigate whether a different molecular geometry affects the FDI probability. We do so, by comparing our results for FDI for the diatomic H_2 with the triatomic H_3^+. First, we consider that both molecules are driven by a linearly polarised laser field of the same laser field strength. The laser field is aligned with one side of the molecules. In Table 4.1, we show the results for laser field strengths of 0.04 a.u. and 0.06 a.u. We find that the FDI probability is much larger for H_2. This result is not surprising. It is easier to ionise an electron in the diatomic molecule, since both molecules are driven with the same laser field strength while the ionisation energies of H_3^+ are much larger than those of H_2. The

first and second ionisation energies of H_3^+ are $I_{p_1} = 1.2079$ a.u. and $I_{p_2} = 1.9300$ a.u., respectively, while for H_2 $I_{p_1} = 0.5669$ a.u. and $I_{p_2} = 1.2843$ a.u.

Next, we compare the FDI probability for both molecules when the ionisation probability $\Gamma(I)$ is the same. The ionisation probability is obtained by integrating, over the duration of the laser pulse, the ionisation rate $\Gamma(t,I)$ for a laser pulse intensity I:

$$\Gamma(I) \approx \int_{t_i}^{t_f} \Gamma(t,I)dt. \tag{4.7}$$

In Table 4.2, we present the FDI probability for H_2 and H_3^+ when $\Gamma(I)$ is of the order of 10^{-5} and 10^{-2}. We find that when $\Gamma(I)$ is the same for both molecules the FDI probability is also roughly the same. Moreover, we find that the probability for pathway B of FDI is for both molecules larger than the probability for pathway A of FDI. The above results suggest that the molecular geometry does not significantly affect the FDI probability.

4.3 Conclusions

Concluding, in section 4.1, using a 3D semi-classical calculation where the Coulomb singularity is fully accounted for, we have shown that our results for the KER distribution for FDI of the strongly-driven D_3^+ agree well with experimental results. We have also found that the underlying mechanism for FDI switches from tunnel to over-the-barrier ionisation with increasing field strength. It would be interesting if future experiments identify the asymmetry in the angular distribution of the D^* fragment for FDI events which we have shown to be a signature of pathway B of FDI.

Moreover, in section 4.2, we have studied the FDI and FSI in strongly-driven H_3^+ from its ground state. We have shown that the distribution of the kinetic energy release of the nuclei for FDI peaks at a higher energy than the one roughly estimated from the Coulomb explosion of the nuclei at the time the bound electron tunnel-ionises. The reason is that by the time the bound electron tunnel-ionises the nuclei have already acquired a significant amount of kinetic energy. As we have shown, this is not the case for strongly-driven H_2^+ when it is fragmenting from its ground state. In addition, we have shown that FSI is a more rare process compared to FDI which is a significant process with probability 10%. Finally, we have shown that the FDI probability is not significantly influenced by the different molecular geometry of H_2 and H_3^+.

Chapter 5

Controlling electron-electron correlation with two-colour laser fields

In theoretical studies of strongly-driven two-electron diatomic and triatomic molecules, two pathways of FDI have been identified [111], see discussion in Chapter 4. Electron-electron correlation has been shown to be important, primarily, for one of the two pathways of FDI. It is well accepted that electron-electron correlation underlies a significant part of double ionisation in strongly-driven molecules, i.e. non-sequential double ionisation [49, 121]. However, the electron-electron correlation in FDI has yet to be accessed experimentally.

In this chapter, we propose a road for future experiments to identify the important role of electron-electron correlation in FDI by employing orthogonally polarised two-colour (OTC) laser fields. We identify the parameters of OTC laser fields that best control the relevant pathway for electron-electron correlation in FDI. We demonstrate traces of attosecond control of electron motion in space and time in two observables of FDI as a function of the time-delay between the fundamental 800 nm and the second harmonic 400 nm laser field. We show that, together, the FDI probability and the momentum of the escaping electron along the fundamental laser field bear clear signatures of the turning on and off of electron-electron correlation. The 3D semi-classical model presented in Chapter 2 is employed for the

simulation.

Two-colour laser fields have been shown to be an efficient tool for controlling electron motion [122, 123] and for steering the outcome of chemical reactions [124–126]. Other applications include the field-free orientation of molecules [127–129], the generation of high-harmonic spectra [130–132] and probing atomic and molecular orbital symmetry [133–135].

5.1 Method and initial molecular and field configuration

We employ the initial state of D_3^+ that is accessed experimentally via the reaction [55, 59]

$$D_2 + D_2^+ \rightarrow D_3^+ + D \tag{5.1}$$
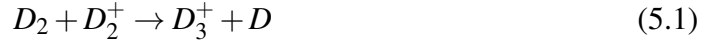
as discussed in section 4.1. It consists of a superposition of triangular-configuration vibrational states $v = 1 - 12$ [55, 112]. We assume that most of the D_3^+ ionisation occurs at the outer classical turning point of the vibrational levels [114, 115]. The turning point varies from 2.04 a.u. ($v = 1$) to 2.92 a.u. ($v = 12$). We initialise the nuclei at rest for all vibrational levels [62]. The combined strength of the two laser fields is within the below-the-barrier ionisation regime. The initial time t_0 is selected using importance sampling [136] in the time interval the two-colour laser field is present, see section 2.1.1. The ionisation rate [73], see section 2.1.2.1.3, is then used as the importance sampling distribution.

The OTC laser field we employ is of the form

$$\mathbf{E}(t, \Delta t) \quad = \quad E_\omega f(t) cos(\omega t)\hat{z} + E_{2\omega} f(t + \Delta t) cos[2\omega(t + \Delta t)]\hat{x} \tag{5.2}$$

with

$$f(t) \quad = \quad exp\left(-2ln2\left(\frac{t}{\tau_{FWHM}}\right)^2\right), \tag{5.3}$$

with $\omega = 0.057$ a.u. for commonly used Ti:sapphire lasers at 800 nm. T_ω and $T_{2\omega}$ are the corresponding periods of the fundamental and second harmonic laser fields, polarised along the $\hat{z}$- and $\hat{x}$-axis, respectively. $\tau_{FWHM} = 40$ fs is the full-width-half-maximum. Δt is the time delay between the $\omega - 2\omega$ pulses. We consider $E_\omega = 0.08$ a.u., since for this field strength pathway B of FDI, where electron-

electron correlation is present, prevails over pathway A—4.8% versus 3.6%, see section 4.1.

To compute the FDI probability as a function of the time delay Δt of the $\omega - 2\omega$ pulses, we use

$$P^{FDI}(\Delta t) = \frac{\sum_{v,i} P_v \Gamma(\Delta t, v, i) P^{FDI}(\Delta t, v, i)}{\sum_{v,i} P_v \Gamma(\Delta t, v, i)}, \tag{5.4}$$

where i refers to the different orientations of the molecule with respect to the z-component of the laser field. We consider only two cases of planar alignment, that is, one side of the equilateral, molecular triangle is either parallel or perpendicular to the $\hat{z}-axis$. $\Gamma(\Delta t, v, i)$ is given by

$$\Gamma(\Delta t, v, i) = \int_{t_i}^{t_f} \Gamma(t_0, \Delta t, v, i) dt_0, \tag{5.5}$$

where the integration is over the duration of the OTC field. $\Gamma(t_0, \Delta t, v, i)$ is the ionisation rate at time t_0 for a certain molecular orientation i, vibrational state v and time delay Δt. P_v is the percentage of the vibrational state v in the initial state of D_3^+ [112]. $P^{FDI}(\Delta t, v, i)$ is the number of FDI events out of all initiated classical trajectories for a certain molecular orientation i, vibrational state v and time delay Δt. Due to the challenging computations involved, we approximate Eq. 5.4 using the $v = 8$ state of D_3^+. This approximation is justified, since we find that the $v = 8$ state contributes the most in the sum in Eq. 5.4. We obtain very similar results for the $v = 7, 9$ states, which contribute to the sum in Eq. 5.4 less than the $v = 8$ state but more than the other states.

5.2   Probability of FDI as a function of the time delay

In Fig.5.1(a), for $E_{2\omega} = 0.05$ a.u., we plot the FDI probability as a function of the time delay for $\Delta t \in [0, T_{2\omega}]$. The results are periodic with $T_{2\omega}/2$. We find that the FDI probability changes significantly with Δt. This change is mainly due to pathway B with probability that varies from 1.2% at $\Delta t =$-0.2, -0.7 $T_{2\omega}$ to 6.7% at $\Delta t =$-0.4, -0.9 $T_{2\omega}$. In contrast, the probability of pathway A changes significantly less varying from 2.4% to 3.7%. For $E_{2\omega}$ <0.05 a.u., the probability of pathway B varies less than for $E_{2\omega} = 0.05$ a.u.
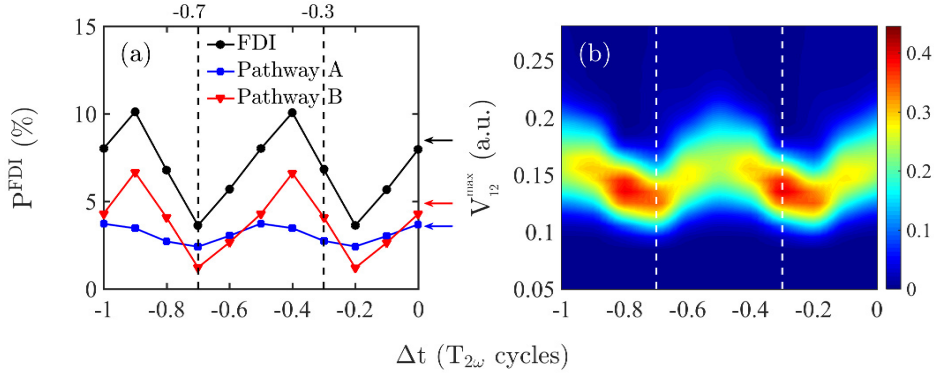
Figure 5.1: (a) The FDI probability and the probabilities of pathways A and B and (b) the distribution of V_{12}^{max} are plotted as a function of Δt for $E_\omega = 0.08$ a.u. and $E_{2\omega} = 0.05$ a.u. In (a) the arrows on the right indicate the corresponding probabilities when $E_{2\omega} = 0$ a.u.

Control of electron-electron correlation in double ionisation in atoms has been demonstrated through the free parameters Δt and $E_{2\omega}$ of OTC laser fields [137–141]. The time-delay between the laser fields can significantly affect the time and the distance of the closest approach of the returning electron [122]. For FDI, this is demonstrated in Fig.5.1(b). For each classical trajectory labelled as FDI, we compute the maximum of the Coulomb potential energy $1/|\mathbf{r}_1 - \mathbf{r}_2|$, V_{12}^{max}. Then, we plot the distribution of V_{12}^{max} as a function of Δt. The minimum values of V_{12}^{max} correspond to electron 1 being at a maximum distance from the core, i.e. minimum electron-electron correlation. Comparing Fig.5.1(a) with (b), we find that these minima occur at the same Δts, where the FDI probability and the probability of

pathway B is minimum, i.e. at Δt =-0.2, -0.7 $T_{2\omega}$.

5.3 Momentum of the ionising electron in FDI as a function of the time delay

The probability of each FDI pathway as well as V_{12}^{max} are not experimentally accessible quantities. To demonstrate the presence of electron-electron correlation in FDI, in addition to the sharp change of the FDI probability with Δt, we need one more experimentally accessible observable. This observable should bare clear signatures of the prevalence of pathway A at the Δts where the minima of the FDI probability occur, i.e. at Δt =-0.2, -0.7 $T_{2\omega}$. We find that such a FDI-observable is the change of the momentum of the escaping electron along the polarisation direction of the fundamental (ω) laser field, p_z, with Δt.
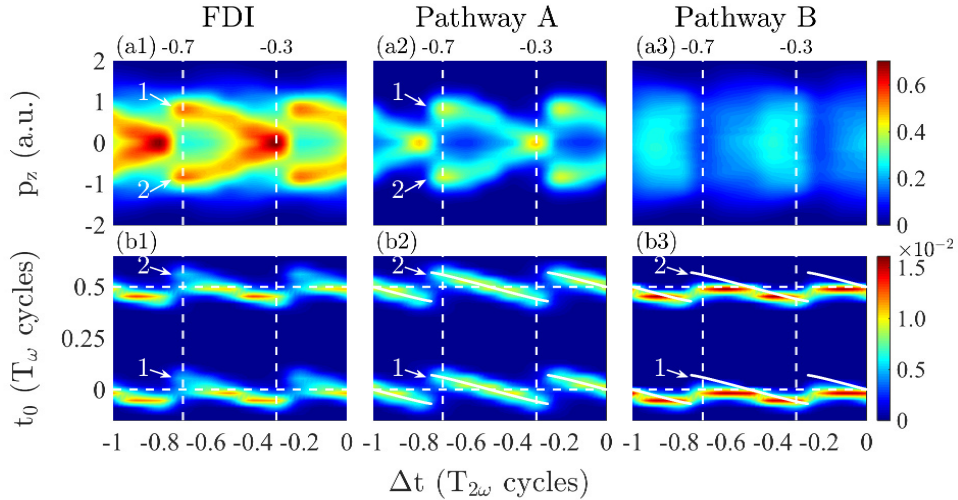
Figure 5.2: The distribution of p_z for FDI (a1) and for pathways A (a2) and B (a3) are plotted as a function of Δt. For each Δt, the distribution of p_z for FDI is normalised to 1 while for pathways A and B it is normalised with respect to the total FDI probability. The distribution of the time electron 1 tunnel-ionises during half cycles 1 and 2 for FDI (b1) and for pathways A (b2) and B (b3) is plotted as a function of Δt. For each Δt, the distribution of t_0 in (b1)-(b3) is normalised to 1. t_{max} is plotted with white dots (appear as white lines) in (b2) and (b3).

In Fig.5.2(a1) we plot the distribution of p_z as a function of Δt for one period

of the results, that is, in the interval $\Delta t \in [-0.7T_{2\omega}, -0.2T_{2\omega}]$ in steps of $\Delta t = 0.1$ $T_{2\omega}$. We find that the distribution of p_z has a V-shape. It consists of two branches that have a maximum split at $\Delta t = $-0.7 $T_{2\omega}$, with peak values of p_z around -0.85 a.u. and 0.85 a.u. The two branches coalesce at $\Delta t = $-0.3 $T_{2\omega}$, with p_z centred around zero. Moreover, FDI events with electron 1 tunnel-ionising during half cycles with extrema at nT_{ω} ($n/2T_{\omega}$) contribute to the upper (lower) branch of the distribution of p_z. n takes both positive and negative integer values. We find that half cycles 1 and 2, see Fig.5.3(a1) and (a2), with extrema at 0 and T/2 of the E_{ω} laser field, respectively, contribute the most to the momentum distribution of p_z. Thus, it suffices to focus our studies on half cycles 1 and 2.
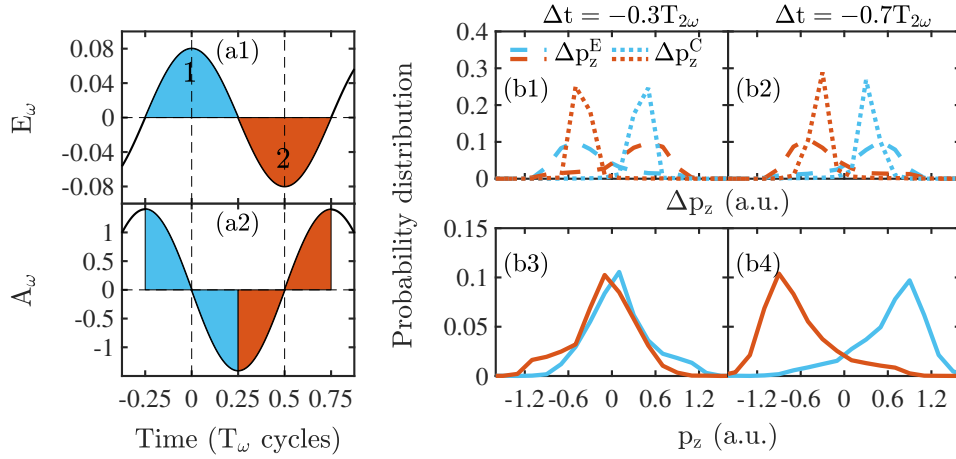
Figure 5.3: Half cycles 1 and 2 for E_{ω} (a1) and its vector potential (a2). For pathway A, the distributions of Δp_z^E and Δp_z^C are plotted for half cycles 1 and 2 for $\Delta t = $-0.3 $T_{2\omega}$ (b1) and $\Delta t = $-0.7 $T_{2\omega}$ (b2). The distribution of p_z is plotted for half cycles 1 and 2 for $\Delta t = $-0.3 $T_{2\omega}$ (b3) and $\Delta t = $-0.7 $T_{2\omega}$ (b4).

First, we investigate the change of the distribution of the time electron 1 tunnel-ionises t_0 with Δt, see Fig.5.2(b1). When the second harmonic (2ω) field is turned off, t_0 is centred around the extrema of half cycles 1 and 2 (not shown). However, when the 2ω-field is turned on, depending on Δt, electron 1 tunnel-ionises at times t_0 that are shifted to the right or to the left of the extrema of half cycles 1 and 2, see Fig.5.2(b1). Moreover, we find that t_0 shifts monotonically from the lowest value of the shift at $\Delta t = -0.3$ $T_{2\omega}$ to its highest value at $\Delta t = -0.7$ $T_{2\omega}$. We find that this change of t_0 is due to the monotonic change with Δt of the time t_{max} when the

magnitude of the OTC laser field is maximum. That is, for each Δt, we compute the time t_{max} when the laser field in Eq. 5.3 is maximum. t_{max} is also the time that the ionisation rate is maximum. We plot t_{max} for half cycles 1 and 2 in Fig.5.2(b2) and (b3). We compare t_{max} with the distribution of t_0 for pathways A and B. We find t_{max} to be closest to the distribution of t_0 for pathway A. Indeed, only when electron 1 is the escaping electron will the time electron 1 tunnel-ionises be roughly equal to the time the ionisation rate is maximum. In pathway B it is electron 2 that escapes. Thus, the time t_0 must be such that both the ionisation rate and the electron-electron correlation efficiently combine to ionise electron 2.

Next, for pathway A, we explain how the two brunches of the distribution of p_z split when t_0 shifts to the right of the extrema of half cycles 1 and 2 (Δt=-0.7 $T_{2\omega}$) or coalesce when t_0 shifts to the left (Δt =-0.3 $T_{2\omega}$). we compute the changes in p_z of the escaping electron 1 due to the ω-field as well as due to the interaction of electron 1 with the core. These momentum changes are given by

$$\Delta p_z^E(\Delta t, t_0) = -\int_{t_0}^{\infty} E_\omega(t)dt \tag{5.6}$$

$$\Delta p_z^C(\Delta t, t_0) = \int_{t_0}^{\infty} \left(\sum_{i=1}^{3} \frac{\mathbf{R_i} - \mathbf{r_1}}{|\mathbf{r_1} - \mathbf{R_i}|^3} + \frac{\mathbf{r_1} - \mathbf{r_2}}{|\mathbf{r_1} - \mathbf{r_2}|^3} \right) \cdot \hat{z}dt, \tag{5.7}$$

with $\mathbf{R}_i$ the position of the nuclei. Using the times t_0 for the events labeled as pathway A, we plot the probability distributions of Δp_z^E and of Δp_z^C at Δt =-0.3 $T_{2\omega}$ and at Δt =-0.7 $T_{2\omega}$ in Fig.5.3(b1) and (b2), respectively. We find that, for both Δts, the distribution of Δp_z^C peaks at positive (negative) values of Δp_z^C when electron 1 tunnel-ionises during half cycle 1 (2). Indeed, during half cycle 1 (2), electron 1 tunnel-ionises to the left (right) of the field-lowered Coulomb potential. Then, the force from the core acts along the positive (negative) $\hat{z}$-axis resulting in the distribution Δp_z^C peaking around positive (negative) values for half cycle 1 (2). We find that the contribution of the electron-electron repulsion term is small compared to the attraction from the nucleus in Δp_z^C. In contrast, the distribution of Δp_z^E peaking at positive or negative values of Δp_z^E depends on whether t_0 shifts to the right or to the left of the extrema of half cycles 1 and 2, i.e. it depends on Δt.

For Δt=-0.3 $T_{2\omega}$, when t_0 shifts to the left of the extrema of half cycles 1 (2), the vector potential is positive (negative) resulting in the distribution of Δp_z^E peaking at negative (positive) values of Δp_z^E. Similarly, for Δt=-0.7 $T_{2\omega}$, the distribution of Δp_z^E peaks at positive (negative) values of Δp_z^E for half cycle 1 (2).

In Fig.5.2(b3) and (b4), we plot the distributions of the final momentum p_z, which is given by $\Delta p_z^E + \Delta p_z^C + p_{z,t_0}$. The distribution of the component of the initial momentum of electron 1, p_{z,t_0}, has a small contribution to p_z and is not shown. In Fig.5.3(b3), for Δt =-0.3 $T_{2\omega}$, we show that the distributions of p_z for half cycles 1 and 2 are similar and peak at zero. They give rise to the two branches of the distribution p_z coalescing in Fig.5.2(a2) and (a1). In Fig.5.3(b4), for Δt =-0.7 $T_{2\omega}$, we find that the distributions of p_z for half cycles 1 and 2 are quite different with peaks at 0.85 a.u. and -0.85 a.u., respectively. They give rise to the split of the two branches of the distribution p_z in Fig.5.2(a2) and (a1). Unlike pathway A, for pathway B the distribution of p_z as a function of Δt in Fig.5.2(a3) is very broad. The reason is that electron 2 has time to interact with the core since it tunnel-ionises after a few cycles of the laser field.

5.4 Triatomic versus diatomic molecules
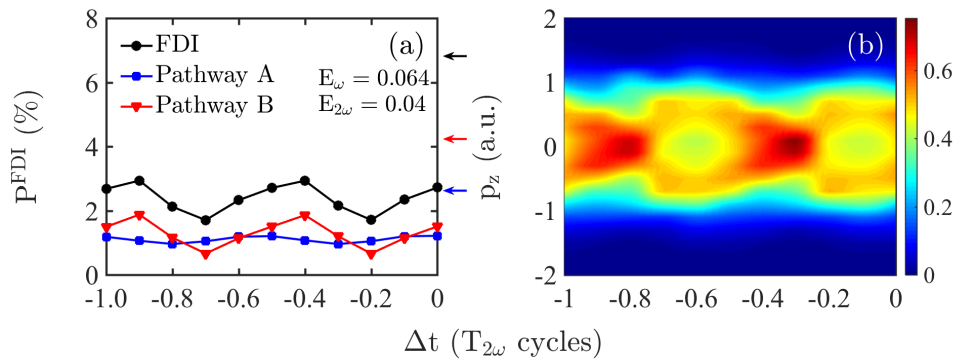
Figure 5.4: (a) and (b) similar to Fig.5.1(a) and Fig.5.2(a1), respectively, for H_2.

Finally, we show that a similar level of control of electron-electron correlation with OTC fields can not be achieved for H_2. We choose $E_\omega = 0.064$ a.u. so

that E_ω for H_2 and D_3^+ has the same percentage difference from the field strength that corresponds to over-the-barrier ionisation. We choose $E_{2\omega} = 0.04$ a.u. so that $E_\omega/E_{2\omega}$ is the same for both molecules. We show in Fig.5.4(a) that, for all Δts, the FDI probability significantly reduces when the 2ω-field is turned on. Indeed, its maximum value is 2.7% compared to 6.8% for $E_{2\omega} = 0$ a.u. In contrast, in D_3^+ the FDI probability changes from 8.5% without 2ω-field to a maximum value of 10.5% for $E_{2\omega} = 0.05$ a.u. We find that the FDI probability as well as the probability of pathway B do not significantly change with Δt. In addition, the two branches of the V-shaped distribution p_z of the escaping electron are not as pronounced in Fig.5.4(b) as for D_3^+. The results in Fig.5.4 are obtained when the inter-nuclear axis of H_2 is parallel to E_ω. We find similar results for a perpendicular orientation, however, for $E_{2\omega} = 0$ a.u., the FDI probability is almost zero. The much lower FDI probability for H_2 when the 2ω laser pulse is switched on shows that the laser pulse that is perpendicularly polarised to the molecular axis drives away a large percentage of the electrons that would otherwise remain in Rydberg states if $E_{2\omega} = 0$. However, for D_3^+, this effect is counteracted by the stronger attractive force an electron experiences due to the presence of a third nucleus in a triangular configuration.

5.5 Conclusions

In conclusion, we have shown that control of electron-electron correlation in FDI can be achieved employing OTC fields in D_3^+. We have found that the FDI probability changes sharply with the time-delay between the two laser fields. Moreover, we have identified a split in the distribution of the final momentum of the escaping electron that takes place at time-delays where the FDI probability is minimum. We have shown this split to be a signature of the absence of electron-electron correlation. It then follows that electron-electron correlation is present for the time-delays, where the FDI probability is maximum. Future experiments can employ our scheme to demonstrate the importance of electron-electron correlation in FDI.

Chapter 6

Conclusions

In this dissertation, we discuss phenomena in strongly-driven atoms and two-electron multi-centre molecules where electron-electron correlation plays an important role. Such phenomena are non-sequential double ionisation in atoms and frustrated double ionisation in molecules. For our studies we have employed sophisticated 3D semi-classical models that are accurate and compare well with experiments and quantum mechanical calculations. These models are much faster than quantum mechanical calculations and very importantly these models offer a physical picture of the mechanisms that underly NSDI and FDI.

We have first studied non-sequential double ionisation in *Ar* when driven by near-single-cycle intense and infrared laser fields. We have investigated NSDI for a range of intensities. For small intensities, we have found that our results agree overall well but do not exactly reproduce a cross-shaped structure in correlated electron momenta distributions that was experimentally identified by recent experimental results. Moreover, we find that at these small intensities both the main double ionisation pathways, the direct and the delayed, contribute to non-sequential double ionisation. Previous studies assumed that only the delayed pathway contributes to NSDI. For these small intensities, we also study how the contribution of the two major pathways of NSDI changes as a function of the carrier-envelope phase of the ultrashort laser pulse. We obtain correlated electron momenta as a function of the carrier-envelope phase that are close to the experimental results. We also find that the width of the experimentally obtained sum of the electron mo-

menta along the polarisation direction of the laser field is well reproduced by our computations. A difference between our results and the experimentally obtained ones is that our computations underestimate the double ionisation events with very small electron momenta. Most probably this implies that our model for *Ar* overestimates the Coulomb attraction and, thus, more accurate effective potentials need to be employed in future calculations. For high intensities, we also find that our computational results for the correlated electron momenta reproduce well a previously experimentally unseen pattern where the electrons escape opposite to each other along the polarisation direction of the laser field. This pattern was previously identified for high intensities for the strongly-driven nitrogen molecule with fixed nuclei and was attributed to sort recollisions. We also find that, for high intensities, soft recollisions in strongly-driven *Ar* lead to an anti-correlation pattern. It will be interesting to include interference effects in future double ionisation studies. Such effects have already been considered in single ionisation of strongly-driven atoms, see Appendix E.

Next, we have investigated double and frustrated double ionisation in strongly-driven two-electron triatomic molecules. For strongly-driven D_3^+, we have compared our results for the distributions of the sum of the final kinetic energies of the nuclei for double and for frustrated double ionisation with experimental results. The initial state of D_3^+ is not the ground state but the one that can be experimentally realised. It corresponds to a superposition of vibrational states with inter-nuclear distances larger than the inter-nuclear distance of the ground state. Fully accounting for the focal volume effect, we have found a very good agreement between our computations and the experimental results for frustrated double ionisation. The agreement is not as good for double ionisation, with our distribution of the sum of the final kinetic energies of the nuclei peaking at a higher energy. We have found that this latter feature can most probably be attributed to our 3D semi-classical model overestimating the probability for double ionisation. Moreover, for double ionisation, a very good agreement was found between our computations and experimental results for the distribution of the angle between the velocity vector of either of the three nu-

clei and the polarisation direction of the laser field. We have also studied frustrated double and frustrated single ionisation for strongly-driven H_3^+ from its ground state. We have shown that for frustrated double ionisation the distribution of the sum of the final kinetic energies of the nuclei can not be accounted for solely from the Coulomb explosion of the nuclei at the time the initial bound electron ionises. We have found the reason to be that for strongly-driven H_3^+ the nuclei have acquired significant kinetic energy already by the time the initially bound electron ionises. We have found this not to be the case for strongly-driven H_2. We have attributed the difference to the initially bound electron screening less efficiently the three nuclei in H_3^+ compared to the two nuclei in H_2^+. In addition, we have found that the probability for frustrated double ionisation in H_3^+ and H_2^+ is roughly the same when the two molecules are strongly-driven by laser pulses with different field strengths corresponding to the same ionisation probability. Thus, the molecular geometry does not seem to play a significant role concerning the probability of frustrated double ionisation in a linearly polarised laser field. Moreover, we have shown that, for intermediate intensities, frustrated single ionisation is a much less probable process compared to frustrated double ionisation in strongly-driven two-electron molecules.

We have shown that two pathways underlie frustrated double ionisation in two-electron triatomic molecules. These pathways have been previously theoretically identified in strongly-driven two-electron diatomic molecules. We have found that in one pathway, A, the initially bound electron gains energy from the laser field in an enhanced-like ionisation process, tunnel-ionises and finally remains bound in a Rydberg state of one of the ions. The other electron that initially tunnel-ionises escapes fast. In pathway B, the electron that initially tunnel-ionises returns to the core and finally remains bound in a Rydberg state in one of the ions. The initially bound electron gains energy from the laser field in an enhanced-like ionisation process but also through electron-electron correlation from the electron that returns to the core. We have found that electron-electron correlation plays a much more important role in pathway B. However, while it is well established by theory and experiment that electron-electron correlation underlies non-sequential double ionisation, this is not

the case for frustrated double ionisation. Given that frustrated double ionisation in molecules is more important a mechanism than non-sequential double ionisation, with roughly a probability of 10% out of all possible ionisation events, it is important for future experiments to establish the presence of electron-electron correlation in frustrated double ionisation. We have therefore provided a road map for future experiments how to establish electron-electron correlation by using two-colour laser fields that are perpendicular polarised to each other. We have shown that two measurable quantities as a function of the time delay between the two laser fields are enough to establish the presence of electron-electron correlation. The first quantity is the probability of frustrated double ionisation as a function of the time delay. We have found that this probability has significant minima, which according to our analysis, correspond to a very small contribution of pathway B to frustrated double ionisation. Moreover, we have shown that the ionising electron momentum along the direction of the laser field exhibits a striking V-pattern as a function of the time delay. We have shown that this V-shape pattern can be solely attributed to pathway A. Very interestingly it is related to the time of tunnel ionisation in the initial state. While in the presence of the fundamental field, i.e. higher field strength, this tunnel-ionisation time in the initial state is centred around the extrema of the laser field, when both pulses are on this tunnel ionisation time shifts to the right or to the left of the extrema of the laser field depending on the time delay. We have shown that the combined effect of the shift of the tunnel-ionisation time and the Coulomb interaction with the nucleus of the escaping electron gives rise to this striking V-shape pattern. Future studies can consider different combinations of laser fields in order to achieve better control of frustrated double ionisation in multi-centre molecules.

Appendix A

Dipole approximation

A classical electromagnetic field in vacuum is described by the electric and magnetic fields $\mathbf{E}(\mathbf{r},t)$ and $\mathbf{B}(\mathbf{r},t)$ that satisfy Maxwell's equations without sources. $\mathbf{E}(\mathbf{r},t)$ and $\mathbf{B}(\mathbf{r},t)$ are expressed as

$$\mathbf{E} = -\nabla\phi - \frac{\partial \mathbf{A}}{\partial t} \tag{A.1}$$

$$\mathbf{B} = \nabla \times \mathbf{A}. \tag{A.2}$$

where $\phi(\mathbf{r},t)$ and $\mathbf{A}(\mathbf{r},t)$ are the scalar and vector potential, respectively. These equations are invariant under the classical gauge transformations

$$\mathbf{A}' = \mathbf{A} + \nabla F \tag{A.3}$$

$$\phi' = \phi - \frac{\partial F}{\partial t}, \tag{A.4}$$

where F is a real, differentiable function of $\mathbf{r}$ and t.

When $kr \ll 1$, then, we can apply the dipole approximation; $k = 2\pi/\lambda$ and λ is the wavelength of the laser field. In this approximation, the vector field has no space dependence, i.e. $\mathbf{A}(\mathbf{r},t) \cong \mathbf{A}(t)$ and Eq.A.3 and A.4 take the form

$$\mathbf{E}(t) = -\frac{d\mathbf{A}(t)}{dt} \tag{A.5}$$

$$\mathbf{B} = \nabla \times \mathbf{A}(t) = 0. \tag{A.6}$$

Furthermore, to obtain the length gauge, $F(\mathbf{r},t)$ is set to equal to $-\mathbf{A}(t) \cdot \mathbf{r}$ and Eq.A.3, A.4 takes the form

$$\mathbf{A}' = 0 \tag{A.7}$$

$$\phi' = \frac{\partial \mathbf{A}}{\partial t} \cdot \mathbf{r} = -\mathbf{E}(t) \cdot \mathbf{r}. \tag{A.8}$$

As a result, a Hamiltonian in the dipole approximation

$$H = \sum_i \frac{1}{2m_i}(\mathbf{p}_i + Q_i\mathbf{A}')^2 + \sum_{i<j} \frac{Q_iQ_j}{|\mathbf{r}_i - \mathbf{r}_j|} + \sum_i Q_i\phi_i', \tag{A.9}$$

in the length gauge takes the form

$$H = \sum_i \frac{\mathbf{p}_i^2}{2m_i} + \sum_{i<j} \frac{Q_iQ_j}{|\mathbf{r}_i - \mathbf{r}_j|} - \sum_i Q_i\mathbf{E}(t) \cdot \mathbf{r}_i, \tag{A.10}$$

where the subscript i refers to different electrons and nuclei. Q_i is the charge of particle i. Eq.A.10 is the Hamiltonian we normally employ in our calculation.

Appendix B

Intensity of a laser field

A monochromatic laser field on the *x-z* plane, in the dipole approximation, is usually expressed as

$$\mathbf{E}(t) = E_0 \left[cos(\omega t + \phi)\hat{z} + \varepsilon sin(\omega t + \phi)\hat{x} \right], \tag{B.1}$$

with E_0 the strength, ε the ellipticity and ω the angular frequency, respectively, of the field. $f(t)$ is the envelope of the laser field. ϕ is the carrier-envelope phase. The intensity of the laser field is defined as:

$$
\begin{aligned}
I &= \frac{\omega}{2\pi} \int_0^{2\pi/\omega} nc\varepsilon_0 \mathbf{E}^2(t) dt \\
&= \frac{\omega}{2\pi} \int_0^{2\pi/\omega} nc\varepsilon_0 E_0^2 \left[cos^2(\omega t + \phi) + \varepsilon^2 sin^2(\omega t + \phi) \right] dt \\
&= \frac{1}{2} nc\varepsilon_0 (1 + \varepsilon^2) E_0^2,
\end{aligned}
\tag{B.2}
$$

where n is the refractive index (n=1 in the vacuum) and ε_0 is the vacuum permittivity. For a linearly polarised laser field ($\varepsilon = 0$) the intensity takes the form

$$I = \frac{1}{2} nc\varepsilon_0 E_0^2. \tag{B.3}$$

Appendix C

Focal volume effect

The focal volume effect that arises from the laser field being spatially inhomogeneous in the focal area has to be accounted for in computations in order to directly compare with the experiment. Next, we briefly outline the method that is following Ref. [106] in order to account for focal volume effect. The experimentally observed yields of an ion for a specific peak intensity I_0 is given by

$$S(I_0) = \int_0^{I_0} P(I) \left[-\frac{\partial V(I_0, I)}{\partial I} \right] dI, \tag{C.1}$$

where $P(I)$ is the probability of producing an ion at intensity I and $V(I_0, I)$ is the volume occupied when the intensity is between I and I_0. We consider the intensity of a Gaussian laser beam given by [106, 142]

$$I(r, z) = I_0 \left(\frac{w_0}{w(z)} \right)^2 \exp\left(-\frac{2r^2}{w^2(z)} \right) \tag{C.2}$$

with

$$w(z) = w_0 \sqrt{1 + \left(\frac{z}{z_R} \right)^2} \tag{C.3}$$

$$z_R = \frac{\pi w_0^2}{\lambda}, \tag{C.4}$$

where $2w_0$ is the beam waist, z_R is the Rayleigh length, λ is the length of the wave. To obtain the focal volume effect at $z = 0$, we compute the volume corresponding

to the area perpendicular to the z axis. This is given by

$$
\begin{aligned}
V(I_0, I) &= \int r \, dr \, d\theta \\
&= \int_0^{2\pi} \int_0^{r(I,z)} r \, dr \, d\theta \\
&= \pi [r(I,0)]^2 = \frac{1}{2} \pi \omega_0^2 \ln\left(\frac{I_0}{I}\right),
\end{aligned}
\tag{C.5}
$$

where $r(I,z)$ is decided by Eq.C.2

$$
r(I,z) = \left\{ \frac{1}{2} \omega_0^2 \left[1 + \left(\frac{z}{z_R}\right)^2 \right] \ln\left[\frac{I_0}{I} \frac{1}{1 + \left(\frac{z}{z_R}\right)^2} \right] \right\}^{\frac{1}{2}}.
\tag{C.6}
$$

Substitute the $V(I_0, I)$ from Eq.C.5 into Eq.C.1 we obtain

$$
\begin{aligned}
S(I_0) &= \int_0^{I_0} P(I) \left[-\frac{\partial V}{\partial I} \right] dI \\
&= \frac{1}{2} \pi \omega_0^2 \int_0^{I_0} \frac{P(I)}{I} dI.
\end{aligned}
\tag{C.7}
$$

Appendix D

Definition of the ionisation time of an electron during the time propagation

During the analysis of the doubly-ionised events we obtain for strongly-driven atoms, we identify the ionisation time of each electron during the time propagation. To calculate this ionisation time for each electron, we employ the compensated energy which was introduced in Ref. [66, 107]. The change of velocity due to the electronic field $\mathbf{E}(t)$ is obtained by

$$\Delta\mathbf{v}(t) = -\int_{t_0}^{t} \mathbf{E}(t)dt, \tag{D.1}$$

where t_0 is the start time of the propagation. Then the compensated energy is defined as [107]

$$E_c(t) = V(t) + \frac{1}{2}\left[\mathbf{v}(t) - \Delta\mathbf{v}(t)\right]^2. \tag{D.2}$$

In the case when the electronic field is given by $\mathbf{E}(t) = E_0 cos(\omega t)\hat{z}$, we get [107]

$$\Delta\mathbf{v}(t) = -\frac{E_0}{\omega}\left[sin(\omega t) - sin(\omega t_0)\right]\hat{z} = \Delta v_z \hat{z}, \tag{D.3}$$

$$E_c(t) = V(t) + \frac{1}{2}\left[v_x^2 + v_y^2 + (v_z - \Delta v_z)^2\right]. \tag{D.4}$$

Note that, in the case that $V(t) = 0$, the compensated energy E_c is constant and positive. Thus in our calculation, we define the ionisation time as the time when the

compensated energy becomes positive and stay positive for the remaining time in the propagation.

Appendix E

Interference effect in semi-classical models

Interference effects in semi-classical models have been previously addressed in Ref. [143, 144]. A Monte Carlo method that also accounts for interference effects has been implemented in Ref. [145]. A more accurate Monte Carlo method that accounts for interference effects has been developed in Ref. [146]. In what follows we briefly describe this latter model.

The propagator between the initial state $(\mathbf{r}_a, t_a)$ and final state $(\mathbf{r}_b, t_b)$ is expressed as [147]

$$K(\mathbf{r}_b, t_b; \mathbf{r}_a, t_a) \;=\; \langle \mathbf{r}_b | e^{-iHt} | \mathbf{r}_a \rangle. \tag{E.1}$$

The semi-classical approximation of this propagator is given by

$$
\begin{aligned}
K^{SC}(\mathbf{r}_b, t_b; \mathbf{r}_a, t_a) &= \langle \mathbf{r}_b | e^{-iHt} | \mathbf{r}_a \rangle^{SC} \\
&= \left(\frac{1}{2\pi i} \right)^{\frac{3}{2}} \sum_j \left[det \left(-\frac{\partial^2 S(\mathbf{r}_b, t_b; \mathbf{r}_a, t_a)}{\partial r_a \partial r_b} \right) \right]^{\frac{1}{2}} e^{iS(\mathbf{r}_b, t_b; \mathbf{r}_a, t_a)},
\end{aligned}
\tag{E.2}
$$

where the substitute j is over all classical trajectories.

$$S(\mathbf{r}_b, t_b; \mathbf{r}_a, t_a) = \int_{t_a}^{t_b} L(\mathbf{p}, \mathbf{r}) dt, \tag{E.3}$$

where $L = T - V$ are the Lagrangian of the electron. Keeping only the exponential

term, we approximate it by

$$K^{SC}(\mathbf{r}_b,t_b;\mathbf{r}_a,t_a) = \sum_j e^{iS(\mathbf{r}_b,t_b;\mathbf{r}_a,t_a)}. \tag{E.4}$$

Accounting for the phase of each trajectory before the exit point , we obtain

$$K^{SC}(\mathbf{r}_b,t_b;\mathbf{r}_a,t_a)\exp(iI_pt_a) = \sum_j e^{i\left[S(\mathbf{r}_b,t_b;\mathbf{r}_a,t_a)+I_pt_a\right]}. \tag{E.5}$$

The trajectories that interfere are those with same final energy, where the ionising electron has the same final momentum. Therefore, the relevant propagator can be obtained from Eq.E.5 by a Flourier transformation

$$K^{SC}(\mathbf{p}_b,t_b;\mathbf{r}_a,t_a)\exp(iI_pt_a) = \sum_j e^{i\left[S(\mathbf{r}_b,t_b;\mathbf{r}_a,t_a)-\mathbf{p}_b\mathbf{r}_b+I_pt_a\right]} \equiv \sum_j e^{i\Phi}. \tag{E.6}$$

Φ is given by [146]

$$\Phi(\mathbf{p}_b,t_b;\mathbf{r}_a,t_a) = -\int_{t_a}^{t_b}\left[\mathbf{r}\cdot\dot{\mathbf{p}}+H(\mathbf{r},\mathbf{p})\right]dt - \mathbf{p}_a\mathbf{r}_a + I_pt_a. \tag{E.7}$$

For the case when the Hamiltonian is given by

$$H(\mathbf{p},\mathbf{r}) = \frac{\mathbf{p}^2}{2} - \frac{Q}{\mathbf{r}} + \mathbf{E}(t)\cdot\mathbf{r}, \tag{E.8}$$

Then

$$\Phi = -\int_{t_0}^{\infty}\left(\frac{\mathbf{p}^2}{2} - \frac{2Q}{\mathbf{r}}\right)dt - \mathbf{p}_0\mathbf{r}_0 + I_pt_0, \tag{E.9}$$

where the start time is assumed to be t_0, the infinity is taken to be the final time.

Next, we split up the time propagation into two intervals form the start of propagation time t_0 to the end of laser pulse t_f and from t_f to the infinity of time, while in the later interval the system is conservative. By doing so one finds that the

phase for trajectory j is given by

$$\Phi_j(t_0, \mathbf{p}_0) = -\mathbf{p}_0 \cdot \mathbf{r}(t_0) + I_p t_0 - \int_{t_0}^{t_f} \left[\frac{\mathbf{p}^2}{2} - \frac{2Q}{r} \right] dt + \Phi_f^C(t_f) \qquad \text{(E.10)}$$

$$\Phi_f^C(t_f) \approx -Q\sqrt{b} \left[\ln g + arcsinh \left(\frac{\mathbf{r}(t_f) \cdot \mathbf{p}(t_f)}{g\sqrt{b}} \right) \right] \qquad \text{(E.11)}$$

with

$$b = \frac{1}{2E_f} \qquad \text{(E.12)}$$

$$g = \sqrt{1 + 2E_f \mathbf{L}_f^2}, \qquad \text{(E.13)}$$

where E_f is the energy of the ionising electron at the end of the laser pulse and $\mathbf{L}_f = \mathbf{r}(t_f) \times \mathbf{p}(t_f)$ is the angular momentum.

Therefore, the ionisation probability for a final momentum $\mathbf{p}$ is given by

$$P(\mathbf{p}) = \left| \sum_j^{N(\mathbf{p})} \sqrt{w_j(t_0, \mathbf{p}_0)} e^{i\Phi_j(t_0, \mathbf{p}_0)} \right|^2 \qquad \text{(E.14)}$$

with $w_j(t_0, \mathbf{p}_0)$ the weight of the trajectory j for an electron tunnel-ionising with momentum $\mathbf{p}_0$ at time t_0 in the initial condition and $N(\mathbf{p})$ the number of electrons with final momentum $\mathbf{p}$.

Bibliography

[1] T. H. Maiman. Stimulated optical radiation in ruby. *Nature*, 187:493–494, 1960.

[2] M. Hentschel, R. Kienberger, Ch. Spielmann, G. A. Reider, N. Milosevic, T. Brabec, P. Corkum, U. Heinzmann, M. Drescher, and F. Krausz. Attosecond metrology. *Nature*, 414:509–513, 2001.

[3] E. Goulielmakis, M. Schultze, M. Hofstetter, V. S. Yakovlev, J. Gagnon, M. Uiberacker, A. L. Aquila, E. M. Gullikson, D. T. Attwood, R. Kienberger, F. Krausz, and U. Kleineberg. Single-cycle nonlinear optics. *Science*, 320(5883):1614–1617, 2008.

[4] H. Mashiko, S. Gilbertson, M. Chini, X. Feng, C. Yun, H. Wang, S. D. Khan, S. Chen, and Z. Chang. Extreme ultraviolet supercontinua supporting pulse durations of less than one atomic unit of time. *Opt. Lett.*, 34(21):3337–3339, Nov 2009.

[5] H. Niikura, F. Legare, R. Hasbani, M. Yu. Ivanov, D. M. Villeneuve, and P. B. Corkum. Probing molecular dynamics with attosecond resolution using correlated wave packet pairs. *Nature*, 421(6925):826–829, Feb 2003.

[6] S. Baker, J. S. Robinson, C. A. Haworth, H. Teng, R. A. Smith, C. C. Chirilă, M. Lein, J. W. G. Tisch, and J. P. Marangos. Probing proton dynamics in molecules on an attosecond time scale. *Science*, 312(5772):424–427, 2006.

[7] P. B. Corkum and F. Krausz. Attosecond science. *Nat. Phys.*, 3(6):381–387, Jun 2007.

[8] F. Krausz and M. Ivanov. Attosecond physics. *Rev. Mod. Phys.*, 81:163–234, Feb 2009.

[9] L. Plaja, R. Torres, and A. Zaïr. *Attosecond Physics: Attosecond Measurements and Control of Physical Systems*. Springer Series in Optical Sciences. Springer Berlin Heidelberg, 2013.

[10] K. Burnett, V. C. Reed, and P. L. Knight. Atoms in ultra-intense laser fields. *J. Phys. B: At. Mol. Opt. Phys.*, 26(4):561, 1993.

[11] J. H. Posthumus. The dynamics of small molecules in intense laser fields. *Rep. Prog. Phys.*, 67(5):623, 2004.

[12] P. M. Paul, E. S. Toma, P. Breger, G. Mullot, F. Aug, Ph. Balcou, H. G. Muller, and P. Agostini. Observation of a train of attosecond pulses from high harmonic generation. *Science*, 292(5522):1689–1692, 2001.

[13] A. McPherson, G. Gibson, H. Jara, U. Johann, T. S. Luk, I. A. McIntyre, K. Boyer, and C. K. Rhodes. Studies of multiphoton production of vacuum-ultraviolet radiation in the rare gases. *J. Opt. Soc. Am. B*, 4(4):595–601, Apr 1987.

[14] M. Ferray, A. L'Huillier, X. F. Li, L. A. Lompre, G. Mainfray, and C. Manus. Multiple-harmonic conversion of 1064 nm radiation in rare gases. *J. Phys. B: At. Mol. Opt. Phys.*, 21(3):L31, 1988.

[15] Anne L'Huillier, M. Lewenstein, P. Salières, Ph. Balcou, M. Yu. Ivanov, J. Larsson, and C. G. Wahlström. High-order harmonic-generation cutoff. *Phys. Rev. A*, 48:R3433–R3436, Nov 1993.

[16] P. B. Corkum. Plasma perspective on strong field multiphoton ionization. *Phys. Rev. Lett.*, 71:1994–1997, Sep 1993.

[17] W. Becker and H. Rottke. Many-electron strong-field physics. *Contemp. Phys.*, 49(3):199–223, 2008.

[18] J. L. Krause, K. J. Schafer, and K. C. Kulander. High-order harmonic generation from atoms and ions in the high intensity regime. *Phys. Rev. Lett.*, 68:3535–3538, Jun 1992.

[19] M. Lewenstein, Ph. Balcou, M. Yu. Ivanov, A. L'Huillier, and P. B. Corkum. Theory of high-harmonic generation by low-frequency laser fields. *Phys. Rev. A*, 49:2117–2132, Mar 1994.

[20] A. L'Huillier, L. A. Lompre, G. Mainfray, and C. Manus. Multiply charged ions formed by multiphoton absorption processes in the continuum. *Phys. Rev. Lett.*, 48:1814–1817, Jun 1982.

[21] A. l'Huillier, L. A. Lompre, G. Mainfray, and C. Manus. Multiply charged ions induced by multiphoton absorption in rare gases at 0.53 μm. *Phys. Rev. A*, 27:2503–2512, May 1983.

[22] D. N. Fittinghoff, P. R. Bolton, B. Chang, and K. C. Kulander. Observation of nonsequential double ionization of helium with optical tunneling. *Phys. Rev. Lett.*, 69:2642–2645, Nov 1992.

[23] D. Charalambidis, P. Lambropoulos, H. Schröder, O. Faucher, H. Xu, M. Wagner, and C. Fotakis. Settling a long-standing question on strong-field double ionization. *Phys. Rev. A*, 50:R2822–R2825, Oct 1994.

[24] B. Walker, B. Sheehy, L. F. DiMauro, P. Agostini, K. J. Schafer, and K. C. Kulander. Precision measurement of strong field double ionization of helium. *Phys. Rev. Lett.*, 73:1227–1230, Aug 1994.

[25] M. V. Ammosov, N. B. Delone, and V. P. Krainov. Tunnel ionization of complex atoms and of atomic ions in an alternating electromagnetic field. *JETP*, 64:1191–1194, Apr 1986.

[26] A. M. Perelomov, V. S. Popov, and M. V. Terent'ev. Ionization of atoms in an alternating electric field. *JETP*, 23:924–934, 1966.

[27] K. Kondo, A. Sagisaka, T. Tamida, Y. Nabekawa, and S. Watanabe. Wavelength dependence of nonsequential double ionization in He. *Phys. Rev. A*, 48:R2531–R2533, Oct 1993.

[28] E. P. Mansson, D. Guenot, C. L. Arnold, D. Kroon, S. Kasper, J. M. Dahlstrom, E. Lindroth, A. S. Kheifets, A. L'Huillier, S. L. Sorensen, and M. Gisselbrecht. Double ionization probed on the attosecond timescale. *Nat. Phys.*, 10:207–211, Dec 2014.

[29] S. Augst, A. Talebpour, S. L. Chin, Y. Beaudoin, and M. Chaker. Nonsequential triple ionization of argon atoms in a high-intensity laser field. *Phys. Rev. A*, 52:R917–R919, Aug 1995.

[30] Th. Weber, M. Weckenbrock, A. Staudte, L. Spielberger, O. Jagutzki, V. Mergel, F. Afaneh, G. Urbasch, M. Vollmer, H. Giessen, and R. Dörner. Recoil-ion momentum distributions for single and double ionization of helium in strong laser fields. *Phys. Rev. Lett.*, 84:443–446, Jan 2000.

[31] R. Moshammer, B. Feuerstein, W. Schmitt, A. Dorn, C. D. Schröter, J. Ullrich, H. Rottke, C. Trump, M. Wittmann, G. Korn, K. Hoffmann, and W. Sandner. Momentum distributions of Ne^{n+} ions created by an intense ultrashort laser pulse. *Phys. Rev. Lett.*, 84:447–450, Jan 2000.

[32] Th. Weber, H. Giessen, M. Weckenbrock, G. Urbasch, A. Staudte, L. Spielberger, O. Jagutzki, V. Mergel, M. Vollmer, and R. Dorner. Correlated electron emission in multiphoton double ionization. *Nature*, 405(6787):658–661, Jun 2000.

[33] R. Kopold, W. Becker, H. Rottke, and W. Sandner. Routes to nonsequential double ionization. *Phys. Rev. Lett.*, 85:3781–3784, Oct 2000.

[34] B. Feuerstein, R. Moshammer, D. Fischer, A. Dorn, C. D. Schröter, J. Deipenwisch, J. R. Crespo Lopez-Urrutia, C. Höhr, P. Neumayer, J. Ullrich, H. Rottke, C. Trump, M. Wittmann, G. Korn, and W. Sandner. Sepa-

ration of recollision mechanisms in nonsequential strong field double ionization of Ar: The role of excitation tunneling. *Phys. Rev. Lett.*, 87:043003, Jul 2001.

[35] A. Emmanouilidou, J. S. Parker, L. R. Moore, and K. T. Taylor. Direct versus delayed pathways in strong-field non-sequential double ionization. *New J. Phys.*, 13(4):043001, 2011.

[36] N. Camus, B. Fischer, M. Kremer, V. Sharma, A. Rudenko, B. Bergues, M. Kübel, N. G. Johnson, M. F. Kling, T. Pfeifer, J. Ullrich, and R. Moshammer. Attosecond correlated dynamics of two electrons passing through a transition state. *Phys. Rev. Lett.*, 108:073003, Feb 2012.

[37] B. Bergues, M. Kübel, N. G. Johnson, B. Fischer, N. Camus, K. J. Betsch, O. Herrwerth, A. Senftleben, A. M. Sayler, T. Rathje, T. Pfeifer, I. Ben-Itzhak, R. R. Jones, G. G. Paulus, F. Krausz, R. Moshammer, J. Ullrich, and M. F. Kling. Attosecond tracing of correlated electron-emission in nonsequential double ionization. *Nat. Commun.*, 3:813, May 2012.

[38] J. S. Parker, B. J. S. Doherty, K. T. Taylor, K. D. Schultz, C. I. Blaga, and L. F. DiMauro. High-energy cutoff in the spectrum of strong-field nonsequential double ionization. *Phys. Rev. Lett.*, 96:133001, Apr 2006.

[39] L. Fu, J. Liu, and S. Chen. Correlated electron emission in laser-induced nonsequence double ionization of helium. *Phys. Rev. A*, 65:021406, Jan 2002.

[40] S. L. Haan, L. Breen, A. Karim, and J. H. Eberly. Variable time lag and backward ejection in full-dimensional analysis of strong-field double ionization. *Phys. Rev. Lett.*, 97:103008, Sep 2006.

[41] J. Liu, D. F. Ye, J. Chen, and X. Liu. Complex dynamics of correlated electrons in molecular double ionization by an ultrashort intense laser pulse. *Phys. Rev. Lett.*, 99:013003, Jul 2007.

[42] A. Emmanouilidou. Recoil collisions as a portal to field-assisted ionization at near-uv frequencies in the strong-field double ionization of helium. *Phys. Rev. A*, 78:023411, Aug 2008.

[43] M. Kitzler and S. Gräfe. *Ultrafast Dynamics Driven by Intense Light Pulses: From Atoms to Solids, from Lasers to Intense X-rays*. Springer Series on Atomic, Optical, and Plasma Physics. Springer International Publishing, 2015.

[44] T. Nubbemeyer, K. Gorling, A. Saenz, U. Eichmann, and W. Sandner. Strong-field tunneling without ionization. *Phys. Rev. Lett.*, 101:233001, Dec 2008.

[45] B. Manschwetus, T. Nubbemeyer, K. Gorling, G. Steinmeyer, U. Eichmann, H. Rottke, and W. Sandner. Strong laser field fragmentation of H_2: Coulomb explosion without double ionization. *Phys. Rev. Lett.*, 102:113002, Mar 2009.

[46] T. Seideman, M. Yu. Ivanov, and P. B. Corkum. Role of electron localization in intense-field molecular ionization. *Phys. Rev. Lett.*, 75:2819–2822, Oct 1995.

[47] T. Zuo and A. D. Bandrauk. Charge-resonance-enhanced ionization of diatomic molecular ions by intense lasers. *Phys. Rev. A*, 52:R2511–R2514, Oct 1995.

[48] D. M. Villeneuve, M. Yu. Ivanov, and P. B. Corkum. Enhanced ionization of diatomic molecules in strong laser fields: A classical model. *Phys. Rev. A*, 54:736–741, Jul 1996.

[49] H. Niikura, F. Legare, R. Hasbani, A. D. Bandrauk, M. Yu. Ivanov, D. M. Villeneuve, and P. B. Corkum. Sub-laser-cycle electron pulses for probing molecular dynamics. *Nature*, 417(6892):917–922, jun 2002.

[50] E. Dehghanian, A. D. Bandrauk, and G. L. Kamta. Enhanced ionization

of the H_2 molecule driven by intense ultrashort laser pulses. *Phys. Rev. A*, 81:061403, Jun 2010.

[51] J. Wu, M. Meckel, L. Ph. H. Schmidt, M. Kunitski, S. Voss, H. Sann, H. Kim, T. Jahnke, A. Czasch, and R. Dörner. Probing the tunnelling site of electrons in strong field enhanced ionization of molecules. *Nat. Commun.*, 3:1113, Oct 2012.

[52] J. Wu, A. Vredenborg, B. Ulrich, L. Ph. H. Schmidt, M. Meckel, S. Voss, H. Sann, H. Kim, T. Jahnke, and R. Dörner. Multiple recapture of electrons in multiple ionization of the argon dimer by a strong laser field. *Phys. Rev. Lett.*, 107:043003, Jul 2011.

[53] B. Manschwetus, H. Rottke, G. Steinmeyer, L. Foucar, A. Czasch, H. Schmidt-Böcking, and W. Sandner. Mechanisms underlying strong-field double ionization of argon dimers. *Phys. Rev. A*, 82:013413, Jul 2010.

[54] T. Nubbemeyer, U. Eichmann, and W. Sandner. Excited neutral atomic fragments in the strong-field dissociation of N_2 molecules. *J. Phys. B: At. Mol. Opt. Phys.*, 42(13):134010, 2009.

[55] J. McKenna, A. M. Sayler, B. Gaire, Nora G. Johnson, K. D. Carnes, B. D. Esry, and I. Ben-Itzhak. Benchmark measurements of H_3^+ nonlinear dynamics in intense ultrashort laser pulses. *Phys. Rev. Lett.*, 103:103004, Sep 2009.

[56] J. D. Alexander, C. R. Calvert, R. B. King, O. Kelly, L. Graham, W. A. Bryan, G. R. A. J. Nemeth, W. R. Newell, C. A. Froud, I. C. E. Turcu, E. Springate, I. D. Williams, and J. B. Greenwood. Photodissociation of D_3^+ in an intense, femtosecond laser field. *J. Phys. B: At. Mol. Opt. Phys.*, 42(14):141004, 2009.

[57] A. M. Sayler, J. McKenna, B. Gaire, N. G. Kling, K. D. Carnes, and I. Ben-Itzhak. Measurements of intense ultrafast laser-driven D_3^+ fragmentation dynamics. *Phys. Rev. A*, 86:033425, Sep 2012.

[58] B. Gaire, J. McKenna, M. Zohrabi, K. D. Carnes, B. D. Esry, and I. Ben-Itzhak. Dynamics of $D_3{}^+$ slow dissociation induced by intense ultrashort laser pulses. *Phys. Rev. A*, 85:023419, Feb 2012.

[59] J. McKenna, A. M. Sayler, B. Gaire, N. G. Kling, B. D. Esry, K. D. Carnes, and I. Ben-Itzhak. Frustrated tunnelling ionization during strong-field fragmentation of D_3^+. *New J. Phys.*, 14(10):103029, 2012.

[60] C. Lefebvre, H. Z. Lu, S. Chelkowski, and A. D. Bandrauk. Electron-nuclear dynamics of the one-electron nonlinear polyatomic molecule H_3^{2+} in ultra-short intense laser pulses. *Phys. Rev. A*, 89:023403, Feb 2014.

[61] A. Emmanouilidou, C. Lazarou, A. Staudte, and U. Eichmann. Routes to formation of highly excited neutral atoms in the breakup of strongly driven H_2. *Phys. Rev. A*, 85:011402, Jan 2012.

[62] H. Price, C. Lazarou, and A. Emmanouilidou. Toolkit for semiclassical computations for strongly driven molecules: Frustrated ionization of H_2 driven by elliptical laser fields. *Phys. Rev. A*, 90:053419, Nov 2014.

[63] A. Chen, H. Price, A. Staudte, and A. Emmanouilidou. Frustrated double ionization in two-electron triatomic molecules. *Phys. Rev. A*, 94:043408, Oct 2016.

[64] R. Abrines and I. C. Percival. Classical theory of charge transfer and ionization of hydrogen atoms by protons. *Proc. Phys. Soc.*, 88(4):861, 1966.

[65] I. C. Percival and D. Richards. The theory of collisions between charged particles and highly excited atoms. *Adv. At. Mol. Phys.*, 11:1 – 82, 1976.

[66] J. G. Leopold and I. C. Percival. Microwave ionization and excitation of rydberg atoms. *Phys. Rev. Lett.*, 41:944–947, Oct 1978.

[67] G. Bandarage and R. Parson. Saddle-point electrons in proton-impact ionization of H: A classical trajectory study. *Phys. Rev. A*, 41:5878–5888, Jun 1990.

[68] J. Grochmalicki, M. Lewenstein, and K. Rząewski. Stabilization of atoms in superintense laser fields: Is it real? *Phys. Rev. Lett.*, 66:1038–1041, Feb 1991.

[69] R. Y. Rubinstein. *Simulation and the Monte Carlo Method, 2nd Edition Set*. Wiley Series in Probability and Statistics. Wiley, 2008.

[70] N. B. Delone and V. P. Krainov. Energy and angular electron spectra for the tunnel ionization of atoms by strong low-frequency radiation. *J. Opt. Soc. Am. B*, 8(6):1207–1211, Jun 1991.

[71] X. M. Tong, Z. X. Zhao, and C. D. Lin. Theory of molecular tunneling ionization. *Phys. Rev. A*, 66:033402, Sep 2002.

[72] S.-F. Zhao, C. Jin, A.-T. Le, T. F. Jiang, and C. D. Lin. Determination of structure parameters in strong-field tunneling ionization theory of molecules. *Phys. Rev. A*, 81:033423, Mar 2010.

[73] R. Murray, M. Spanner, S. Patchkovskii, and M. Yu. Ivanov. Tunnel ionization of molecules and orbital imaging. *Phys. Rev. Lett.*, 106:173001, Apr 2011.

[74] C. J. Joachain, N. J. Kylstra, and R. M. Potvliege. *Atoms in Intense Laser Fields:*. Cambridge University Press, Cambridge, Dec 2011.

[75] S. Larochelle, A. Talebpour, and S. L. Chin. Non-sequential multiple ionization of rare gas atoms in a Ti:sapphire laser field. *J. Phys. B: At. Mol. Opt. Phys.*, 31(6):1201, 1998.

[76] S. Augst, D. D. Meyerhofer, D. Strickland, and S. L. Chin. Laser ionization of noble gases by coulomb-barrier suppression. *J. Opt. Soc. Am. B*, 8(4):858–867, Apr 1991.

[77] X. M. Tong and C. D. Lin. Empirical formula for static field ionization rates of atoms and molecules by lasers in the barrier-suppression regime. *J. Phys. B: At. Mol. Opt. Phys.*, 38(15):2593, 2005.

[78] Ph. V. Demekhin, A. Ehresmann, and V. L. Sukhorukov. Single center method: A computational tool for ionization and electronic excitation studies of molecules. *J. Chem. Phys.*, 134(2):024113, 2011.

[79] S.-F. Zhao, J. Xu, Cheng Jin, A.-T. Le, and C. D. Lin. Effect of orbital symmetry on the orientation dependence of strong field tunnelling ionization of nonlinear polyatomic molecules. *J. Phys. B: At. Mol. Opt. Phys.*, 44(3):035601, 2011.

[80] O. I. Tolstikhin, T. Morishita, and L. B. Madsen. Theory of tunneling ionization of molecules: Weak-field asymptotics including dipole effects. *Phys. Rev. A*, 84:053423, Nov 2011.

[81] S. Patchkovskii, Z. Zhao, T. Brabec, and D. M. Villeneuve. High harmonic generation and molecular orbital tomography in multielectron systems. *J. Chem. Phys.*, 126(11):114306, 2007.

[82] X. Hao, G. Wang, X. Jia, W. Li, J. Liu, and J. Chen. Nonsequential double ionization of Ne in an elliptically polarized intense laser field. *Phys. Rev. A*, 80:023408, Aug 2009.

[83] L. Fechner, N. Camus, J. Ullrich, T. Pfeifer, and R. Moshammer. Strong-field tunneling from a coherent superposition of electronic states. *Phys. Rev. Lett.*, 112:213001, May 2014.

[84] R. Abrines and I. C. Percival. A generalized correspondence principle and proton-hydrogen collisions. *Proc. Phys. Soc.*, 88(4):873, 1966.

[85] L. Meng, C. O. Reinhold, and R. E. Olson. Electron removal from molecular hydrogen by fully stripped ions at intermediate energies. *Phys. Rev. A*, 40:3637–3645, Oct 1989.

[86] L. Fu, J. Liu, J. Chen, and S. Chen. Classical collisional trajectories as the source of strong-field double ionization of helium in the knee regime. *Phys. Rev. A*, 63:043416, Mar 2001.

[87] D. F. Ye, J. Chen, and J. Liu. Classical trajectory perspective on double-ionization dynamics of diatomic molecules irradiated by ultrashort intense laser pulses. *Phys. Rev. A*, 77:013403, Jan 2008.

[88] A. Emmanouilidou and A. Staudte. Intensity dependence of strong-field double-ionization mechanisms: From field-assisted recollision ionization to recollision-assisted field ionization. *Phys. Rev. A*, 80:053415, Nov 2009.

[89] C. Lazarou, A. Chen, and A. Emmanouilidou. Microcanonical distribution for one-electron triatomic molecules. *arXiv:1511.05455*, Nov 2015.

[90] M. E. Schwartz and L. J. Schaad. Ab initio studies of small molecules using 1s gaussian basis functions. II. H_3^+. *J. Chem. Phys.*, 47(12):5325–5334, 1967.

[91] H.-J. Werner, P. J. Knowles, G. Knizia, F. R. Manby, M. Schütz, et al. Molpro, version 2009, a package of ab initio programs, 2009. see http://www.molpro.net.

[92] D. C. Heggie. A global regularisation of the gravitationaln-body problem. *Celestial mechanics*, 10(2):217–241, 1974.

[93] J. S. Cohen. Reexamination of over-the-barrier and tunneling ionization of the hydrogen atom in an intense field. *Phys. Rev. A*, 64:043412, Sep 2001.

[94] K. T. Taylor, J. S. Parker, D. Dundas, and K. J. Meharg. Theory of laser-driven double-ionization of atoms at ti:sapphire laser wavelengths. *J. Mod. Opt.*, 54(13-15):1959–1983, 2007.

[95] A. Becker, R. Dörner, and R. Moshammer. Multiple fragmentation of atoms in femtosecond laser pulses. *J. Phys. B: At. Mol. Opt. Phys.*, 38(9):S753, 2005.

[96] J. Ullrich, R. Moshammer, A. Dorn, R. Dörner, L. Ph. H. Schmidt, and H. Schmidt-Böcking. Recoil-ion and electron momentum spectroscopy: reaction-microscopes. *Rep. Prog. Phys.*, 66(9):1463, 2003.

[97] M. Kübel, C. Burger, Nora G. Kling, T. Pischke, L. Beaufore, I. Ben-Itzhak, G. G. Paulus, J. Ullrich, T. Pfeifer, R. Moshammer, M. F. Kling, and B. Bergues. Complete characterization of single-cycle double ionization of argon from the nonsequential to the sequential ionization regime. *Phys. Rev. A*, 93:053422, May 2016.

[98] N. G. Johnson, O. Herrwerth, A. Wirth, S. De, I. Ben-Itzhak, M. Lezius, B. Bergues, M. F. Kling, A. Senftleben, C. D. Schröter, R. Moshammer, J. Ullrich, K. J. Betsch, R. R. Jones, A. M. Sayler, T. Rathje, K. Rühle, W. Müller, and G. G. Paulus. Single-shot carrier-envelope-phase-tagged ion-momentum imaging of nonsequential double ionization of argon in intense 4-fs laser fields. *Phys. Rev. A*, 83:013412, Jan 2011.

[99] A. Emmanouilidou. Prevalence of different double ionization pathways and traces of three-body interactions in strongly driven helium. *Phys. Rev. A*, 83:023403, Feb 2011.

[100] A. S. Maxwell and C. Figueira de Morisson Faria. Controlling below-threshold nonsequential double ionization via quantum interference. *Phys. Rev. Lett.*, 116:143001, Apr 2016.

[101] P. Kustaanheimo and E. Stiefel. Perturbation theory of Kepler motion based on spinor regularization. *J. Reine Angew. Math.*, 1965:204–219, 1965.

[102] C. Huang, Y. Zhou, Q. Zhang, and P. Lu. Contribution of recollision ionization to the cross-shaped structure in nonsequential double ionization. *Opt. Express*, 21(9):11382–11390, May 2013.

[103] A. Staudte, C. Ruiz, M. Schöffler, S. Schössler, D. Zeidler, Th. Weber, M. Meckel, D. M. Villeneuve, P. B. Corkum, A. Becker, and R. Dörner. Binary and recoil collisions in strong field double ionization of helium. *Phys. Rev. Lett.*, 99:263002, Dec 2007.

[104] A. Rudenko, V. L. B. de Jesus, Th. Ergler, K. Zrost, B. Feuerstein, C. D. Schröter, R. Moshammer, and J. Ullrich. Correlated two-electron momentum

spectra for strong-field nonsequential double ionization of He at 800 nm. *Phys. Rev. Lett.*, 99:263003, Dec 2007.

[105] B. HuP, J. Liu, and S. Chen. Plateau in above-threshold-ionization spectra and chaotic behavior in rescattering processes. *Phys. Lett. A*, 236(5):533 – 542, 1997.

[106] P. Wang, A. M. Sayler, K. D. Carnes, B. D. Esry, and I. Ben-Itzhak. Disentangling the volume effect through intensity-difference spectra: application to laser-induced dissociation of H_2^+. *Opt. Lett.*, 30(6):664–666, Mar 2005.

[107] J. G. Leopold and I. C. Percival. Ionisation of highly excited atoms by electric fields. III. microwave ionisation and excitation. *J. Phys. B: At. Mol. Opt. Phys.*, 12(5):709, 1979.

[108] B. Bergues, M. Kbel, N. G. Kling, C. Burger, and M. F. Kling. Single-cycle non-sequential double ionization. *IEEE J. Sel. Top. Quantum Electron.*, 21(5):1–9, Sep 2015.

[109] E. Lötstedt, T. Kato, and K. Yamanouchi. Classical dynamics of laser-driven D_3^+. *Phys. Rev. Lett.*, 106:203001, May 2011.

[110] E. Lötstedt, T. Kato, and K. Yamanouchi. A classical model of H_3^+ in an intense laser field. *J. Phys. B: At. Mol. Opt. Phys.*, 46(23):235601, 2013.

[111] A. Emmanouilidou and C. Lazarou. Multiple electron trapping in the fragmentation of strongly driven molecules. *New J. Phys.*, 14(11):115010, 2012.

[112] V. G. Anicich and J. H. Futrell. A computer study of the formation of H_3^+ and its vibrational deactivation using a statistical model. *International Journal of Mass Spectrometry and Ion Processes*, 55(2):189 – 215, 1984.

[113] D. Talbi and R. P. Saxon. Theoretical study of excited singlet states of H_3^+: Potential surfaces and transition moments. *J. Chem. Phys.*, 89(4):2235–2241, 1988.

[114] Th. Ergler, B. Feuerstein, A. Rudenko, K. Zrost, C. D. Schröter, R. Mosham-mer, and J. Ullrich. Quantum-phase resolved mapping of ground-state vibra-tional D_2 wave packets via selective depletion in intense laser pulses. *Phys. Rev. Lett.*, 97:103004, Sep 2006.

[115] E. Goll, G. Wunner, and A. Saenz. Formation of ground-state vibrational wave packets in intense ultrashort laser pulses. *Phys. Rev. Lett.*, 97:103003, Sep 2006.

[116] V. N. Serov, A. Keller, O. Atabek, and N. Billy. Quantitative theory-versus-experiment comparison for the intense laser dissociation of H_2^+. *Phys. Rev. A*, 68:053401, Nov 2003.

[117] F. Lindner, G. G. Paulus, H. Walther, A. Baltuška, E. Goulielmakis, M. Lez-ius, and F. Krausz. Gouy phase shift for few-cycle laser pulses. *Phys. Rev. Lett.*, 92:113001, Mar 2004.

[118] C. Altucci, V. Tosa, R. Velotta, and C. H. Nam. Dynamical medium depletion in high-order above-threshold ionization with few-cycle laser pulses. *Phys. Rev. A*, 70:065402, Dec 2004.

[119] P. H. Bucksbaum, A. Zavriyev, H. G. Muller, and D. W. Schumacher. Soft-ening of the H_2^+ molecular bond in intense laser fields. *Phys. Rev. Lett.*, 64:1883–1886, Apr 1990.

[120] T. Nubbemeyer, K. Gorling, A. Saenz, U. Eichmann, and W. Sandner. Strong-field tunneling without ionization. *Phys. Rev. Lett.*, 101:233001, Dec 2008.

[121] A. S. Alnaser, T. Osipov, E. P. Benis, A. Wech, B. Shan, C. L. Cocke, X. M. Tong, and C. D. Lin. Rescattering double ionization of d_2 and h_2 by intense laser pulses. *Phys. Rev. Lett.*, 91:163002, Oct 2003.

[122] M. Kitzler and M. Lezius. Spatial control of recollision wave packets with attosecond precision. *Phys. Rev. Lett.*, 95:253001, Dec 2005.

[123] M. Richter, M. Kunitski, M. Schöffler, T. Jahnke, L. P. H. Schmidt, and R. Dörner. Ionization in orthogonal two-color laser fields: Origin and phase dependences of trajectory-resolved Coulomb effects. *Phys. Rev. A*, 94:033416, Sep 2016.

[124] D. Ray, F. He, S. De, W. Cao, H. Mashiko, P. Ranitovic, K. P. Singh, I. Znakovskaya, U. Thumm, G. G. Paulus, M. F. Kling, I. V. Litvinyuk, and C. L. Cocke. Ion-energy dependence of asymmetric dissociation of D_2 by a two-color laser field. *Phys. Rev. Lett.*, 103:223201, Nov 2009.

[125] H. Li, D. Ray, S. De, I. Znakovskaya, W. Cao, G. Laurent, Z. Wang, M. F. Kling, A. T. Le, and C. L. Cocke. Orientation dependence of the ionization of co and no in an intense femtosecond two-color laser field. *Phys. Rev. A*, 84:043429, Oct 2011.

[126] X. Gong, P. He, Q. Song, Q. Ji, H. Pan, J. Ding, F. He, H. Zeng, and J. Wu. Two-dimensional directional proton emission in dissociative ionization of H_2. *Phys. Rev. Lett.*, 113:203001, Nov 2014.

[127] S. De, I. Znakovskaya, D. Ray, F. Anis, Nora G. Johnson, I. A. Bocharova, M. Magrakvelidze, B. D. Esry, C. L. Cocke, I. V. Litvinyuk, and M. F. Kling. Field-free orientation of CO molecules by femtosecond two-color laser fields. *Phys. Rev. Lett.*, 103:153002, Oct 2009.

[128] E. Frumker, C. T. Hebeisen, N. Kajumba, J. B. Bertrand, H. J. Wörner, M. Spanner, D. M. Villeneuve, A. Naumov, and P. B. Corkum. Oriented rotational wave-packet dynamics studies via high harmonic generation. *Phys. Rev. Lett.*, 109:113901, Sep 2012.

[129] I. Znakovskaya, M. Spanner, S. De, H. Li, D. Ray, P. Corkum, I. V. Litvinyuk, C. L. Cocke, and M. F. Kling. Transition between mechanisms of laser-induced field-free molecular orientation. *Phys. Rev. Lett.*, 112:113005, Mar 2014.

[130] I. J. Kim, C. M. Kim, H. T. Kim, G. H. Lee, Y. S. Lee, J. Y. Park, D. J. Cho, and C. H. Nam. Highly efficient high-harmonic generation in an orthogonally polarized two-color laser field. *Phys. Rev. Lett.*, 94:243901, Jun 2005.

[131] L. Brugnera, F. Frank, D. J. Hoffmann, R. Torres, T. Siegel, J. G. Underwood, E. Springate, C. Froud, E. I. C. Turcu, J. W. G. Tisch, and J. P. Marangos. Enhancement of high harmonics generated by field steering of electrons in a two-color orthogonally polarized laser field. *Opt. Lett.*, 35(23):3994–3996, Dec 2010.

[132] L. Brugnera, D. J. Hoffmann, T. Siegel, F. Frank, A. Zaïr, J. W. G. Tisch, and J. P. Marangos. Trajectory selection in high harmonic generation by controlling the phase between orthogonal two-color fields. *Phys. Rev. Lett.*, 107:153902, Oct 2011.

[133] N. Dudovich, O. Smirnova, J. Levesque, Y. Mairesse, M. Yu. Ivanov, D. M. Villeneuve, and P. B. Corkum. Measuring and controlling the birth of attosecond XUV pulses. *Nat. Phys.*, 2(11):781–786, Nov 2006.

[134] D. Shafir, Y. Mairesse, D. M. Villeneuve, P. B. Corkum, and N. Dudovich. Atomic wavefunctions probed through strong-field light-matter interaction. *Nat Phys*, 5(6):412–416, Jun 2009.

[135] X. Gong, C. Lin, F. He, Q. Song, K. Lin, Q. Ji, W. Zhang, J. Ma, P. Lu, Y. Liu, H. Zeng, W. Yang, and J. Wu. Energy-resolved ultrashort delays of photoelectron emission clocked by orthogonal two-color laser fields. *Phys. Rev. Lett.*, 118:143203, Apr 2017.

[136] R.Y. Rubinstein and D.P. Kroese. *Simulation and the Monte Carlo Method*. Wiley Series in Probability and Statistics. Wiley, 2016.

[137] Y. Zhou, Q. Liao, Q. Zhang, W. Hong, and P. Lu. Controlling nonsequential double ionization via two-color few-cycle pulses. *Opt. Express*, 18(2):632–638, Jan 2010.

[138] Y. Zhou, C. Huang, A. Tong, Q. Liao, and P. Lu. Correlated electron dynamics in nonsequential double ionization by orthogonal two-color laser pulses. *Opt. Express*, 19(3):2301–2308, Jan 2011.

[139] L. Chen, Y. Zhou, C. Huang, Q. Zhang, and P. Lu. Attosecond-resolved electron emission in nonsequential double ionization. *Phys. Rev. A*, 88:043425, Oct 2013.

[140] L. Zhang, X. Xie, S. Roither, Y. Zhou, P. Lu, D. Kartashov, M. Schöffler, D. Shafir, P. B. Corkum, A. Baltuška, A. Staudte, and M. Kitzler. Subcycle control of electron-electron correlation in double ionization. *Phys. Rev. Lett.*, 112:193002, May 2014.

[141] S. Eckart, M. Richter, M. Kunitski, A. Hartung, J. Rist, K. Henrichs, N. Schlott, H. Kang, T. Bauer, H. Sann, L. Ph. H. Schmidt, M. Schöffler, T. Jahnke, and R. Dörner. Nonsequential double ionization by counterrotating circularly polarized two-color laser fields. *Phys. Rev. Lett.*, 117:133202, Sep 2016.

[142] O. Svelto. *Principles of Lasers*. Springer US, 2010.

[143] R. P. Feynman. Space-time approach to non-relativistic quantum mechanics. *Rev. Mod. Phys.*, 20:367–387, Apr 1948.

[144] P. Salières, B. Carré, L. Le Déroff, F. Grasbon, G. G. Paulus, H. Walther, R. Kopold, W. Becker, D. B. Milošević, A. Sanpera, and M. Lewenstein. Feynman's path-integral approach for intense-laser-atom interactions. *Science*, 292(5518):902–905, 2001.

[145] M. Li, J.-W. Geng, H. Liu, Y. Deng, C. Wu, L.-Y. Peng, Q. Gong, and Y. Liu. Classical-quantum correspondence for above-threshold ionization. *Phys. Rev. Lett.*, 112:113002, Mar 2014.

[146] N. I. Shvetsov-Shilovski, M. Lein, L. B. Madsen, E. Räsänen, C. Lemell,

J. Burgdörfer, D. G. Arbó, and K. Tőkési. Semiclassical two-step model for strong-field ionization. *Phys. Rev. A*, 94:013415, Jul 2016.

[147] D. Tannor. *Introduction to Quantum Mechanics: A Time-Dependent Perspective*. University Science Books, 2007.

List of Publications

1. <u>A. Chen</u>, M. F. Kling, A. Emmanouilidou, Controlling electron-electron correlation in frustrated double ionization of molecules with orthogonally polarized two-color laser fields, accepted (Phys. Rev. A) (2017).

2. <u>A. Chen</u>, M. Kbel, B. Bergues, M. F. Kling, A. Emmanouilidou, Non-sequential double ionization with near-single cycle laser pulses, accepted (Sci. Rep.) (2017).

3. <u>A. Chen</u>, H. Price, A. Staudte, and A. Emmanouilidou, Frustrated double ionization in two-electron triatomic molecules, Phys. Rev. A 94, 043408 (2016).

4. <u>A. Chen</u>, C. Lazarou, H. Price and A. Emmanouilidou, Frustrated double and single ionization in a two-electron triatomic molecule H_3^+, J. Phys. B: At. Mol. Opt. Phys. 49, 235001 (2016).

5. A. Emmanouilidou, <u>A. Chen</u>, C. Hofmann, U. Keller. and A. S. Landsman, The effect of electron-electron correlation on the attoclock experiment, J. Phys. B: At. Mol. Opt. Phys. 48, 245602 (2015). (Journal of Physics B Highlights of 2015)